저작자표시-비영리-변경금지 2.0 대한민국

이용자는 아래의 조건을 따르는 경우에 한하여 자유롭게

- 이 저작물을 복제, 배포, 전송, 전시, 공연 및 방송할 수 있습니다.

다음과 같은 조건을 따라야 합니다:

저작자표시. 귀하는 원저작자를 표시하여야 합니다.

비영리. 귀하는 이 저작물을 영리 목적으로 이용할 수 없습니다.

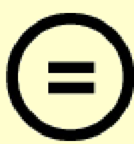

변경금지. 귀하는 이 저작물을 개작, 변형 또는 가공할 수 없습니다.

- 귀하는, 이 저작물의 재이용이나 배포의 경우, 이 저작물에 적용된 이용허락조건을 명확하게 나타내어야 합니다.
- 저작권자로부터 별도의 허가를 받으면 이러한 조건들은 적용되지 않습니다.

저작권법에 따른 이용자의 권리는 위의 내용에 의하여 영향을 받지 않습니다.

이것은 이용허락규약(Legal Code)을 이해하기 쉽게 요약한 것입니다.

Disclaimer

Doctoral Thesis

Non Local Spin Diffusion Driven by Spin Hall Effect at Oxide Heterointerfaces

Mi-Jin Jin

Department of Materials Science and Engineering

Graduate School of UNIST

2017

Non Local Spin Diffusion Driven by Spin Hall Effect at Oxide Heterointerfaces

Mi-Jin Jin

Department of Materials Science and Engineering

Graduate School of UNIST

Non Local Spin Diffusion Driven by Spin Hall Effect at Oxide Heterointerfaces

A thesis/dissertation
submitted to the Graduate School of UNIST
in partial fulfillment of the
requirements for the degree of
Doctor of Philosophy

Mi-Jin Jin

7. 18. 2017 Month/Day/Year of submission

Approved by

Advisor

Jung-Woo Yoo

Non Local Spin Diffusion Driven by Spin Hall Effect at Oxide Heterointerfaces

Mi-Jin Jin

This certifies that the thesis/dissertation of Mi-Jin Jin is approved.

July/18/2017 of submission

Advisor: Jung-Woo Yoo

Seung-Hyub Baek : Thesis Committee Member #1

Hyung-Joon Shin : Thesis Committee Member #2

Kibog Park : Thesis Committee Member #3

Ki-Suk Lee : Thesis Committee Member #4

UNIST
ULSAN NATIONAL INSTITUTE OF
SCIENCE AND TECHNOLOGY

Abstract

Thesis subject: Non-local spin diffusion driven by spin Hall effect at oxide heterointerface

This thesis describes spin Hall effect (SHE) / Inverse spin Hall effect (ISHE) induced non-local spin transport and detection through a LAO/STO 2-dimensional interface.

For that, first this thesis introduce about basic knowledge of spintronics with regard to spin transport, injection and detection. Also spin orbit coupling (SOC) and related effect with Rashba SOC which is closely related to the experimental results will be described intensively. The physical origin of SHE/ISHE is discussed based on intrinsic and extrinsic mechanism followed by the previous experimental works done in various systems. Then, 2-dimentional electron gas of $LaAlO_3/SrTiO_3$ (LAO/STO) interface and its interesting phenomenon are introduced along with recent research progress, which shows that the LAO/STO is exciting playground for spin-orbitronics.

For the main part of this thesis, our experimental scheme of the non-local measurement for the spin diffusion and precession through the SHE/ISHE is first described. Next, detailed sample preparation, patterning and fabrication method are explained. The fabricated H-bar type geometry device can manipulate spin current without spin injection from ferromagnetic material and detect through same material (LAO/STO 2DEG H-bar geometry). Generating a spin current not through the spin injection from outside but instead through the inherent spin Hall effect and demonstrating the non-local spin transport is a novel approach for spintronic application with 2DEG materials. The analysis on the non-local spin voltage, confirmed by the signature of a Larmor spin precession and its length dependence, displays that both D'yakonov-Perel' and Elliott-Yafet mechanisms involve in the spin relaxation at low temperature. Our results show that the oxide heterointerface is highly efficient in spin-charge conversion with exceptionally strong spin Hall coefficient $\gamma \sim 0.15 \pm 0.05$ and could be outstanding platform for the study of coupled charge and spin transport phenomena and their electronic applications.

Contents

Abstract -- 1

List of figures -- 5
List of tables -- 15
List of Abbreviations -- 16

Chapter 1. Introduction of Electrical Spin Transport -- 18
1.1 Spintronics (from develop to now) --- 18
1.2 Spin transport (Spin current) -- 20
1.3 Spin injection & detection --- 21
1.4 Spin relaxation mechanism -- 30

Chapter 2. Spin Orbit Coupling (SOC) & Spin Hall Effect (SHE) -- 33
2.1. Spin orbit coupling (SOC) – intrinsic & extrinsic -- 33
2.2. SOC at 2D – Rashba SOC -- 41
2.3. Spin Hall effect vs Inverse Spin Hall effect --- 49
2.4. Detection of SHE without ferromagnetic materials -- 56

Chapter. 3. LAO/STO 2-Dimensional Electron Gas (2DEG) --- 61
3.1. Introduction of LAO, STO, and 2DEG --- 61
3.2. LAO/STO research trend -- 65
3.3. Spin transport in LAO/STO -- 71
3.4. Localization (Related issue for spin transport in LAO/STO 2DEG) ---------------------- 74

Chapter. 4. Experimental Technique (Sample Fabrication) -- 77
4.1. LAO/STO sample preparation -- 77
4.2. Patterning process & Fabrication -- 79
4.3. Test equipment -- 87

Chapter. 5. Non-Local Spin Signal in LAO/STO -- 89
5.1. Introduction (Idea & motivation) -- 89
5.2. Fabricated device basic property (basic property) -- 91

5.3. Rashba SOC in LAO/STO (planer AMR) -- 96
5.4. Non-local spin signal depends on the channel length -- 99
5.5. Non-local spin signal with temperature & Relaxation mechanism ------------------------ 102
5.6. Summary -- 105

References -- 106
Appendix A : List of Achievements -- 114
Acknowledgements --- 117

List of Figures

Figure 1-1. Introduction of spintronics example via spin engineering

Figure 1-2. A schematic diagram of the electron spin movement and the two channel resistance model at parallel and antiparallel states.

Figure 1-3. Schematic example of GMR behavior (at multi layers of thin film) with perpendicular magnetic field. The GMR is present for ferromagnetic layers which are separated by a non-magnetic or an antiferromagnetic metallic thin film. (H_s: saturation magnetic field for parallel state of magnetization)

Figure 1-4. Schematic of ideal magnetoresistance curve of two FM layer with spacer material as a function of in-plane external magnetic field sweep. The two FM layers have different coercive field with different field dependent magnetization behavior (upper graph). And because of the different coercive field, field dependent resistance shows two times of different resistance change during the field sweep (below R vs H graph).

Figure 1-5. Two types of GMR devices. Current in plane (CIP) and Current perpendicular to plane (CPP)

Figure 1-6. Non-local spin injection and detection at spin valve device. (a) Top view. (b) Side view. Current I is sent from F1 to the left end of N. The spin accumulation at $x = L$ is proves by measuring voltage V at F2. (c) Spatial variation of the ECP for up-and down-spin electrons in N. (d) Densities of states for the up- and down-spin bands in N (center) and F2 (left and right). (e) Non-local resistance V/I as a function of in-plane magnetic field B, where P and AP represent the parallel and antiparallel orientations of magnetizations in F1 and F2 (reproduced from reference 7).

Figure 1-7. Schematic illustration of the Hanle effect at ferromagnet/tunnel barrier/conducting channel junction device. This allows manipulation of the spin polarization by applying magnetic field perpendicular to the spins. The spin accumulation (near the zero magnetic field) gradually reduces to zero with increasing magnetic field. (at $B = 0$, static spin polarization and maximum spin accumulation, at $B \neq 0$, spin precession, and suppressed spin accumulation).

Figure 1-8. An example of the experimental detection about representative non-local lateral spin valve and Hanle effects. (a) A schematic diagram of the non-local experiment (not to scale). The large arrows

indicate the magnetizations of the source and detector. The two different contact separations are 160 μm and 12 μm. Electrons are injected along the path shown in red. The injected spins (purple) diffuse in either direction from contact 3. The non-local voltage is detected at contact 4. Other choices of source and detector among contacts 2, 3 and 4 are also possible. (b) Non-local voltage, $V_{4,5}$, versus in-plane magnetic field, B_y, (swept in both directions) for sample A at a current I = 1.0 mA and T = 50 K. The raw data are shown in the upper panel (with an offset V_0 = -30.227 mV subtracted). The background (dashed cyan curve underneath the data) is fitted by a second-order polynomial. The lower panel shows the data with this background subtracted. (c) Non-local voltage, $\mathbf{V_{4,5}}$, versus perpendicular magnetic field, B_z, for the same contacts and bias conditions (and the same offset V_0) as in b. The data in the lower panel have the background (dashed cyan curve in the upper panel) subtracted. The data shown in black are obtained with the magnetizations of contacts 3 and 4 parallel, and the data shown in red are obtained in the antiparallel configuration (reproduced from reference 12)

Figure 1-9. Relevant spin relaxation mechanisms for conduction electrons. (a) The Elliott–Yafet mechanism. The periodic spin-orbit interaction makes the spin ‘‘up’’ Bloch states contain small spin-down amplitude, and vice versa. Impurities, boundaries, and phonons can induce transitions between spin ‘‘up’’ and ‘‘down’’ leading to depolarization of spin. (b) The D’yakonov–Perel’ mechanism. In non-centrosymmetric crystals spin bands are no longer degenerate: in the same momentum state spin up has different energy than spin down. This is equivalent to having internal magnetic fields depending on, electron’s momentum. The spin of an electron precesses along such a field, until the electron momentum changes by impurity, boundary, or phonon scattering. Then the precession starts again, but along a different axis. Since the spin polarization changes during the precession, the scattering acts against the spin relaxation. (c) The Bir–Aronov–Pikus mechanism. The exchange interaction between electrons and holes causes the electron spins to precess along some effective magnetic field determined by hole spins. In the limit of strong hole spin relaxation, this effective field randomly changes before the full precession is completed, reducing the electron spin relaxation (reproduced from reference 15).

Figure 2-1. Various applications of Spin-orbitronics. If there is a spin-orbital coupling phenomenon due to broken inversion symmetry in some systems, a unique characteristic that can realize spin-orbitronics appears. In other words, spin-orbitronics is an electronic device field realized by controlling the spin-orbit coupling phenomenon. As shown in this figure, the magnetization direction and the spin direction of the material or device can be electrically controlled (using spin-orbit coupling phenomenon) and a desired state is realized as a device (reproduced from reference 16)

Figure 2-2. Comparison of the band structure (dispersion relation) of the free electron, Zeeman spin

splitting and Rashba spin splitting.

Figure 2-3. Comparison of the three kind of spin splitting, Rashba spin splitting, Zeeman spin splitting and valley spin splitting.

Figure 2-4. Spin texture at the fermi surface. (a) Rashba (2-dimensional SOC at the interface or surface), (b) Dresselhause (3-dimensional SOC at the bulk materials), (c) Rashba plus Dresselhaus.

Figure 2-5. Comparison of intrinsic SOC and extrinsic SOC. In this figure, the intrinsic SOC from structural inversion symmetry and extrinsic SOC were introduced which is closely related with this thesis experiment.

Figure 2-6. Schematic of Mott-skew scattering mechanism of extrinsic SOC. Spin up and down electrons changes its scattering angle by the impurity.

Figure 2-7. Schematic of Side-jump machanism of extrinics SOC. Spin up and down electrons undergoes lateral displacement during scattering event by the impurity.

Figure 2-8. Summary of SOC and its phenomenon (spin Hall and inverse spin Hall effect) mechanism

Figure 2-9.Comparison of conventional FET and spin-FET. Conventional FET just flows the electron (or hole) charge depends on the gate voltage, Spin-FET flows electron spin with controlling the electron spin direction by the gate voltage.

Figure 2-10. Experimental detection of Spin-FET. By applying top gate voltage and external field, the voltage modulation is detected (reproduced from reference 29).

Figure 2-11. Schematic band structure of Rashba and Rashba-Edelstein effect. When current is applied into the Rashba interface, there are deficit of spin down and excess of spin up state (Δk) will appear and the spin accumulation can be exist.

Figure 2-12. Experimental detection of Inverse Rashba-Edelstein Effect (IREE). The efficient conversion from spin-to charge current found at the Ag/Bi interface shows that the REE could be a major tool for the generation and detection of spin currents or magnetization control (reproduced from reference 31).

Figure 2-13. The Spin Galvanic effect (SGE). SGE arises from asymmetric electron relaxation in a spin-split conduction band. Initially, spin polarized state (left) relaxes towards equilibrium (right) by means of four types of spin flip transition (center). The solid blue arrows indicate balanced transitions that together preserve the symmetrical distribution. But transitions shown by dashed red arrows do not balance causing a spin-polarized current.

Figure 2-14. Complementary spin Hall and inverse spin Galvanic effect torques (up) and the detection of robust spin orbit torque/spin Galvanic effect (down) (reproduced from reference 37, 38).

Figure 2-15. (left) Hall Effect (right) spin Hall effect. In the Hall effect, magnetic field B and the associated Lorentz force *F* generate transverse charge accumulation with opposite direction for electron and hole. And the electrochemical potential of spin up and down carriers are the same. A voltage difference between the two edges is built up. In the spin Hall effect, spin accumulation with opposite direction for up and down spin can be generated by the spin orbit coupling without magnetic field. And the electrochemical potential for spin up and down carrier is different. There are no measured voltage difference between two edges will show but spin orientation dependent voltage exist.

Figure 2-16. Schematic of spin Hall effect (SHE) and inverse spin Hall effect (ISHE) which are represents conversion charge current transverse spin current (SHE) and from spin current to transverse charge current (ISHE). Spin Hall constant γ (= spin Hall angle) can be define as spin Hall conductivity σ_{SH} divide by charge conductivity σ_{C}.

Figure 2-17. Hall effect family. After Hall effect was discovered at 1879, various Hall effect related or similar phenomenon were introduced and proved by experiment.

Figure 2-18. First experimental observation of direct spin Hall effect (SHE). They used GaAs semiconductor sample and optically detected spin polarization by Kerr rotation microscopy (reproduced from reference 42).

Figure 2-19. The SHE measurement using LED. (a) Scanning electron microscopy image of the SHE LED device. (b) Polarization along z axis measured with active LED 1 for two opposite I_p current orientations. Spectral region of peak B of the high bias electroluminescence (EL) curve of wafer 1 is shown. Non-zero and opposite out-of-plane polarization for the two I_p orientations demonstrates the SHE. (c) Polarization along z axis measured with fixed I_p current and for biased LED 1 or LED 2. The data show opposite polarizations at opposite edges of the 2-dimensional hole gas (2DHG) channel

confirming the SHE origin of the measured signal (reproduced from reference 43).

Figure 2-20. Experimental detection method of SHE/ISHE

Figure 2-21. Example of SHE/ISHE detection measurement. They measured not only spin Hall induced R vs perpendicular magnetic field curve (right side), but also spin precession signal (Hanle curve) by using non-local spin valve device geometry (center) (reproduced from reference 52).

Figure 2-22. Example of SHE/ISHE detection measurement. Using FM material, spin-polarized current was injected into the high SOC metal (Au), then the inverse spin Hall voltage signal was obtained displaying hysteresis behavior (reproduced from reference 53).

Figure 2-23. SEM image of H-bar geometry spin Hall device (up) and schematic current flow of (a) diffusive (b) spin Hall and (c) quasi-ballistic region (reproduced by reference 55).

Figure 2-24. Spin Hall effect transistor. (a) Schematics of the measurement setup with optically injected spin-polarized electrical current propagating through the Hall bar and corresponding experimental Hall effect signals at crosses H1 and H2. (b) Same as (a) for measurement geometry in which electrical current is closed before the first detecting Hall cross H1. (c) Schematics of the diffusive transport of injected spin-polarized electrons and Monte-Carlo simulations of the out-of-plane component of the spin of injected electrons averaged over the 1-mm bar cross section assuming Rashba field α = 5.5 meV Å, Dresselhaus field β = −24 meV Å, and different values of the mean free path l (reproduced from reference 57).

Figure 2-25. Spin Hall effect using non-local geometry in graphene. They obtain SOC induced non-local voltage difference and further spin precession signal via parallel magnetic field by using 2D graphene channel material (reproduced from reference 58).

Figure 2-26. Possible thermal effect during non-local SHE measurement. With/without perpendicular magnetic field, the possible thermal effect such as Seebeck, Peltier, Nernst and Ettingshaugen effect can be present.

Figure 3-1. Polar catastrophe and charge reconstruction mechanism of LAO/STO interface conductivity.

Figure 3-2. Electronic structure of LAO/STO interface. Left, The dispersion of the different sub-bands.

The lowest energy sub-bands have a d_{xy} character. Right, Extension of the wave functions of the sub-bands through $SrTiO_3$. The lowest energy d_{xy} electrons are very spatially localized at the interface, whereas d_{xz} and d_{yz} extend further into the $SrTiO_3$ (reproduced from reference 78).

Figure 3-3. Emergent phenomena and 2D electron gas with Rashba SOC at oxide interface (reproduced from reference 114).

Figure 3-4. Interesting phenomena of LAO/STO interface.

Figure 3-5. Controllable conductivity of LAO/STO interface via several kinds of method.

Figure 3-6. Transistor operation in top gated LAO/STO heterostructures (reproduced from reference 104)

Figure 3-7. Giant photovoltaic effects driven by residual polar field (reproduced from reference 105)

Figure 3-8. Highly sensitive gas sensor by the modulation with Pd nanoparticles (reproduced from reference 106)

Figure 3-9. First experimental spin injection and detection at LAO/STO interface (left) and suggested spin injection mechanism from FM materials to 2DEG through LAO oxide insulator (right) (reproduced from reference 81).

Figure 3-10. Gate tunable spin precession signal with RA product change (reproduced from reference 81).

Figure 3-11. Spin to charge conversion in NiFe/LAO/STO device. (a) Schematic of spin-pumping experimental configuration. (b) Ferromagnetic resonance signal at negative and positive external magnetic fields, at a gate voltage of V_g = +125V. (c) Detected voltage normalized to the square of the amplitude of the RF field (thick solid lines) at negative and positive external magnetic fields at V_g = +125V. (d) Sketch of a electron dispersion in Rashba-type system at equilibrium. At the Fermi level there are two Fermi contours (one sketched in blue, the other in red) with opposite spin textures (the blue and red arrows show the spin direction of the electrons on the outer and inner contour, respectively). (e) Principle of the inverse Edelstein effect: the injection of a current j_s of spins oriented along y from the ferromagnet creates an accumulation of spin-up electrons (darker blue and red arrows) and a

depletion of spin-down electrons (lighter blue and red arrows). This accumulation/depletion process shifts the two inequivalent Fermi contours, which generates a transverse charge current along x (reproduced from reference 110).

Figure 3-12. Weak/weak anti-localization depends on the relative length between electric mean free path (l), spin orbit length (L_{so}) and phase coherence length (L_{φ}).

Figure 3-13. Experimental observation of weak/weak anti-localization and Rashba SOC at LAO/STO interface. Depends on back gate voltage, weak/weak anti-localization is changed. Rashba SOC constant was obtained by fitting the MR curve (reproduced from reference 83).

Figure 3-14. Electronic phase diagram which represent gate dependent WL/WAL and Rashba field at LAO/STO interface (reproduced from reference 114, 115)

Figure 4-1. AFM images of the surface morphology (a) TiO_2-terminated STO substrate. (b) LAO/STO substrate.

Figure 4-2. The prepared LAO/STO has metallic behavior of temperature dependent sheet resistance and mobility measured with Van Der Paww geometry. The estimated mobility and carrier concentration averaged for several samples were 1200 cm^2/Vs and 3.1 x 10^{13} cm^{-2}, respectively.

Figure 4-3. Schematic of bottom-up device fabrication steps for H-bar patterned LAO/STO 2DEG.

Figure 4-4. Example of resistance vs temperature for contact electrode with good adhesion condition (left) and contact electrode with poor adhesion condition (right).

Figure 4-5. Device fabrication procedure. (a) Device fabrication steps. (b) Schematics of the side views of the device at each fabrication step. (c) Optical images of the top views at each fabrication step.

Figure 4-6. AO/STO sample before (a) and after (b) patterning. R1 and R2 indicate resistances taken with current and voltage contact configuration rotated by 90° (see inset of (b) and (d)). Inset is an optical microscopy image of the etched van der Pauw pattern. The black arrow and white dashed lines in (a) and (b) are a guide to the eye to show the position of the cubic-tetragonal transition and the slope change in R (T). The process of etching the sample is shown in (c). A photoresist mask is patterned on bare LAO/STO, which is subsequently etched. The mask is removed, leaving only the conductive interface

covered by the pattern. After the process is complete, the sample topography was imaged using an optical profilometer (d) (reproduced from reference 116).

Figure 4-7. (Top) E-beam lithography system. Specifications: 2.1 nm beam size for 100 keV with 7 nA beam current, ≤ 5 nm of line width, Address grid resolution around 1 nm (1 mm main field), and beam voltage range of 30 ~ 100 keV. (Bottom) Thermal/e-beam evaporation system.

Figure 4-8. Thermal annealing system of Atomic Layer Deposition (ALD) chamber. Specific heating range is up to 500 ˚C with up to 100 sccm flow gas of oxygen, argon, nitrogen, and so on.

Figure 4-9. Reactive ion etching (RIE) condition set-up for top-down process. Atomic force microscope (AFM) image of etched LAO/STO and etched STO surface (up) and its RIE test condition (down). When pattering the H-bar type geometry of LAO/STO 2DEG, the estimated etching rate of LAO/STO was ~ 5 nm/min with plasma power 1500 W and deep power 200 W.

Figure 4-10. Sample image connected to PPMS puck before the electrical measurement.

Figure 4-11. Physical properties measurement system (PPMS) and connected electrical measurement system. PPMS has specification of temperature range 1.8 K - 400 K with temperature accuracy of ± 0.5 % , continuous low-temperature control, controlled temperature sweep mode, and magnet range ± 9 T with field resolution of 0.3 Oe to 1 T and 3 Oe to 9 T.

Figure 5-1. Experimental plane with H-bar type sample geometry. i) SHE & ISHE induced non-local spin signal though the oxide interface. ii) Non-local spin precession signal by external magnetic field (Hanle curve) and obtain Rashba SOC constant & spin diffusion length & spin life time at LAO/STO 2DEG. iii) channel length dependence and temperature dependence of the spin signal and analysis the mechanism of SOC.

Figure 5-2. Local IV curve (left) and temperature dependent resistance behavior of device (right). Local IV curve should be linear relation to remove thermal effect or unstable detecting voltage. And Resistance vs Temperature curve clearly shown the metallic behavior.

Figure 5-3. Local transport properties measured for the device A. (a) Temperature dependence of Hall mobility. (b) Temperature dependence of sheet carrier density.

Figure 5-4. Non-local MR measured as a function of perpendicular magnetic field for the device A. Measurements taken with I_{DC} = 10 μA for the 3 μm channel of device A. The non-local voltage showed only a trace of a Hall voltage offset, which is directly proportional to the applied perpendicular magnetic field.

Figure 5-5. Local MRs measured as a function of parallel magnetic field for the device A. Measurements taken with I_{DC} = 10 μA for each of the two-terminal probes as shown in the inset of figure 5-2.
Figure 5-6. (a) MR as a function of perpendicular magnetic field measured for the local line (probe 1-2) at various temperatures (T = 2, 5, 10, 20, and 50 K). The MR curves are shifted vertically for clarity. (b) AMR measured for the local line (probe 1-2) with a source current of I_{DC} = 30 μA at B_a = 8 T and T = 2, 5, 10, 20, and 50 K. The inset shows the measurement configuration with respect to the applied magnetic field (B_a) in the plane. The angle dependent AMR displays an asymmetry between θ = 0 and 180, which implies the presence of equivalent field arisen from the Rashba spin-orbit interaction (denoted as B_R in the inset).

Figure 5-7. Temperature dependent behavior of magnetoresistances (MRs) measured for the device A. (a) MRs as a function of perpendicular magnetic field measured at T = 20, 30, 40, 50, 70, and 100 K. (b) MR curves plotted according to the generalized Kohler's rule $\Delta\rho/\rho_0 \sim f(\mu H)$. All curves excellently collapse in a single function displaying universal behavior.

Figure 5-8. Comparison of conventional planer AMR and planer AMR with Rashba SOC at a conductive interface. As already mentioned above chapters, asymmetry AMR also can be the evidence of Rashba SOC (reproduced from reference 96, 144).

Figure 5-9. Angle-dependent AMR measured for the device A. (a) AMR measured at B = 8 T for I_{DC} = 5, 10, 20, and 30 μA. (b) AMR measured at H = - 8 T for I_{DC} = 5, 10, 20, and 30 μA.

Figure 5-10. The estimated Rashba-like fields. (a) Rashba-like fields for various DC currents. Values were estimated by fitting equation (6) to the results in figure 5-4. (b) Rashba-like fields for various temperatures. Values were estimated by fitting equation (6) to the results in figure 5-6 (b).

Figure 5-11. Device geometry for the study of spin Hall induced spin diffusion in LAO/STO. (a) SEM image of the non-local device (device A) fabricated on a 5 mm x 5 mm STO substrate. The line width is 500 nm. Channel lengths, i.e., the distances between the centers of consecutive lines, are 2, 3, 4, and 5 μm. The inset shows a cross-sectional high-resolution transmission electron microscope (HR-TEM)

image of the LAO/STO interface. (b) Schematic of spin Hall induced non-local spin diffusion and its measurement configuration. In this geometry, local charge current induces a transverse spin current via the spin Hall effect, which in turn produces non-local spin voltage via the inverse spin Hall effect.

Figure 5-12. Dependence of non-local spin signals on channel length. (a) Non-local voltage as a function of in-plane magnetic field measured for the channels with lengths of 2 and 3 μm. The inset displays a measurement configuration with the relative orientation of the in-plane magnetic field. Red and blue lines are fits of equation 2 to the data. The 3 μm channel produced a narrower Hanle curve due to increased transit time for spin. (b) The magnitude of the non-local spin voltage as a function of the channel length measured for the device A and B. Solid lines are fits of equation 1 to the data.

Figure 5-13. Temperature dependence of non-local spin signals measured for the device B. (a) Non-local spin resistance as a function of in-plane magnetic field for the channel of 3 μm measured at 2, 5, 10, 15, 17 K. The non-local spin signals are shifted vertically for clarity. (b) Temperature dependence of the extracted parameters by fitting with eq 2 to the measured Hanle curves. From top to bottom, the magnitude of non-local spin resistance, spin diffusion length, spin Hall angle, and spin relaxation time are displayed. (c) The plot of $\tau_{\mathrm{p}} / \tau_{\mathrm{s}}$ versus τ_{p}^{2}, obtained from temperature dependent τ_{s} and τ_{p} values. The red line is a linear fit. The slope and *y* intercept of a linear fit yielded Δ_{DP} ~ 30 μeV and $\Delta g \sim 0.068$. (d) The estimated EY spin relaxation time $\tau_{\mathrm{s,EY}}$ and DP spin relaxation time $\tau_{\mathrm{s,DP}}$ as a function of temperature.

Figure 5-14. Major two types of spin relaxation mechanism of Elliott-Yafet & Dyakonov-Perel' mechanism.

List of Tables

Table 3-1. Property of each LAO and STO single crystal.

Table 3-2. Comparison between LAO/STO and other solid-state materials systems for nanoscale devices. Although LAO/STO is currently more electronically disordered than the other materials systems, its broad array of physical properties and potential tunability make it very attractive as a system for studying correlated electron physics in engineered environments (reproduced from reference 108).

List of Abbreviations

2D	2-dimensional
2DEG	2-dimensional electron gas
2DHG	2-dimensional hole gas
AFM	Atomic force microscopy/Atomic force microscope
ALD	Atomic layer deposition
AMR	Anisotropic Magnetoresistance
BAP	Bir-Aronov-Pikus
CIP	current in plane
CPGE	Circular photo Galvanic effect
CPP	current perpendicular to plane
DOS	Density of state
DP	D'yakonov-Perel'
ECP	Electrochemical potential
EL	Electroluminescence
ELS	Electronic localized states
EY	Elliott-Yafet
FET	Field effect transistor
FM	Ferromagnetic or Ferromagnet
GMR	Giant magnetoresistance
H-bar	Hall bar
HF	Hydrofluoric acid
HR-TEM	High resolution-Transmission electron microscope
ISHE	Inverse spin Hall effect
IREE	Inverse Rashba-Edelstein effect
ISGE	Inverse spin Galvanic effect
LAO	$LaAlO_3$
LED	Light emitting diode
MR	Magnetoresistance
MRAM	Magnetic random access memory
MTJ	Magnetic tunnel junction
NM	Non-magnetic
PPMS	Physical property measurement system

QW	Quantum well
RA	Resistance area
RAM	Random access memory
Rashba SOC	Rashba spin orbit coupling
REE	Rashba-Edelstein effect
RIE	Reactive ion etching
SdH	Shubnikov-de Haas
SDT	Spin dependent tunneling
SGE	Spin Galvanic effect
SHE	spin Hall effect
SL	Strong localization
SOC	Spin Orbit Coupling
STO	$SrTiO_3$
STT-RAM	Spin transfer torque – Random access memory
TMDs	Transition metal dichalcogenides
TMR	Tunnel Magnetoresistance
TSP	Tunneling spin polarization
VDP	Van Der Paww
WAL	Weak anti-localization
WL	Weak localization

Chapter 1.

Introduction of Electrical Spin Transport

1.1 Spintronics: from develop to now

Electrons have both particle and wave properties, and carry negative charges with various condensed matter characteristics. The electron also has its own angular momentum, which is spin. Spins are a major source of the material's magnetic properties, and when the spins are aligned in a solid, the solid becomes a material with having magnetic properties. The electron spin angular momentum and orbital angular momentum has been proposed by a fundamental study of atomic linear spectroscopy (1925 Uhlenbeck and Goudsmit[1, 2]) since the discovery of electrons by JJ Thompson in 1897 and the beginning of quantum mechanics in the 20th century. Unlike current electronics which uses the electron and its movement characteristics, spintronics uses the intrinsic angular momentum of electrons further.

Namely, the field of spintronics aims to manipulate not only electron charge but also electron spin for the electronic device application. Conventional electronic devices ignore the spin property and rely rigidly on the transport of the electron charge. If we add the spin property, it provides new capabilities and functionalities.

The start of spin based electronics (spintronics) was due to the foundation of magnetoresistance by William Thomson at 1857 [3]. Afterward, at 1988, the development of GMR (Giant magnetoresistance) by Albert Fert and Perter Grunberg[4, 5] can make it possible to improve the application of industrial production. From the beginning of GMR foundation, we have experienced dramatic development in spin related fundamental physics and engineering for the past century. Based on the study of spin related (quantum) physical phenomena such as GMR, TMR (Tunneling magnetoresistance), spin precession, spin torque, spin orbit coupling (spin Hall effect), topological insulator, and spin Seebeck effect (spin caloritronics), various extended industrial device was suggested and developed as shown in figure 1-1 (Ex. Magnetic hard disk, Magnetic Random Access Memory (MRAM), spin-FET, Spin-LED, STT-RAM etc.). Also, the materials used in spintronic researches have been widely expanded from simple mono-element of magnetic materials to multi-element alloy of magnetic materials, magnetic ceramics (magnetic oxide), organic or inorganic hybrid magnetic materials, 1 or 2-dimensional materials, and 2-dimensional conductive interface materials.

Especially, it is now already a public reality that the evolving electronic industry and the electronic

device market can be limited by merely using the behavior of electrons due to the ultra-high integration and high efficiency of the device size. In this situation, there is a growing need for research using not only simple behavior of electrons but also behavior of their spin angular momentum. The spintronic research has now being extended to various electronic devices as well as simple magnetic related devices. These devices have the possibility of enhanced functionality, higher speed, and reduced power consumption.

2-dimensional (2D) material and/or the 2-dimensional electron gas (2DEG) at the oxide interface have been considered as a fascinating materials for the application of next-generation devices or spintronic devices. Their structural property, which lead to a considerable spin orbit interaction and related effects, such as spin orbit torque received great attention for the spin-orbitronic applications (figure 2-1).

Figure 1-1. Introduction of spintronics example via spin engineering

1.2 Spin Transport (Spin current)

In theoretical point of view, the detailed understanding (analysis) of spin transport or spin current is not simple, and there are still some areas that have not been clearly solved. In this chapter, we will focus only on the fundamental spin current and basic concepts related to spin injection and detection to understand the control of spin charge (in conductive 2D materials), which is the main experiment of the paper.

The spintronic mainly based on the non-equilibrium spin population. Electron spin has its own magnetic moment of spin angular momentum and the quantized value of +1/2, -1/2. When the flow of electron charge (-e) expressed as I_{charge} = (-e) × (# of electrons/sec), then the flow of electron spin ($\hbar/2$) can be expressed as I_{spin} = ($\hbar/2$) × (# of electrons/sec) where the $\hbar$ is plank constant ($\hbar = h/2\pi = 1.0546 \times 10^{-34}$ Js). A diffusion spin current due to a spatial inhomogeneous spin density and a drift spin current in the absence of coherent dynamics of spin can be expressed using two channel resistance model. We can define a total charge current as a sum of spin up and spin down charge currents. And the spin currents can be expressed a difference of spin up and spin down charge currents as shown below,

$$I_{total} = I_{\uparrow} + I_{\downarrow}$$

$$I_{spin} = I_{\uparrow} - I_{\downarrow}$$

$$= (\frac{\hbar/2}{-e})I_{\uparrow} - (\frac{-\hbar/2}{-e})I_{\downarrow} = \frac{\hbar/2}{-e}(I_{\uparrow} - I_{\downarrow})$$

And spin polarization (P) can be given by spin current/total charge current,

$$P = \frac{I_{\uparrow} - I_{\downarrow}}{I_{\uparrow} + I_{\downarrow}}$$

The spin polarization deduced from different experiments depends on what precisely is being measured:

$$P_n = \frac{v_{F\uparrow}^n N_{\uparrow} - v_{F\downarrow}^n N_{\downarrow}}{v_{F\uparrow}^n N_{\uparrow} + v_{F\downarrow}^n N_{\downarrow}}$$

where V_F is fermi velocity $v_F = \frac{\hbar k_F}{m_e}$ and n = 0 for electron ejected in a spin-polarized photoemission experiment, n = 1, n = 2 for the ballistic transport and for the diffusive transport experiment.

Referentially, during the electron spin transport, the scattering event will appear due to the presence of disorder, impurities or phonons and spin will interact with other particles (electron, nuclear, and so on). There are four major types of interaction mechanism is exist (this was reproduced from the book of “Spin physics in semiconductor” by M. I. Dyakonov)

1. Direct magnetic interaction – the dipole-dipole interaction between the magnetic moments of a

pair of electrons. Normally negligible for electrons, however important for nuclear spins.

2. Exchange interaction – Coulomb interaction between electrons, which becomes spin dependent because their wave function must be anti-symmetric. This is at the origin of ferromagnetism and important in magnetic semiconductors. This interaction can be distinguished with direct, super, indirect, double and anisotropic exchange interaction.
3. Spin-orbit interaction – If an observer moves with a velocity v in an external electric field E, he will see a magnetic field $B = (v/c)\times E$. Thus there is an effective magnetic field acting on the magnetic moment (spin) of a moving electron. Strongly enhanced for atoms with large Z. This interaction is responsible for most of the spin-related optical and transport effects.
4. Hyperfine interaction with lattice nuclei – Magnetic interaction between the electron and nuclear magnetic moments. Important for bands originating from s-states in atoms with large Z. Leads to spectacular phenomena in the strongly coupled electron–nuclei spin system

For the electron spin transport, the exchange interaction and spin orbit interaction will be the major interaction mechanism at the solid state.

1.3 Spin injection & detection

A successful spintronic device require three effective steps; spin injection or generation, spin manipulation, and spin detection. For that, widely used (basic) behavior of magnetoresistance is GMR (giant magnetoresistance), TMR (Tunneling magnetoresistance), and AMR (Anisotropic magnetoresistance). The GMR phenomenon is a resistance difference when the magnetization directions of the two magnetic layers are parallel (R_P) or antiparallel (R_{AP}) to each other due to spin dependent scattering when the current passes through at least two magnetic layers. This GMR ratio is expressed by the following equation;

$$GMR(\%) = \frac{R_{\mathrm{AP}} - R_{\mathrm{P}}}{R_P} \times 100$$

A schematic of GMR thin film structure's parallel and anti-parallel state and its two channel resistance model are shown in figure 1-2, and its external magnetic field (perpendicular) dependent resistance graph is shown in figure 1-3. The GMR device has anti-parallel state at near the zero external magnetic field (out of plane) and become parallel state over the saturation field.

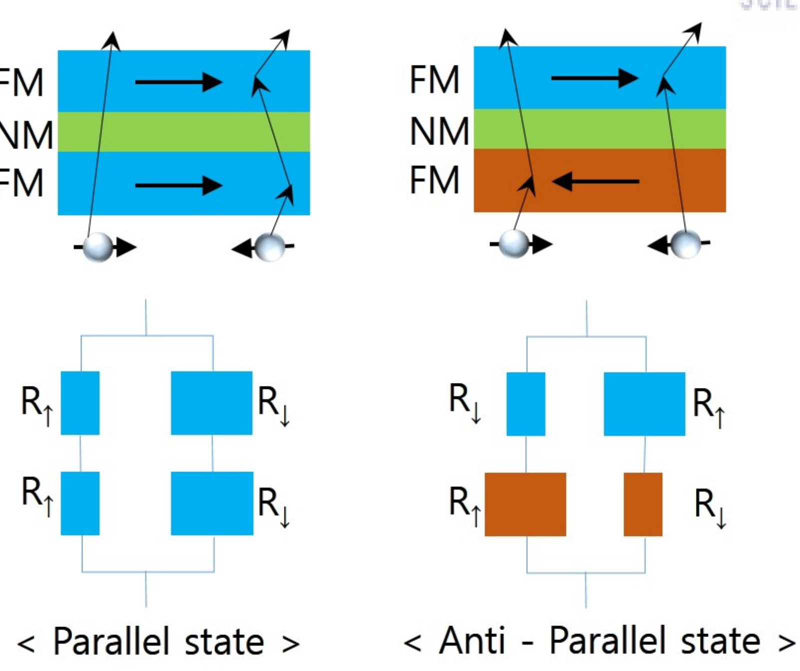

Figure 1-2. A schematic diagram of the electron spin movement and the two channel resistance model at parallel and antiparallel states.

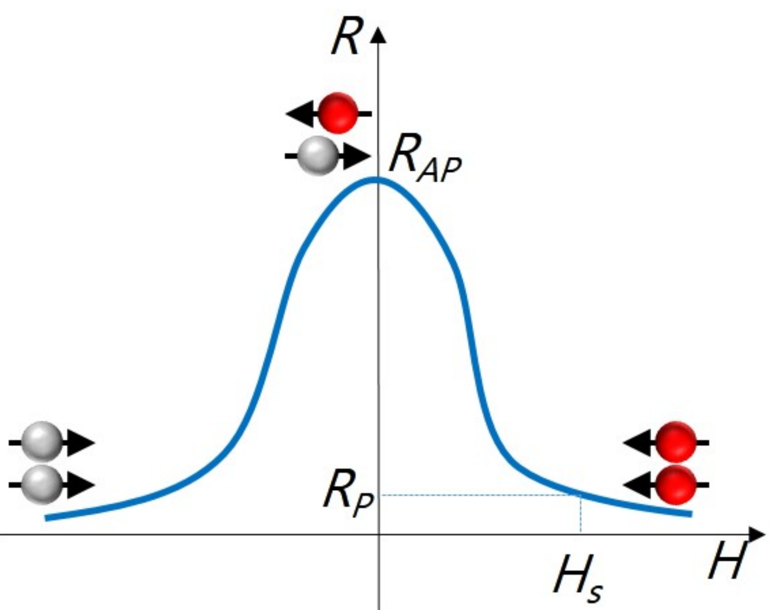

Figure 1-3. Schematic example of GMR behavior (at multi layers of thin film) with perpendicular magnetic field. The GMR is present for ferromagnetic layers which are separated by a non-magnetic or an antiferromagnetic metallic thin film. (H_s: saturation magnetic field for parallel state of magnetization)

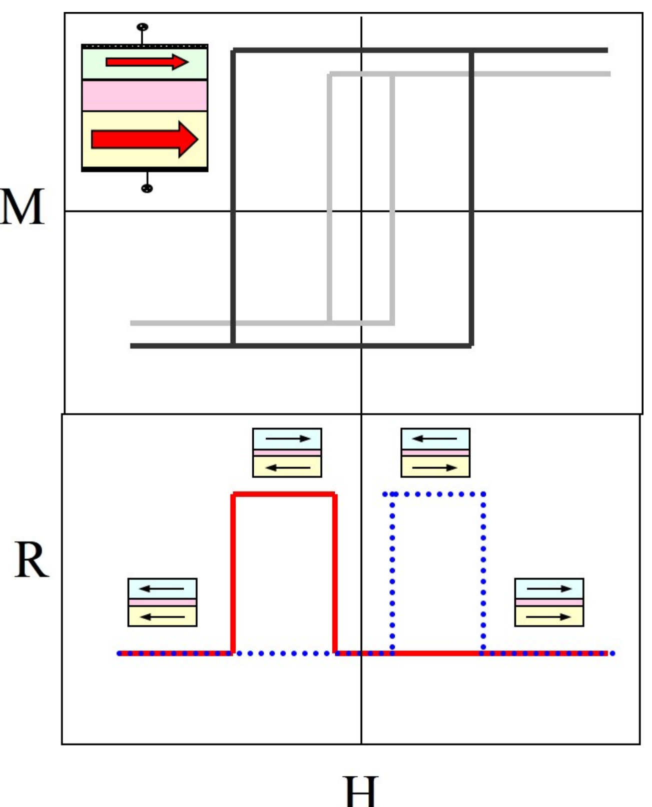

Figure 1-4. Schematic of ideal magnetoresistance curve of two FM layer with spacer material as a function of in-plane external magnetic field sweep. The two FM layers have different coercive field with different field dependent magnetization behavior (upper graph). And because of the different coercive field, field dependent resistance shows two times of different resistance change during the field sweep (below *R* vs *H* graph).

Figure 1-5. Two types of GMR devices. Current in plane (CIP) and Current perpendicular to plane (CPP)

Similar to the GMR phenomenon, there is a tunneling magnetoresistance (TMR) phenomenon in which an insulator material (tunnel barrier) is introduced instead of a non-magnetic material in a layer between ferromagnetic (FM) materials. In this TMR device, thickness of the tunnel barrier must be small enough to allow quantum mechanical tunneling. The use of this TMR phenomenon is magnetic tunnel junction (MTJ). MTJ is one of the most representative devices in the field of spintronics, and this is currently used in various industry fields such as magnetic sensors and magnetic memories.

The TMR phenomenon appears as a result of spin dependent tunneling (SDT) that the electrons tunneling through the insulating barrier is affected by the relative orientation of magnetic electrodes. The probability that electrons can tunnel depends on the density of state (DOS) or on the fermi wave vector at the fermi level. In magnetic materials, exchange splitting of the energy band changes the electron DOS for each spin direction and the tunneling probability is determined accordingly. The relative quantification of the SDT is called tunneling spin polarization (TSP), and its physical meaning is the relative amount of electrons having aligned spins in a specific direction among the all tunneling electrons[6].

The spin direction is not related with the DOS at non-magnetic material, so the number of conducting electrons and mean free path does not depends on the electron spin. But, at magnetic materials, DOS can be differ for each spin direction. Especially, when the DOS near the Fermi level has a large spin dependency, the electron movement is greatly influenced by the spin direction. Leading to the spin dependent transport. Spin dependent scattering, which leads to GMR, or spin dependent tunneling (SDT) phenomenon, which causes TMR phenomenon, occurs in a magnetic / non-magnetic multilayer film device[6].

Based on GMR or TMR behavior, spin valve structure was developed for the effective spin injection and detection. Since the discovery of GMRs in 1988[4, 5], efforts have been made for the industrial use of GMR phenomena. In 1985, Johnson and Silsbee introduced the concept of non-local spin valve device. They reported non-equilibrium spin injection from a ferromagnet to a non-magnetic film (Aluminum) over the spin diffusion length of the order of 1μm (several hundred μm for pure Al). A schematic illustration of spin injection and detection device that consists of a non-magnetic metal N connected to the ferromagnets of the injector F1 and detector F2, as shown in figure 1-6 (a) and (b)[7]. Rather long spin diffusion length led to the proposal of a spin injection technique using a F1/N/F2 structure. The output voltage at F2 depends on the relative orientation of the magnetizations of F1 and F2. The oxide tunnel barrier has generally been inserted in between ferromagnetic thin film and non-magnetic channel film to promote efficient spin injection (figure 1-6 (b) yellow color). The geometry shown in figure 1-6 is referred to a 4-terminal non-local lateral spin valve device. Normally, spin injection and detection experiment has been performed by using this geometry device to minimize the local signal and to achieve rather pure spin current signal than 3- or 2-terminal geometry. Because the 2-teminal geometry

can have local Hall effect and magnetoresistance effect, it will decrease the spin accumulation signal and the artifact can be detected. And the 3-terminal geometry case, one electrode is shared for a spin injection and detection. So the 3-terminal geometry also have controversy of artifact effect. But the 4-terminal geometry device, current will flow only one side of the channel and negligible current will flow through the other side of voltage probes.

Also we can measure the Hanle effect of spin precession with out-of-plane magnetic field and confirm again the spin injection through the non-magnetic material. In this 4-terminal geometry, a charge current (I) is passed through a ferromagnetic electrode F1 into the normal metal (non-magnetic) N and normal metal channel to the left (figure 1-6 (a) and (b)). Because of the ferromagnetic material F1, this current I injects spin polarized electrons into to normal metal (non-magnetic) channel and creating non-equilibrium spin-up and spin-down electrochemical potentials shown in figure 1-6 (c). This non-equilibrium electron spin will diffuse away from the injection electrode through the normal metal channel. And the spin accumulations detected by measuring the voltage V between F2 and N. There are no voltage (or current) source on the right side of the device, only spin-polarized current will flow to the right side of the device and creating spin accumulation. The magnetizations of F1 and F2 can be aligned ether parallel or antiparallel depending on the applied magnetic field. Thus, the non-local resistance and spin diffusion signal can be detected by the voltage V (between F2 and N) as shown in figure 1-6 (d) and (e). Accordingly, the spin and charge current are transported separately in the device[7]. The length scale called spin diffusion (or relaxation) length (λ_s) can be defined $\lambda_s = \sqrt{D\tau_s}$ where D is the diffusion constant and τ_s is the spin life time.

In the 4-terminal geometry, the length (L) between spin injection electrode and spin detection electrode is generally designed to be less than spin diffusion length. Then we can expect the Hanle effect (spin precession) signal detection with external (perpendicular to the sample plane) magnetic field. The polarized electron spin (normally parallel to the thin film plane direction) will injected into the non-magnetic channel and the polarized spins will precess with Larmor frequency by external perpendicular magnetic field. Then the injected polarized spins will lose its direction due to this spin precession phenomena. Resulting phenomena of spin relaxation process according to the spin precession will decrease the spin accumulation signal (non-local voltage signal). Schematic of injected spin state (near zero field) and spin precession state at external magnetic field are shown figure 1-7 with measured voltage (typical Lorentz shape)[8-10]. The typical Hanle effect decay the net spin accumulation with applying perpendicular magnetic field (to spin). At Hanle curve of Lorentz shape, Larmor precession frequency (ω_L) and spin life time (τ) can be extracted from full width half maximum (FWHM; $\omega_L = 1/\tau$) of Lorentzian fit[8-10]. The spin precession frequency, Larmor frequency is given by $\omega_L = g\mu_B B/\hbar$,where g is the g-factor for electrons, μ_B is the Bohr magneton and $g\mu_B/2$ is the spin

magnetic moment associated with the spin angular momentum S (S = 1/2) and $\hbar$ is the reduced Plank's constant[8-10].

The spin precession in ballistic transport regime, modulation of the spin signal by external magnetic field will show perfect cosine function by the relative parallel and anti-parallel magnetization between the injector and detector electrodes. But the spin precession in diffusive transport regime, the spins reaching the detector from the injector is not unique and the diffusing electrons can take different paths to reach the detector electrode. So the spin precession signal has both the oscillatory and decay component which dampens the oscillation in diffusive regime[11]. In the figure 1-8, experimental detection of spin precession behavior (Hanle curve) is shown in diffusive regime.

There are other spin current manipulation (injection and detection) method can be used except spin valve device with GMR or TMR phenomenon. We can use thermal spin behavior such as Spin Seebeck effect, Spin–dependent Seebeck effect, Seebeck spin tunneling and we can use spin orbit coupling (SOC) related behavior such as spin Hall effect (& inverse spin Hall effect), spin Galvanic effect, photo-spin voltaic effect, Rashba SOC induced Spin FET (Spin valve transistor) etc. Among them, next chapter, we will focus on spin orbit coupling (SOC) & spin Hall effect (SHE) and related effect (especially related in 2-D materials) which are mainly contributed in this thesis experiment.

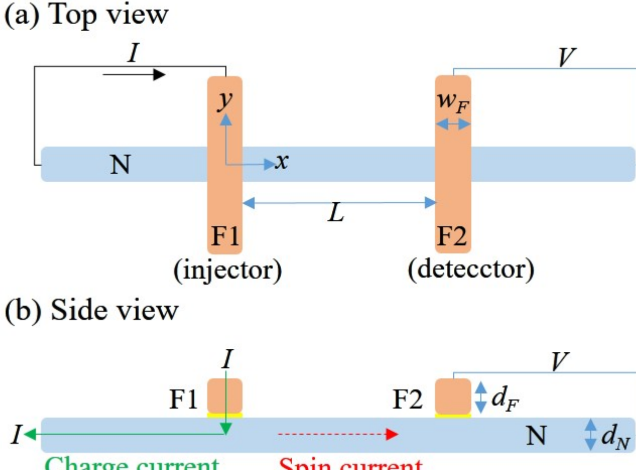

(c) Electrochemical potential (ECP) in N

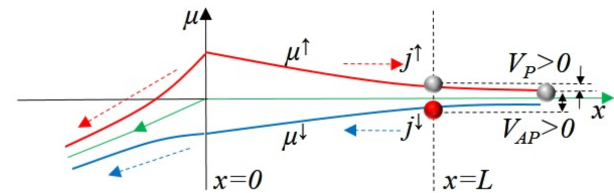

(d) Detection of spin accumulation by F2

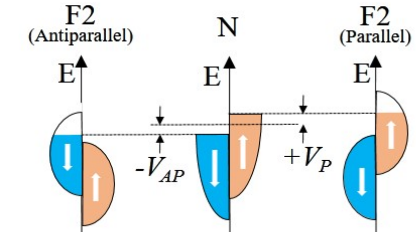

(e) Nonlocal resistance and spin accumulation signal

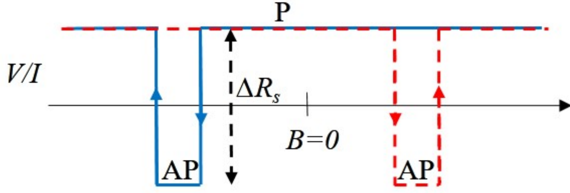

Figure 1-6. Non-local spin injection and detection at spin valve device[7]. (a) Top view. (b) Side view. Current I is sent from F1 to the left end of N. The spin accumulation at $x = L$ is proves by measuring voltage V at F2. (c) Spatial variation of the ECP for up-and down-spin electrons in N. (d) Densities of states for the up- and down-spin bands in N (center) and F2 (left and right). (e) Non-local resistance V/I as a function of in-plane magnetic field B, where P and AP represent the parallel and antiparallel orientations of magnetizations in F1 and F2 (reproduced from reference 7).

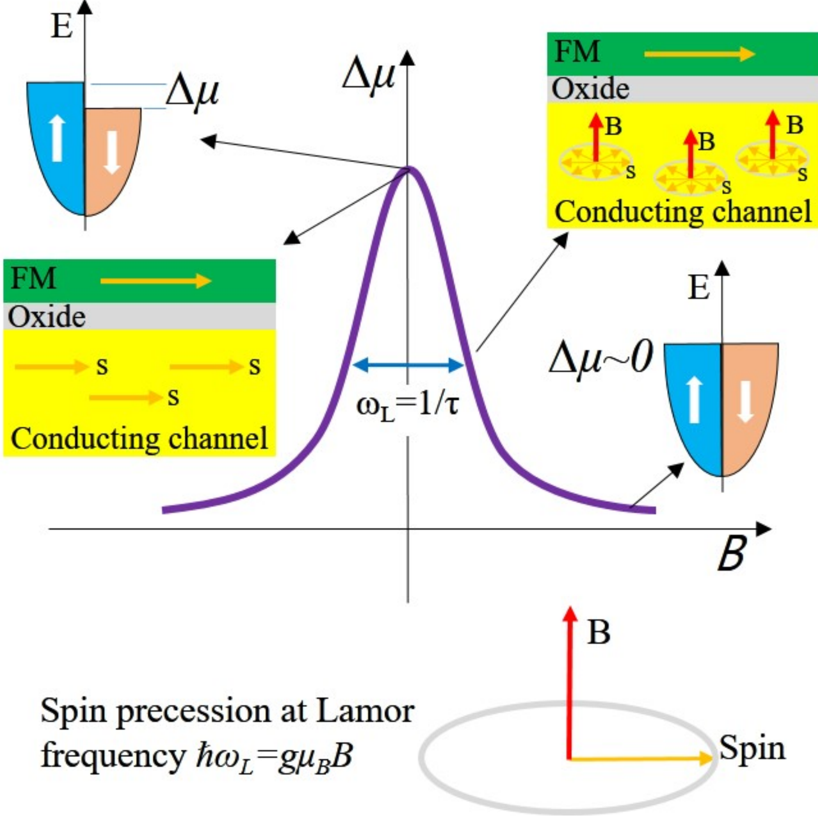

Figure 1-7. Schematic illustration of the Hanle effect at ferromagnet/tunnel barrier/conducting channel junction device. This allows manipulation of the spin polarization by applying magnetic field perpendicular to the spins. The spin accumulation (near the zero magnetic field) gradually reduces to zero with increasing magnetic field. (at $B = 0$, static spin polarization and maximum spin accumulation, at $B \neq 0$, spin precession, and suppressed spin accumulation)[8-10].

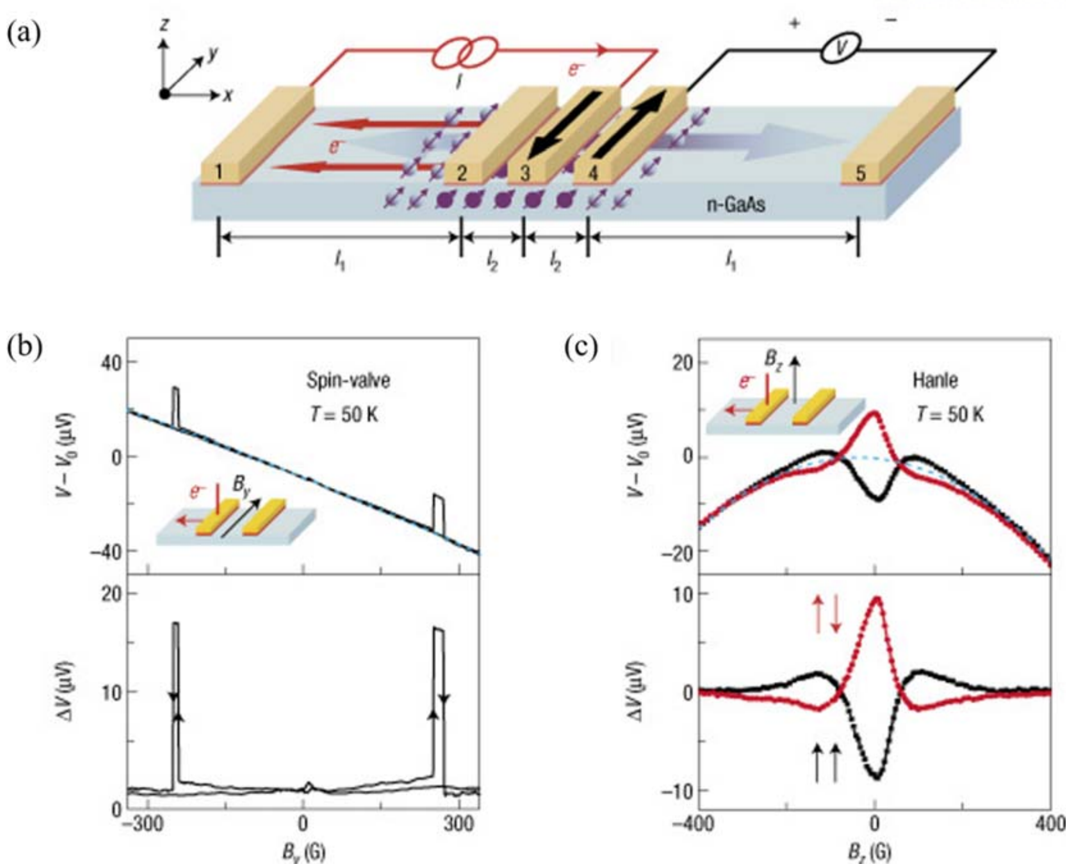

Figure 1-8. An example of the experimental detection about representative non-local lateral spin valve and Hanle effect[12]. (a) A schematic diagram of the non-local experiment (not to scale). The large arrows indicate the magnetizations of the source and detector. The two different contact separations are 160 μm and 12 μm. Electrons are injected along the path shown in red. The injected spins (purple) diffuse in either direction from contact 3. The non-local voltage is detected at contact 4. Other choices of source and detector among contacts 2, 3 and 4 are also possible. (b) Non-local voltage, $V_{4,5}$, versus in-plane magnetic field, B_y, (swept in both directions) for sample A at a current I = 1.0 mA and T = 50 K. The raw data are shown in the upper panel (with an offset V_0 = -30.227 mV subtracted). The background (dashed cyan curve underneath the data) is fitted by a second-order polynomial. The lower panel shows the data with this background subtracted. (c) Non-local voltage, $\mathbf{V_{4,5}}$, versus perpendicular magnetic field, B_z, for the same contacts and bias conditions (and the same offset V_0) as in b. The data in the lower panel have the background (dashed cyan curve in the upper panel) subtracted. The data shown in black are obtained with the magnetizations of contacts 3 and 4 parallel, and the data shown in red are obtained in the antiparallel configuration (reproduced from reference 12).

1.4 Spin relaxation mechanism.

Spin relaxation is the processes that bring an unbalanced population of spin states into equilibrium states. In spintronics, spin relaxation is considerably important since spintronics has serious concern for using spin polarization. If the injected spins can maintain its information for reliable time, it can protect against random or depolarization (maintain long spin diffusion length). In a solid, spin relaxation will turn up with the interaction between the electron and environment affects such as effective magnetic field which interacts with spin and changes its orientation. The effective magnetic field in a solid arises from the spin of other electrons and holes, nuclear spin, phonons (lattice vibrations) that gives time dependent magnetic field, and spin orbit interactions.

Commonly there are 4 major types of relaxation process[13-15]. i) Elliot-Yafet mechanism, ii) D'yakonov-Perel' mechanism, iii) Bir-Aronov-Pikus mechanism, iv) Hyperfine interaction.

i) Elliot-Yaffet (EY) mechanism

This is the case of spin scattering accompanied by momentum scattering. In this case, spin scattering increases with bigger spin orbit interaction. This EY mechanism is often observed in low mobility materials such as organics. In this EY mechanisms, the spin relaxation time τ_{EY} has direct proportionality to elastic scattering time τ.

$$\tau_{\mathrm{EY}} \sim \tau / (\Delta g)^2$$

where Δg is a difference between the electrons g factor in the solid and that of free electrons.

ii) D'yakonov-Perel' (DP) mechanism

This DP mechanism come out at inversion asymmetry materials such as InAs, GaAs and bilayer graphene. If any given solids with inversion symmetry breaking because of its crystalline structure or an externally applied electric field, then an electron in the solid will experiences strong spin-orbit interactions. Dresselhaus and Rashba spin orbit interactions lift the degeneracy between the up spin and down spin states. Both interactions truly behave like effective magnetic field. In the DP scenario, the spin relaxation time should be inversely proportional to the elastic scattering time.

$$\tau_{\mathrm{DP}} \sim 1/\tau$$

iii) Bir-Aronov-Pikus (BAP) mechanism[15]

This is the case of spin scattering by interaction between electron and hole. It is spin relaxation of electrons in semiconductors where there is a significant concentration of both electrons and holes. The wavafunction overlap between electron and hole cause an exchange interaction between them. If the

hole's spin flip, then the exchange interaction will cause the electron's spin to flip as well, leading to spin relaxation.

iv) Hyperfine interaction mechanism.

The nuclear spins generate an effective magnetic field which interacts with electron spins via this hyperfine interaction mechanisms, resulting in spin relaxation[15]. There are interaction between nuclear with limited nuclear spin and other particle in atom (molecule), electrostatic interactions between the electric nuclear dipole moment of an atomic nuclear and surrounding electrons, interaction between the magnetic moment of an atomic nuclear and the magnetic moment of an electron, and interaction of magnetic moments of atomic nuclear. Hyperfine interaction does no cause complete loss of electron spin polarization.

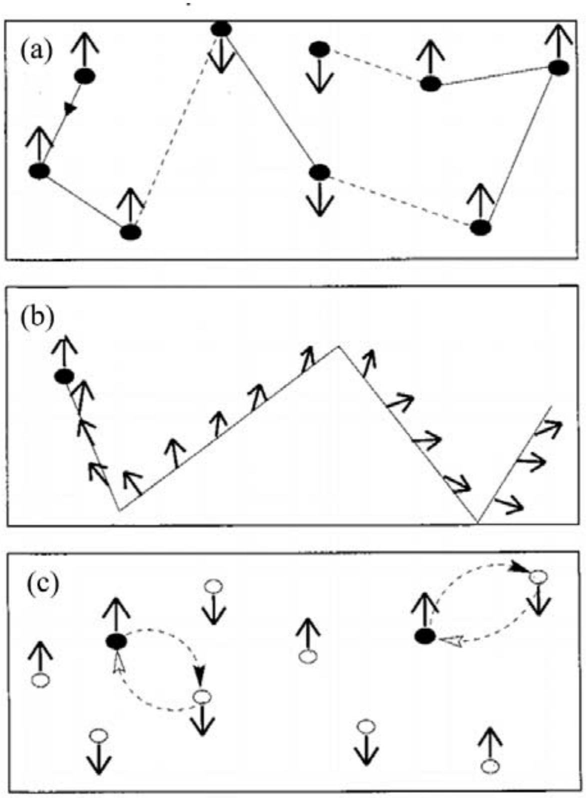

Figure 1-9. Relevant spin relaxation mechanisms for conduction electrons[15]. (a) The Elliott–Yafet mechanism. The periodic spin-orbit interaction makes the spin ‘‘up’’ Bloch states contain small spin-down amplitude, and vice versa. Impurities, boundaries, and phonons can induce transitions between spin ‘‘up’’ and ‘‘down’’ leading to depolarization of spin. (b) The D’yakonov–Perel’ mechanism. In non-centrosymmetric crystals spin bands are no longer degenerate: in the same momentum state spin up has different energy than spin down. This is equivalent to having internal magnetic fields depending on, electron’s momentum. The spin of an electron precesses along such a field, until the electron momentum changes by impurity, boundary, or phonon scattering. Then the precession starts again, but along a different axis. Since the spin polarization changes during the precession, the scattering acts against the spin relaxation. (c) The Bir–Aronov–Pikus mechanism. The exchange interaction between electrons and holes causes the electron spins to precess along some effective magnetic field determined by hole spins. In the limit of strong hole spin relaxation, this effective field randomly changes before the full precession is completed, reducing the electron spin relaxation (reproduced from reference 15).

Chapter 2.

Spin Orbit Coupling & Spin Hall Effect

2.1 Spin Orbit Coupling (SOC)

Spin orbit coupling (SOC) is a relativistic interaction between electron's orbital angular momentum and its spin angular momentum. This SOC has great interest in spintronics because it allows to manipulate the electrons spin state without external magnetic field and it determines the spin relaxation (spin diffusion length or spin life time) in the material. The manipulation of SOC are key points for the spin Hall effect (SHE) or inverse spin Hall effect (ISHE). These days, the new branch of spintronics so called spin-orbitronics (spintronics with exploiting SOC) was introduced and have tremendous interests in research and future industry application. Figure 2-1 shows various applications of spin-orbitronics[16].

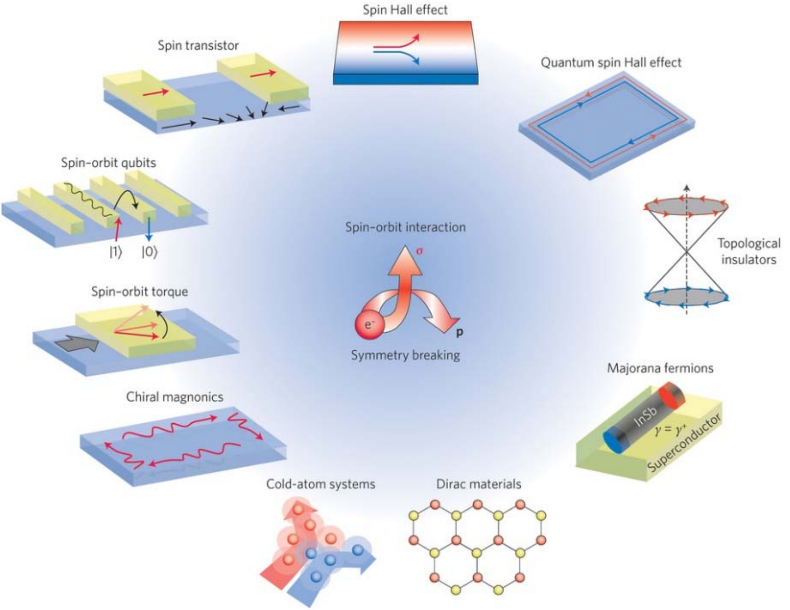

Figure 2-1. Various applications of Spin-orbitronics[16]. If there is a spin-orbital coupling phenomenon due to broken inversion symmetry in some systems, a unique characteristic that can realize spin-orbitronics appears. In other words, spin-orbitronics is an electronic device field realized by controlling the spin-orbit coupling phenomenon. As shown in this figure, the magnetization direction and the spin direction of the material or device can be electrically controlled (using spin-orbit coupling phenomenon) and a desired state is realized as a device (reproduced from reference 16).

To understand SOC briefly, first think about the system which contains number of atoms in a magnetic field. The energy for the system can be represented by a Hamiltonian (H) consisting of kinetic energy, potential energy, etc.

$$H = H_{kinetic} + H_{potential} + H_{Zeeman} + H_{dia} + H_{so} + H_{exchange} + H_{demag} + H_{anisotropy} + \ldots$$

Among them, consider the H_{so} term. For a charge particle move with a velocity $\vec{v}$ in an electric field, there are effective magnetic field $\vec{B}_{eff}$ (Lorentz transformation of E) is exist. A particle in an electric field experiences an internal effective magnetic field in its moving frame. If an electron is moving around the nucleus, but in the frame of electron, it feels the nucleus is moving around the electron. $I = Ze/\tau = Zev/2\pi r$, where $\tau = 2\pi r/v$ and a magnetic field created in the center can be expressed $B = \mu_0 I/2r = \mu_0 Zev/4\pi r^2$ with $r = a_0/Z$, and $v \approx \hbar/mr$ (m is the mass of electron and the Z is atomic number). And $E_{so} = -\vec{\mu}\cdot\vec{B} = \mu_B \cdot \vec{B} \approx \mu_0 \mu_B^2 Z^4 / 4\pi a_0^3$. So the effective SOC term H_{so} which is the interaction between orbital angular momentum (L) and spin angular momentum (S) can be expressed as $H_{so} = \lambda \vec{L}\cdot\vec{S}$, and effective field is $\vec{B}_{eff} = \dfrac{\vec{E}\times\vec{p}}{4mc^2}$

$$H_{SO} = -\mu_B \vec{\sigma}\cdot\vec{B}_{eff} = \mu_B \vec{\sigma}\cdot\left(\frac{\vec{E}\times\vec{p}}{4m_0 c^2}\right) = -\frac{e\hbar}{4m_0^2 c^2}\vec{\sigma}\cdot\left(\vec{E}\times\vec{p}\right)$$

where c is the velocity of light and σ is the Pauli spin matrices vector. Often, we can use notation as $H_{so} = \eta_{SO}\sigma\cdot(k\times\nabla V)$, and the SOC constant is $\eta_{SO} = (\hbar/mc)^2 \approx 3.7\times10^{-6}\,\mathring{A}$. Experimentally, the electrical resistivity and the spin diffusion length are important parameter for spin and charge transport devices. If we know a resistivity (ρ_N) and a spin diffusion length (λ_N) of a material, we can obtain SOC parameter of $\bar{\eta}_{SO}$ [17],

$$\bar{\eta}_{SO} = \frac{3\sqrt{3}\pi}{4\sqrt{2}}\frac{1}{k_F^2}\frac{h}{e^2}\frac{1}{\rho_N \lambda_N}$$

where the k_F is the Fermi momentum and $h/e^2 \approx 25.8$ kΩ. This value $\bar{\eta}_{SO}$ extracted from the spin injection method are larger than the value of η_{SO} (from the free-electron model).

When the atomic number is increased, the SOC also increased. Light atoms such as C, Si have very week SOC and heavy atoms such as Pt, W, Au have very strong SOC. For example, if there is a light element film with doped heavy atoms impurity, then we can expect that doped heavy atoms will make the dominant SOC induced current or electron transport.

The effective SOC, which is main source of spin Hall effect (SHE) or inverse spin Hall effect (ISHE),

can be categorized as two different types. One is intrinsic SOC from the effective field due to periodic potential, the other is extrinsic SOC from the effective field due to non-periodic potential.

i) Intrinsic SOC

The intrinsic spin orbit coupling (SOC) arise in the absence of impurities. This intrinsic SOC will come from symmetry breakings. A certain symmetry such as time reversal symmetry and crystal inversion symmetry is lost, then the spin orbit interaction is realized without any impurities.

Effect of breaking of time reversal symmetry can be explained by wave function and phase movement[6]. When an quantum mechanical system come back to the original position after some movement, there is a phenomenon that remembers the process. And the memory will come out on a phase of quantum mechanical wave function. That is referred as the topological phase or Berry's phase. Electron's trajectory changes when this topological phase information changes. And the change of topological phase information is different for each electron spin. If SOC is involved in, the SHE will take place. In other words, quantum mechanical amplitude changes when there is SOC. The quantum mechanical amplitude difference between the case of "with SOC" and the case of "without SOC" is called the Berry phase, and the Berry phase includes the wave function representing the state of electron condition. If this wave function is influenced by the SOC and changes in the energy band of the spin-up/-down electrons, then the velocity of the electrons is not determined completely by the group velocity and are affected by unusual (abnormal) velocity of the new finite value which is proportional to the Berry curvature. This unusual velocity has dependence of spin and the appearance of spin trajectory which deviates from the electron trajectory predicted by the group velocity is changes by the spin direction[6]

The intrinsic mechanism by structure inversion symmetry breaking can be explained by the crystal structure's inversion asymmetry in materials.

$$H_{so,\mathrm{int}} = \eta_{so}\sigma \cdot \left(k \times \nabla_L V\right) = \frac{1}{2}\sigma \cdot B(k)$$

Here, *B(k)* is the k-dependence magnetic field in the electronic band. At the structure inversion asymmetry, the spin splitting can appear. In the band structure with dispersion relation near the fermi surface, there are no spin up and down splitting exists in free electron case (shown in the left of figure 2-2). In the presence of external magnetic field, the Zeeman energy splits spin up and down electron as shown in figure 2-2. And in the case of Rashba spin splitting, the electron up and down spins split through the k-space (through the sample surface) because of 2D structure inversion asymmetry as shown in the right of figure 2-2. This kind of special spin splitting can appear not only in the interface of heterostructure but also in 2D materials such as graphene (mono and bilayer), MoS_2 and other transition metal dichalcogenides (TMDs) as shown in figure 2-3. These spin splitting can be also

controlled by applying external electric field.

Structure inversion asymmetry induced SOC can be classified into two category. One is the inversion symmetry breaking in bulk structure, which is Dresselhaus SOC, and the other is inversion symmetry breaking in 2-dimensional boundary such as surface state and heterostructure interface, which is Rashba SOC. Figure 2-4 shows the spin texture of Rashba and Dresselhaus state at the Fermi surface. The Rashba SOC at 2-dimensional state, will discuss detailed at chapter 2.2.

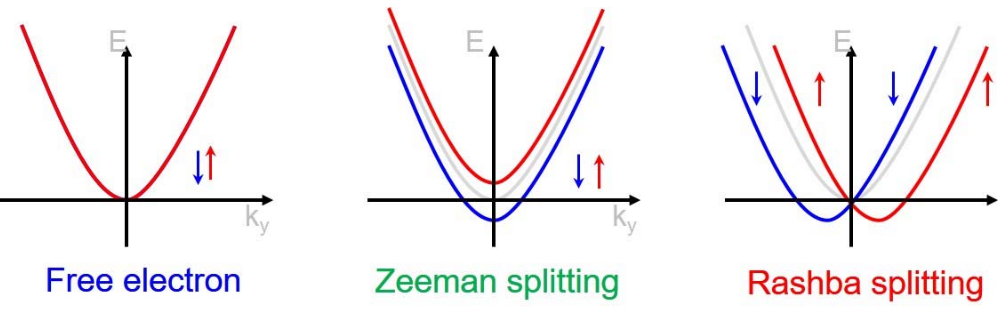

Figure 2-2. Comparison of the band structure (dispersion relation) of the free electron, Zeeman spin splitting and Rashba spin splitting.

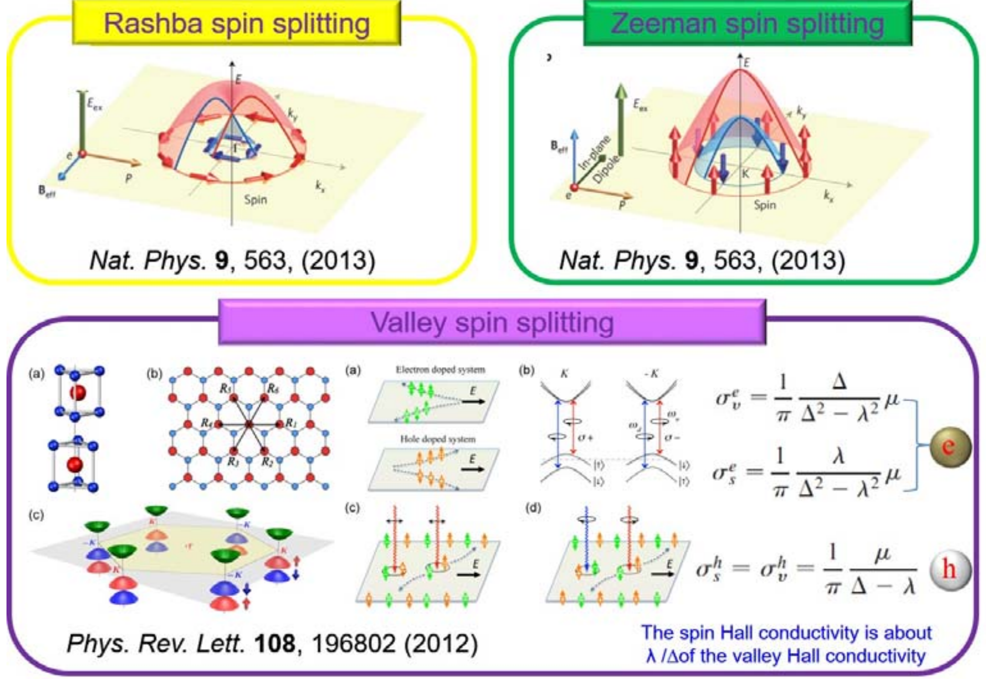

Figure 2-3. Comparison of the three kind of spin splitting, Rashba spin splitting, Zeeman spin splitting and valley spin splitting[18, 19]

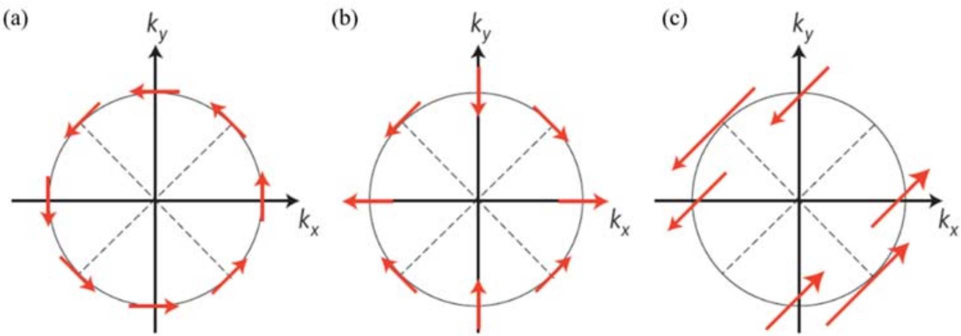

Figure 2-4. Spin texture at the fermi surface. (a) Rashba (2-dimensional SOC at the interface or surface), (b) Dresselhause (3-dimensional SOC at the bulk materials), (c) Rashba plus Dresselhaus

Intrinsic SOC	Extrinsic SOC
from the effective field due to periodic potential $H_{so,\mathrm{int}} = \eta_{so}\sigma\cdot(k\times\nabla U_L) = \frac{1}{2}\sigma\cdot B(k)$ k-dependnece magnetic field in the electronic band Turn from partial inversion symmetry breaking	from the effective field due to non-periodic potential (impurity, etc) $H_{so,\mathrm{ext}} = -\eta_{so}\sigma\cdot(k\times\nabla V)$
Dresselhaus spin orbit coupling ~ bulk (crystal) inversion asymmetry - Zinc-blende lattices of GaAs and InSb - Internal electric field from Coulomb potential gradient (atomic) Rashba spin orbit coupling ~ structural inversion asymmetry - Surface state or heterostructures - External gate bias applied on the 2D electron gas (2DEG) - Electrically controllable ~ device applications	Scattering center Carrier Skew Scattering δr Scattering center Carrier Side-Jump Scattering
S. Zhang, *Phys. Rev. Lett.* **85**, 393 (2000) S. Murakami et al, *Science* **301**, 1348 (2003) J. Sinova et al, *Phys. Rev. Lett.* **92**, 126603 (2004)	Smit, *Physica* **24**, 39 (1958) Berger, *Phys. Rev. B* **2**, 4559 (1970)

Figure 2-5. Comparison of intrinsic SOC and extrinsic SOC. In this figure, the intrinsic SOC from structural inversion symmetry and extrinsic SOC were introduced which is closely related with this thesis experiment.

ii) Extrinsic SOC

The extrinsic SOC arises from the non-periodic component by impurities.

$$H_{so,\mathrm{ext}} = \eta_{so}\sigma \cdot \left(k \times \nabla V\right)$$

There are Mott-skew scattering and Side jump mechanism for the extrinsic SHE. When an electron scatter with impurities, a charge of scattering angle depends on the spin of electron is the Mott-skew (skew) scattering mechanism. And when electron undergoes lateral displacement depends on spin state is the Side-jump mechanism. Figure 2-5 shows the comparison of intrinsic structure SOC mechanism and extrinsic SOC mechanism.

In Mott-skew scattering mechanism, consider the impurity atom (black dot) is in a space and electron is moving (black, blue and red narrows) through the impurity atom as shown in figure 2-6. Black narrows represents the spin electrons' scattering trajectory by potential energy of impurity atom without SOC event (V). The total scattering potential energy of the impurity atom is

$$V_{eff} = V(r) + \frac{1}{2m^2c^2r}\frac{dV}{dr}\mathrm{L} \cdot \mathrm{S}$$

The second term in above equation contains the electron spin s. So Electron feels the different potential energy depends on electron spin[6]. Let's consider the scattering of the spin-up electrons (red arrows) with the electron spin direction coming out of the plane as shown in figure 2-6. The spin-up electrons feel as if they are receiving a magnetic field in the direction coming out of the plane by L · S. Potential energy due to SOC makes repulsion stronger when electron scattering is up direction (red arrow at the upward) and repulsion less stronger when electron scattering is down direction (red arrow at the downward) [6]. In other words, when the scattering angles of the electron momentum are changed, the spin up electrons (red arrows) are more scattered upward when the upward and downward scattering cases are averaged. This is the same result as the electron trajectory is bent upward by the magnetic field coming out from the plane[6]. On the contrary, let's consider the scattering of the spin-down electrons (blue arrows) with the electron spin direction goes into the plane. The spin-down electrons feel as if they are receiving a magnetic field in the direction goes in from the plane. At this time, the potential energy due to SOC makes repulsion stronger when electron scattering is down direction (blue arrow at the downward) and makes repulsion less stronger when electron scattering is up direction (blue arrow at the upward) [6]. Like the preceding, when the scattering angles of the electron momentum are changed, the spin-down electrons (blue arrows) are more scattered downward when the upward and downward scattering cases are averaged. This is the same result as the electron trajectory is bent downward by the magnetic field goes into the plane. This effect of varying the average direction in which the electron trajectory is bent by the electron spin direction is the Mott-skew scattering mechanism[6].

In Side-jump mechanism, electron undergoes lateral displacement during impurity scattering. In

other words, Side-jump mechanism is one origin of SHE due to the Berry phase coming out near an impurity during the scattering event by impurity (which have strong SOC). When the impurity atoms produce a Berry phase, the phase of the electron wave function changes by the Berry phase, and the magnitude varies with the amount of momentum. The additional fact that the Berry phase varies with the value of the momentum means that the position where plane waves interfere constructively with each other has changed[6]. As shown in figure 2-7, depends on the case of an up-spin (red arrow) with the electron spin direction coming out of the plane and the case of a down-spin (blue arrow) with the electron spin direction goes in from the plane, wave packet changes the positon left or right without changing the trajectory direction. At that time, the relative phase difference (between the plane waves constituting the wave group) changes as the position causing the constructive interference (due to the Berry phase) [6].

This mechanism is similar with Mott-skew scattering mechanism at the point of impurity scattering. But Mott-skew scattering changes the scattering angle and Side-jump mechanism just move the trajectory left or right side without affecting scattering angle[6].

In this chapter, we have studied the spin-orbit coupling, and have outlined the basic principle that causes SHE or ISHE. The mechanism of spin-orbit coupling is briefly summarized in figure 2-8. In the next chapter 2.2, the Rashba SOC which appears in some conductive interface (2DEG) is investigated (the Rashba SOC is strongly related with my experiment), and the resulting SHE/ISHE with their applications are introduced in the next chapter 2-3.

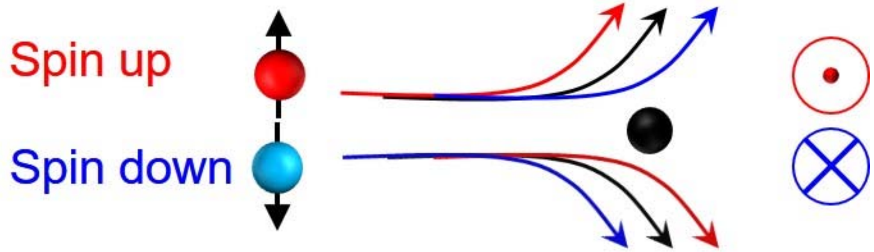

Figure 2-6. Schematic of Mott-skew scattering mechanism of extrinsic SOC. Spin up and down electrons changes its scattering angle by the impurity[6].

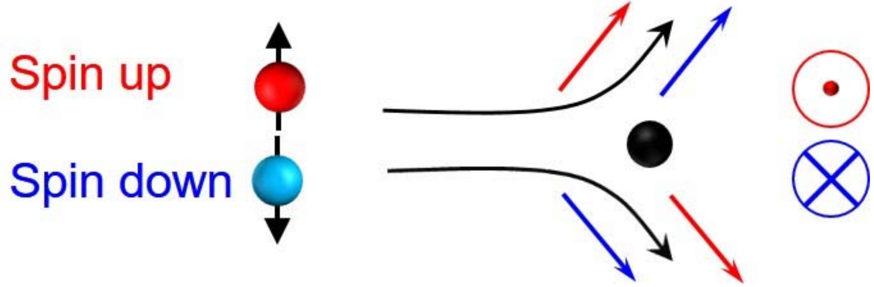

Figure 2-7. Schematic of Side-jump machanism of extrinics SOC. Spin up and down electrons undergoes lateral displacement during scattering event by the impurity[6].

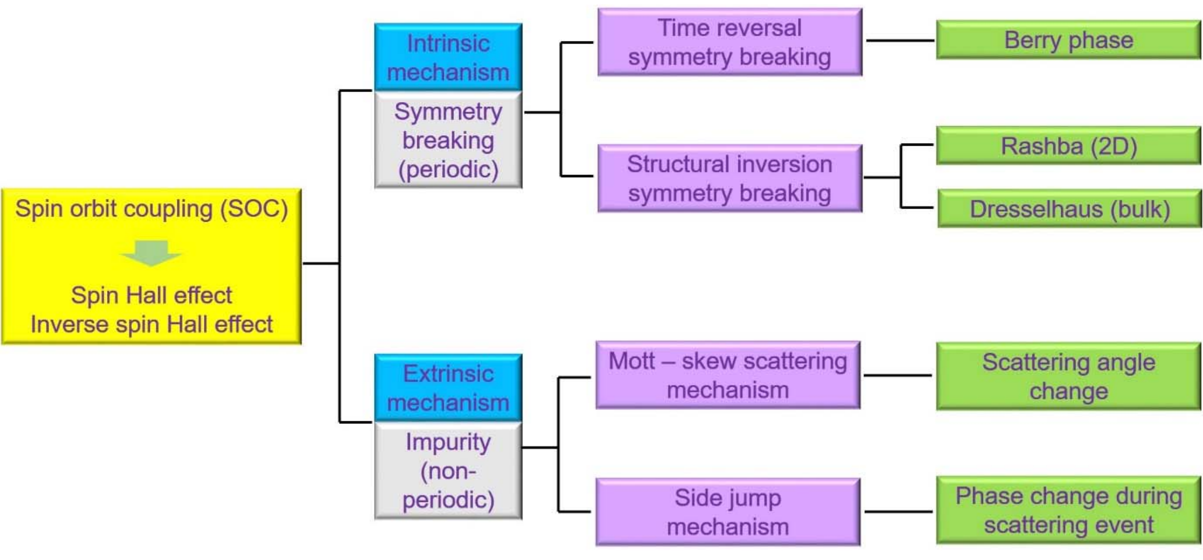

Figure 2-8. Summary of SOC and its phenomenon (spin Hall and inverse spin Hall effect) mechanism

2.2 SOC at 2D – Rashba SOC

As explained in chapter 2.1, Rashba SOC (or Rashba-Dresselhaus) is a specific phenomenon by a structural inversion asymmetry. In this chapter, Rashba SOC will be discussed in detail because the Rashba SOC is closely related to the main experiment of this thesis dissertation.

In 1984, E. Rashba proposed an effect that could be explained by effective Hamiltonian $H_R = \alpha_R(\vec{\sigma} \times \vec{P}) \cdot \vec{Z}$ through the analysis of symmetry[20]. After then, important things have been proved about the Rashba effect through several supporting research and modification: The Rashba effect corresponds to the case where the inversion symmetry is broken, ie, when there is an internal inherent electric field. And electric dipole moment $\vec{P}$ can create energy with coupling the electric field. The created energy can be expressed as $H_L = -\alpha_K(\vec{L} \times \vec{K}) \cdot \vec{E}$, and this energy plays a decisive role in the intrinsic SHE[20]. In addition, the SOC Hamiltonian $\hat{H}_{SOC} = \alpha\vec{L} \cdot \vec{S}$ act as important role in the Rashba effect ($\hat{H}_{SOC}$ causes the Rashba effect to increase according to the atomic number)[21], so the effective Hamiltonian describing the Rashba effect is now represented by

$$\hat{H}_{eff} = \alpha\vec{L} \cdot \vec{S} - \alpha_K(\vec{L} \times \vec{K}) \cdot \vec{E} .$$

This equation accurately expresses “band splitting”, “increasing depends on atomic number”, “chiral spin/chiral spin direction”, “asymmetrical charge distribution” and “existence of orbital angular moment” which are necessary to explain the Rashba phenomenon[21-25].

This Rashba phenomenon occurs in a 2-dimensional system where the inversion symmetry is broken and an internal electric field exists. In some systems, the inversion symmetry breaking can be exist at the three example cases. First is the surface of solid. The solid surface has a solid state on one side and a vacuum on the other side, so the inversion symmetry is considerably broken. There is always a strong electric field on the surface of the solid, which prevents the electrons from leaving the solids. Second is interface between two materials. There are also very strong electric fields at the interface between the two materials because there are different materials on both sides with structural inversion symmetry breaking at interface. For example, LAO/STO interface, which is the main topic of this thesis, has strong Rashba SOC at the conducting interface with structural inversion asymmetry. Third, there is an inversion asymmetry in the crystal structure itself. If the material is an insulator, an electric field may be present inside the material such as Zinc blend structure material, InAs etc with structural inversion asymmetry. This case corresponds to the inversion symmetry breaking of the 3-dimensional structure and is found by Dresselhaus (called the Dresselhaus effect) [21].

When the phenomenon of atomic orbital interference occurs due to the inversion asymmetry, the

orbital angular momentum is inclined at a certain angle and the charge density is distributed asymmetrically. This asymmetrical charge distribution makes electric dipole moment which means the existence of internal electric field. In other words, the system which has an internal electric field with inversion asymmetry has finite strength of Rashba effect even though it is small quantity.

As shown in figure 2-2, spin-up/down electrons are split through the planar direction due to inversion asymmetry and cause Rashba SOC. This Rashba SOC can generally be expressed by Rashba Hamiltonian H_R, spin splitting energy Δ_R, and Rashba field B_R,

$$H_R = \alpha(\hat{n} \times \vec{K}) \cdot \vec{S}$$

$$\Delta_R = 2\alpha k_F$$

$$B_R = 2\alpha k_F / (g\mu_B)$$

where α is the Rashba SOC constant which is proportional to internal electric field $E_{\circ}$ and external voltage (electric field) V_g .

$$\alpha = g\mu_B \frac{\hbar}{2mc^2}(E_0 + \frac{V_g}{d})$$

This Rashba SOC with external electric field (gate voltage) can be studied by several method. For example, J. Nitta et al studied the Shubnikov-de Haas (SdH) oscillation with beating pattern at the InAlAs/InAs interface and calculated the Rashba SOC (in 1997)[26]. SdH oscillation can be observed in the longitudinal resistance as a function of perpendicular magnetic field. Electrons under the influence of the magnetic field move in a cyclotron motion, then the wave nature of the electrons leads to quantization, which is visible in the resistance. SdH oscillation is one of the way to obtain the Rashba SOC parameter with measuring the beating pattern. The beating pattern in the SdH oscillation comes from the spin split of two Fermi circle (Rashba splitting) in momentum space. But the beating also come from the magneto inter-sub-band scattering (MIS) by the second sub-band in a QW[27]. The beating pattern due to MIS can be exclude when the fermi energy obtained from the carrier density range is much below the second sub-band energy level. So this SdH oscillation can be obtained by certain carrier density range and relatively high mobility condition at quantum well (QW) site. The beat patterns from the SdH oscillation observed in InAlAs/InAs QW can be attributed to the spin splitting[26]. The spin splitting energy Δ is inversely proportional to the number of oscillation between two nodes when the total number of electrons is held constant. The oscillation frequency reflects the electron carrier concentration. As a result, spin splitting energy Δ which can be attributed to surface electric field increased by applying negative gate voltage which decrease the carrier concentration and therefore decrease the Fermi wave number k_F. From that, the spin orbit interaction parameter α increased and suggest that the Rashba mechanism is dominant.

Another example, in 1990, Datta and Das suggested spin-FET device using Rashba SOC[28]. This is new approach different from conventional FET (figure 2-9). In the conventional FET, the external gate voltage control only the size of the electron density by using the metal electrode with the source and drain. But the spin-FET uses the magnetic metal as spin injector & detector and control the direction of the electron spin with gate voltage (spin precession control), then obtain an electron spin signal at the spin-detector. In this case, it is possible to drive the device by only a small number of directional electron spins, and the electron density to be applied can be reduced, and the magnitude of the gate voltage also has wide selection range. So this spin-FET has a high possibility of development.

Figure 2-10 shows a report on the modulation of the measured voltage due to the spin precession motion by changing the external magnetic field & gate voltage using a well-known 2D material (2D quantum well)[29]. The applied external voltage is perpendicular to the sample by the upper gate electrode, so the Rashba field is applied through the sample surface direction (y direction in the drawing). Thus, whether the electron spin precesses (or not) depends on the external magnetic field direction. When the direction of the electron spin from the magnetic material (one electrode) to the 2DEG is in same direction (B_y), the electrons are transferred to the other electrode without the precession of the electron spin. But when the direction of the electron spin from the magnetic material (one electrode) to the 2DEG is in different direction (B_x), the electrons injected into the 2DEG are subjected to a spin precession motion, which oscillates the voltage of the measured electrode. In particular, this measure voltage oscillation characteristic can be obtained when the distance between the spin injection electrode and the detection electrode is within a ballistic transport regime.

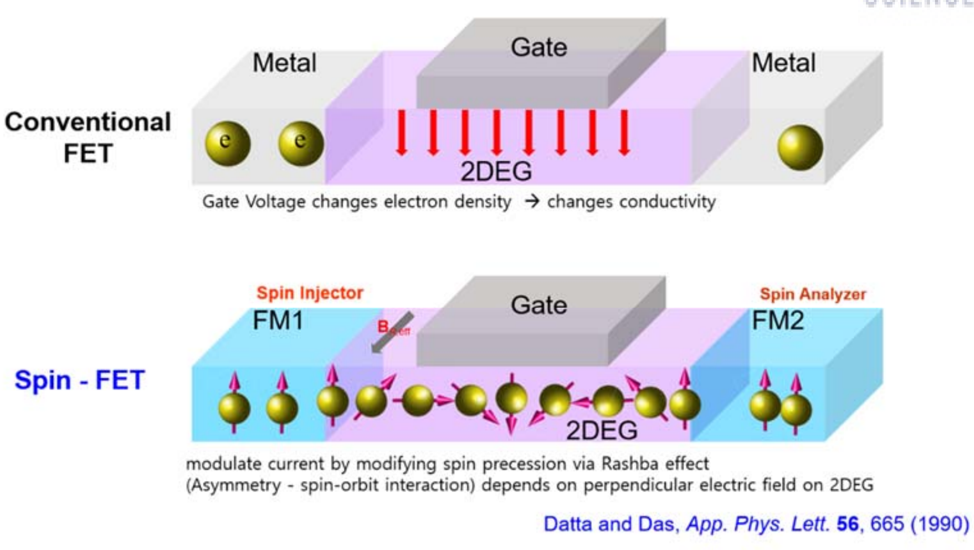

Figure 2-9.Comparison of conventional FET and spin-FET. Conventional FET just flows the electron (or hole) charge depends on the gate voltage, Spin-FET flows electron spin with controlling the electron spin direction by the gate voltage.

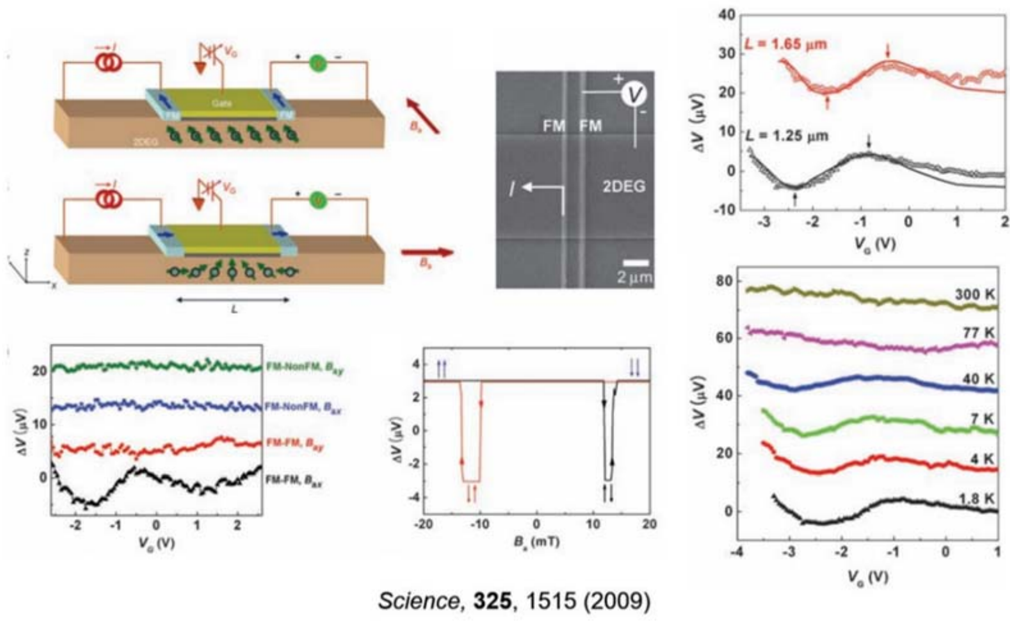

Figure 2-10. Experimental detection of Spin-FET[29]. By applying top gate voltage and external field, the voltage modulation is detected (reproduced from reference 29).

On the extension of this Rashba phenomenon, there are Rashba-Edelstein effect (REE) / Inverse Rashba-Edelstein effect (IREE) exist. These effect can appear with current flow (or voltage) through conductive 2D surface, it can expressed as current induced spin accumulation (REE) or spin induced charge accumulation (IREE). In REE, charge current in Rashba 2DEG system is atomically associated with a non-zero spin accumulation. And IREE is the generation of charge current carried by the interfacial states in response to the non-zero spin density induced by spin injection. This effect was suggested Edelstein at 1990[30]. He 1st showed that direct charge current J passing through the sample can induce spin polarization of conduction electrons. And he explain that this REE is a kinetic analogy of the well-known magneto-electric effect (MEE) in antiferromagnetic insulator. Figure 2-11 shows the schematic illustration of current induced spin accumulation at Rashba interface (Rashba spin splitting interface). Compare with spin Hall effect (or Inverse spin Hall effect), both are current induce spin accumulation (or spin to charge conversion), but SHE (or ISHE) can appear in bulk material (with presence of SOC) and REE (or IREE) can be shown at interface or surface (in case of Rashba type SOC).

In 2013, A. Fert group introduce experiments demonstrating a large spin to charge conversion by the Bi/Ag Rashba interface as shown in figure 2-12. They used NiFe as a ferromagnetic layer and Bi/Ag bilayer as a Rashba interface, and inject spin current from NiFe layer into the Rashba interface by using spin pumping and identify the characteristic signature of an IREE. The non-zero spin density generate chare current (voltage difference). And they introduce an IREE length (λ_{IREE}) characterizing the conversion between the injected spin current into a 2D current[31]. $\lambda_{IREE} = j_C / j_S$, where j_c and j_s are charge current density ($j_c = Ic/a$) and spin current density. Also IREE length can be expressed as $\lambda_{IREE} = \alpha_R \tau_S / \hbar$ and they proved that the j_c of IREE is different from the j_c of ISHE.

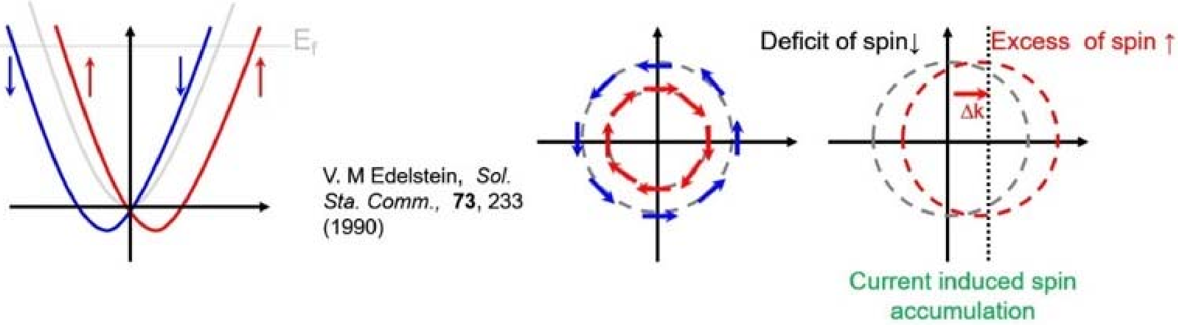

Figure 2-11. Schematic band structure of Rashba and Rashba-Edelstein effect. When current is applied into the Rashba interface, there are deficit of spin down and excess of spin up state (Δk) will appear and the spin accumulation can be exist.

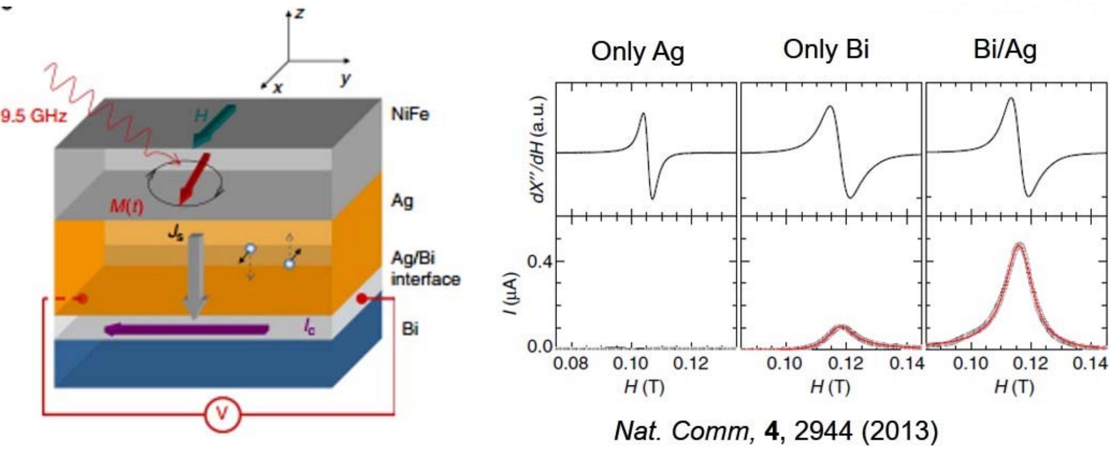

Figure 2-12. Experimental detection of Inverse Rashba-Edelstein Effect (IREE)[31]. The efficient conversion from spin-to charge current found at the Ag/Bi interface shows that the REE could be a major tool for the generation and detection of spin currents or magnetization control (reproduced from reference 31).

When non-equilibrium of electron spin state is exist at the Rashba interface, then there are Spin Galvanic Effect (SGE) or Inverse Spin Galvanic Effect (ISGE) can be appear. SGE is spin polarized charge flow from non-equilibrium electron spin state and ISGE is the non-equilibrium spin density by inversion asymmetry. Conventional Rashba interface just split the up and down spin through the k-space and has equilibrium spin up and down state. But the Spin Galvanic effect (SGE) is induced by non-equilibrium spin polarized state. This is introduced by S. D. Ganichev et al. using circularly polarized terahertz radiation at 2002[32]. This SGE can be explained by three consecutive process shown in figure 2-13. First the two spin up and down sub-bands are shifted in momentum space with different spin state. And it begins with preferential occupation of one of the spin split sub-bands resulting from such as spin injection. Second, four quantitatively different k-dependent spin flip scattering transitions appear. The scattering rates depend on the wave vectors of the initial and final states. The blue arrows represent that the same rates of spin flip transitions preserve the symmetric distribution of carriers in each sub bands. And the broken red arrows represent that two scattering processes are not equivalent and generate asymmetric carrier distribution in both sub bands. Third the current is caused by the k-dependent spin flip relaxation process (second part) and it will relaxes towards equilibrium state[33-36] .

And the SGE differs from other experiments such as spin –voltaic effect where spin current is caused by gradient of potentials, concentrations etc. Recently, some groups are reported experimental detection of the complementary spin-Hall and inverse spin Galvanic effect torques and robust spin-orbit torque and spin Galvanic effect at ferromagnet/semiconductor bilayers (figure 2-14)[37, 38].

Also this spin Galvanic effect (SGE) usually compared with the Circular Photo Galvanic effect (CPGE). Both have the current flow driven by and asymmetric distribution of carriers in k-space in systems with lifted spin degeneracy due to k-linear terms in Hamiltonian. Both effects contribute to the current occurring in the plane of quantum wells. But the SGE is caused by asymmetric spin-flip scattering of spin polarized carriers and it is determined by the process of spin relaxation. And the CPGE is the result of selective photoexcitation of carriers in k-space with circularly polarized light due to optical selection rules. In some optical experiments the photo current may represent a sum of both effects; selective photo excitation of carriers in k-space and in-plane component of non-equilibrium spin polarization. In that experiment, CPGE can be ignored when they use circularly polarized radiation at normal incidence[33-36].

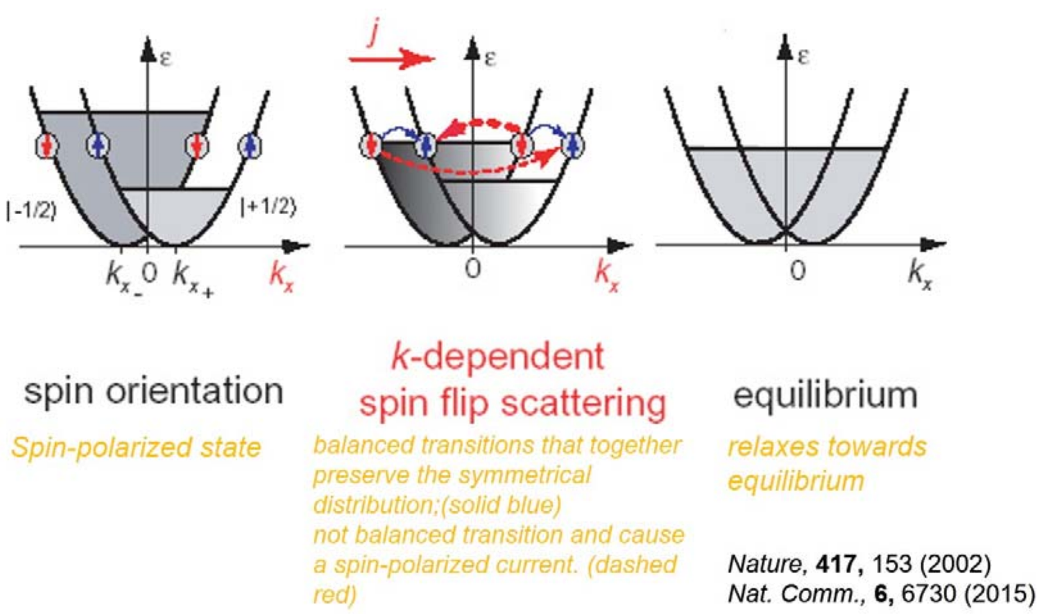

Figure 2-13. The Spin Galvanic effect (SGE). SGE arises from asymmetric electron relaxation in a spin-split conduction band. Initially, spin polarized state (left) relaxes towards equilibrium (right) by means of four types of spin flip transition (center). The solid blue arrows indicate balanced transitions that together preserve the symmetrical distribution. But transitions shown by dashed red arrows do not balance causing a spin-polarized current[33-36].

Figure 2-14. Complementary spin Hall and inverse spin Galvanic effect torques (up) and the detection of robust spin orbit torque/spin Galvanic effect (down) (reproduced from reference 37, 38)[37, 38]

2.3 Spin Hall effect (SHE) & Inverse Spin Hall effect (ISHE)

History

As already mentioned in previous chapter 2-1, Spin Hall effect (SHE) and Inverse Spin Hall Effect (ISHE) are a group of phenomena result from spin orbit coupling (SOC). SHE/ISHE can be associated with variety of spin orbit mechanisms, such as intrinsic or extrinsic from the variations of some symmetry, geometry, impurity, band structure and carrier density etc. This SHE/ISHE was predicted by D'yakonov and Perel' in 1971[39, 40]. Then Hirsch named "spin Hall effect' at 1999. The effect is similar with the conventional Hall effect that is opposite sign of charges will accumulate at the transverse side edge (to the sample plane) of the current flow due to Lorenz force in a magnetic field (figure 2-15 left). Instead of charge accumulation at the transverse side, SHE represents polarized electron spin accumulation at the transverse side (figure 2-15 right and figure 2-16).

The first observations of spin dependent scattering in solids were measurements of anomalous Hall effect (AHE) in ferromagnetic materials[41]. That was the experimental proof that the electron spins are having transverse force when they are moving (SHE). The AHE originates from the interaction between the spin and orbital motion of electrons in metals or semiconductors. Up and down spin electrons are strongly imbalanced in ferromagnets, thus both spin and charge currents are generated in the transverse direction by AHE.

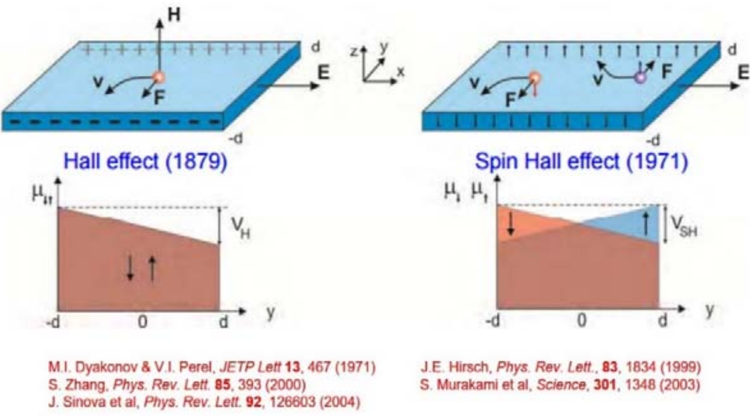

Figure 2-15. (left) Hall Effect (right) spin Hall effect. In the Hall effect, magnetic field B and the associated Lorentz force *F* generate transverse charge accumulation with opposite direction for electron and hole. And the electrochemical potential of spin up and down carriers are the same. A voltage difference between the two edges is built up. In the spin Hall effect, spin accumulation with opposite direction for up and down spin can be generated by the spin orbit coupling without magnetic field. And the electrochemical potential for spin up and down carrier is different. There are no measured voltage difference between two edges will show but spin orientation dependent voltage exist.

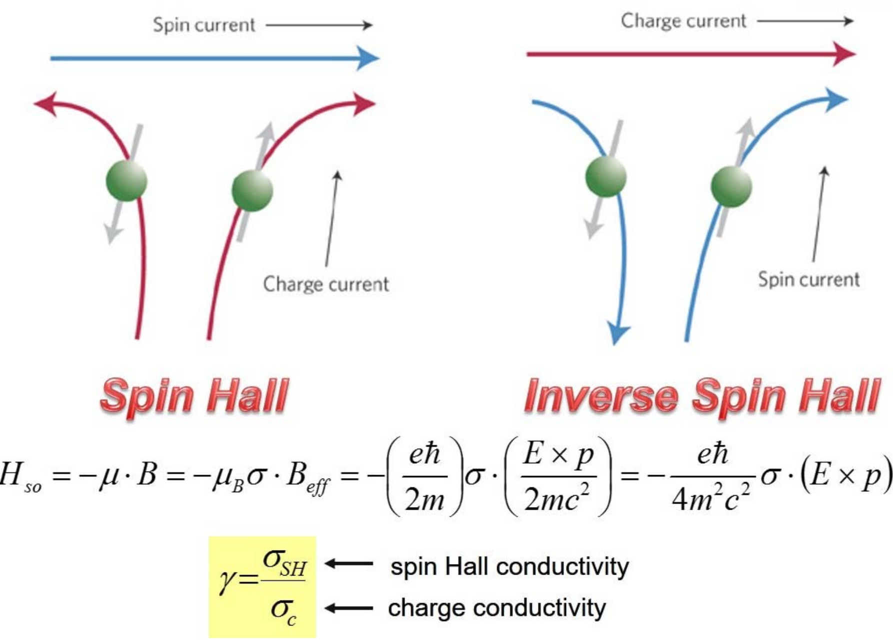

Figure 2-16. Schematic of spin Hall effect (SHE) and inverse spin Hall effect (ISHE) which are represents conversion charge current transverse spin current (SHE) and from spin current to transverse charge current (ISHE). Spin Hall constant γ (= spin Hall angle) can be define as spin Hall conductivity σ_{SH} divide by charge conductivity σ_C.

The Hall effect family

There are some phenomena associated with the Hall effect (called them hall effect family).

Before and after Hall (HE) and spin Hall effect (SHE) was discovered, there are various related or similar concept of phenomenon such as anomalous Hall effect (AHE), quantum Hall effect (QHE), quantum spin Hall effect (QSHE), and Quantum anomalous Hall effect (QAHE) was introduced (figure 2-17). As already introduced above, the HE represents transverse built-in potential by magnetic field and SHE represents generation of transverse spin current by SOC. And the AHE is the combined version of HE and SHE (both Hall voltage and spin accumulation). Further, there are only the edge charge current flowing in the presence of external magnetic field, in QHE (insulator version of HE). The QSHE results from the combined SOC and time reversal symmetry, so that there are only the edge spin current flowing (Insulator version of SHE). And if there are the SOC with time reversal symmetry breaking in some material, then both spin and charge edge current can exist which is QAHE (insulator version of AHE).

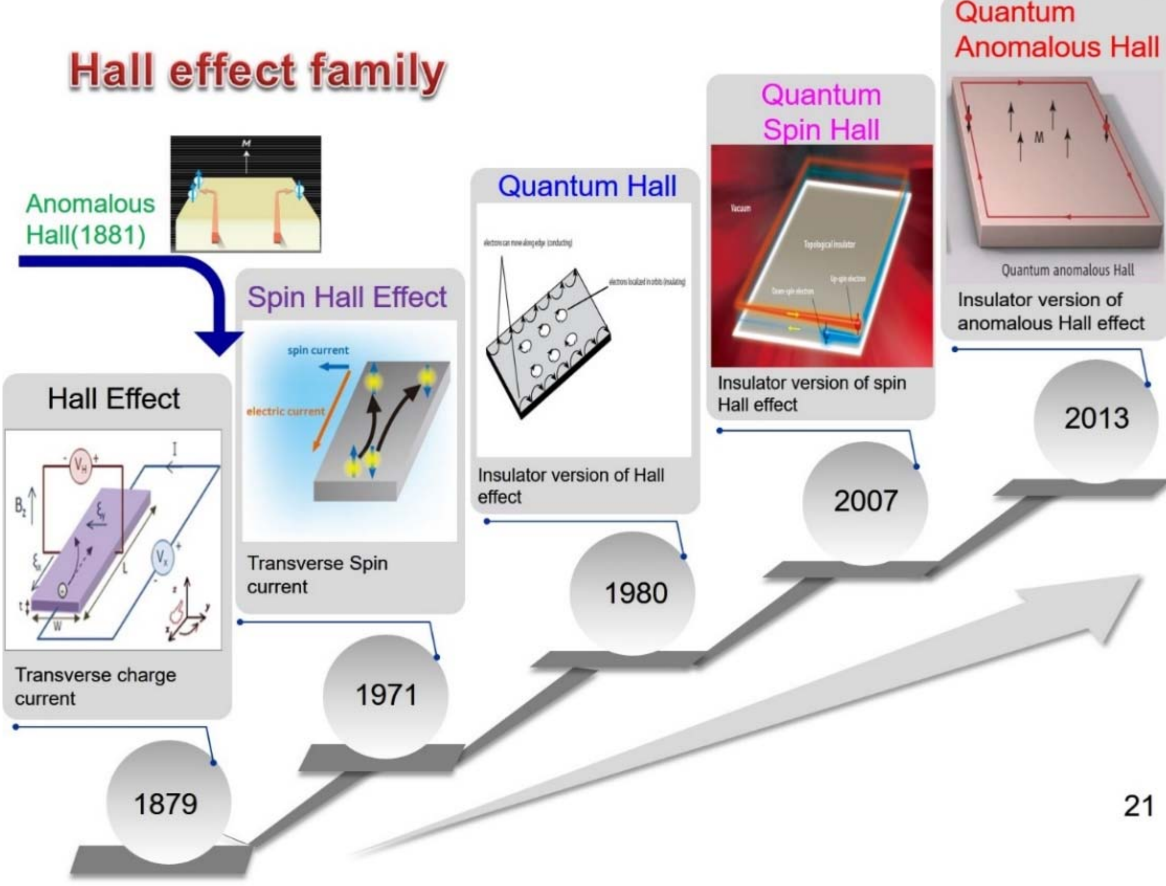

Figure 2-17. Hall effect family. After Hall effect was discovered at 1879, various Hall effect related or similar phenomenon were introduced and proved by experiment.

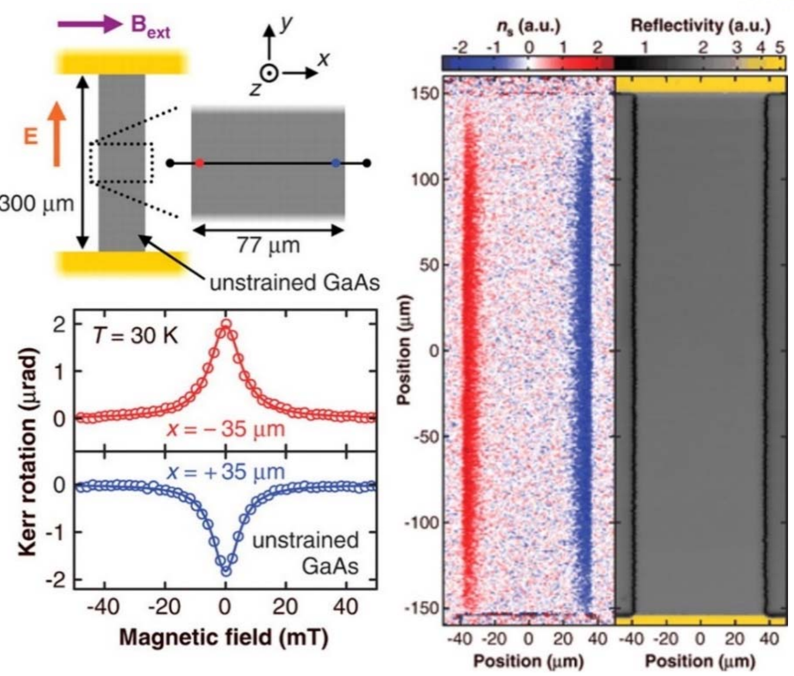

Figure 2-18. First experimental observation of direct spin Hall effect (SHE)[42]. They used GaAs semiconductor sample and optically detected spin polarization by Kerr rotation microscopy (reproduced from reference 42).

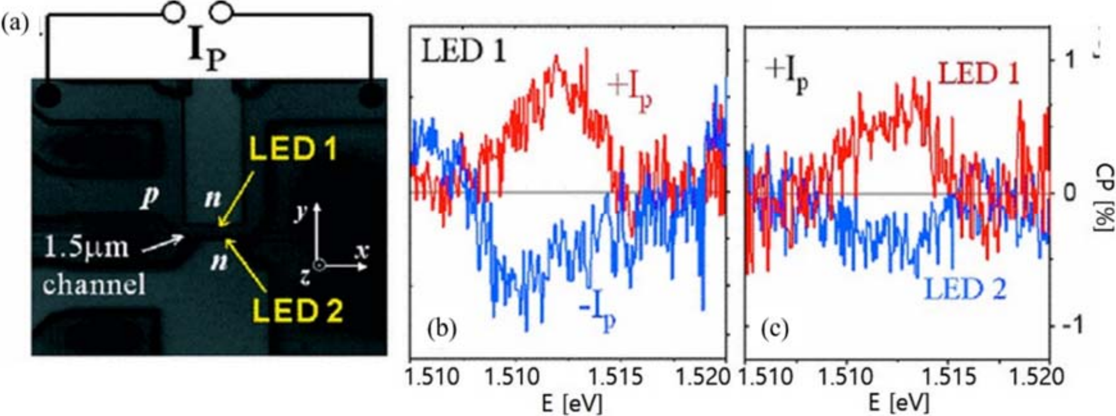

Figure 2-19. The SHE measurement using LED[43]. (a) Scanning electron microscopy image of the SHE LED device. (b) Polarization along z axis measured with active LED 1 for two opposite I_p current orientations. Spectral region of peak B of the high bias electroluminescence (EL) curve of wafer 1 is shown. Non-zero and opposite out-of-plane polarization for the two I_p orientations demonstrates the SHE. (c) Polarization along z axis measured with fixed I_p current and for biased LED 1 or LED 2. The data show opposite polarizations at opposite edges of the 2-dimensional hole gas (2DHG) channel confirming the SHE origin of the measured signal (reproduced from reference 43).

Experimental detection of SHE/ISHE

Coming back to SHE/ISHE, the first experimental observation of SHE in semiconductors were the measurements of spatially resolved electron spin polarization near the edges of n-type GaAs channels using Kerr rotation microscopy as shown figure 2-18[42]. And then, the evidence of SHE was also shown by the polarization of the recombination radiation of holes in a light emitting diode (LED) structure[43]. In the Ker rotation microscopy measurements[42], they used n-type GaAs samples grown by molecular beam epitaxy on semi-insulating GaAs substrates. And they flow current through the sample's longitudinal direction with transverse external field, then static Kerr rotation measurements were achieved with a pulsed Ti: sapphire laser tuned to the absorption edge of the semiconductor with normal incidence to the sample. The existence of spin accumulation close to the edge were shown at a 2-dimensional scan of the sample (figure 2-18 right). The polarization has opposite signs at two edges which represents different color (red and blue) as expected from the SHE[42].

After then, other experimental methods was introduced to measure the SHE/ISHE. One of them is EL measurement (as shown in figure 2-19). And others are magneto transport from FM material to normal metal, ferromagnetic resonance, and so on (figure 2-20). Normally, many of electrical detection is obtained by measuring SHE/ISHE with injecting spin polarized current from FM materials (figure 2-21, 2-22). That is non-local spin Hall effect geometry. In the device, they can obtain effectively large spin Hall parameter by using heavy metal/or alloy such as Au, Mo, Nb, Pd, PT, Pt Cu, PtAy as a spin transport materials[44-51]. From FM induced non-local SHE measurement SHE parameter can be obtained by calculating the equation

$$\Delta R_{SH} = \frac{P}{t_{Al}} \frac{\sigma_{SH}}{\sigma_C^2} exp(-L_{SH} / \lambda_{sf})$$

from reference [52] (figure 2-21) or

$$R_{SH} = \frac{\Delta R_{SH}}{2} sin\theta \quad , \quad \Delta R_{ISHE} = 2\alpha_H \frac{\rho_{Au}}{t_{Au}} P\, exp(-d / \lambda_{Au})$$

from reference [53] (figure 2-22).

In the non-local SHE measurements, without some special case such as 2D interface with a symmetry breaking or topological insulator with time reversal asymmetry, normally the mechanism of spin and charge current can be represented by extrinsic mechanism component at diffusive transport regime. So the Spin Hall parameter α_{SH} can defined $\alpha_{SH} = \alpha_{SJ} + \alpha_{SS}$ where α_{SJ} and α_{SS} represents SH parameter of side jump and SH parameter of skew scattering[17]. When the impurities have a narrow distribution of potentials with definite sign, as in doped impurities, the side jump conductivity is independent of the impurity concentration. By contrast, the skew scattering conductivity depends on the strength, sign, and distribution of impurity potentials, so the skew scattering contribution is dominant for SHE. Whereas when the impurity potentials are distributed with positive and negative contributions and their average

over the impurity distribution vanishes, then the side jump contribution is dominant. So the spin Hall parameter α_{SH} can be expressed as $\alpha_{SH} \approx \alpha_{SJ}\rho_N + \alpha_{SS}\rho^2_N$[17].

In this chapter, we focus on the experimental detection of SHE/ISHE by using ferromagnetic spin injector. In the chapter 2-4, I'd like to introduce experimental detection of SHE/ISHE without ferromagnetic materials which is one of my motivation of this thesis experiment.

Figure 2-20. Experimental detection method of SHE/ISHE

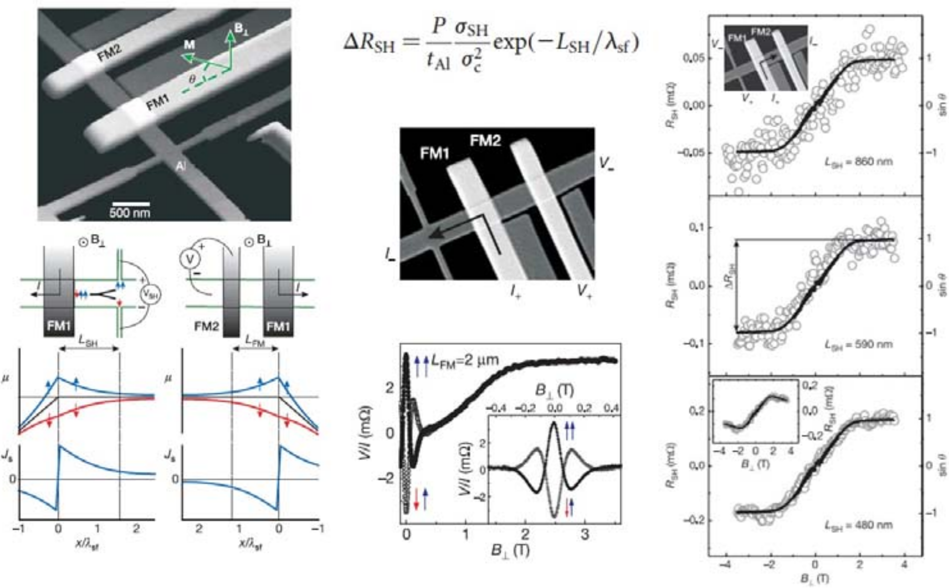

Figure 2-21. Example of SHE/ISHE detection measurement[52]. They measured not only spin Hall induced *R* vs perpendicular magnetic field curve (right side), but also spin precession signal (Hanle curve) by using non-local spin valve device geometry (center) (reproduced from reference 52).

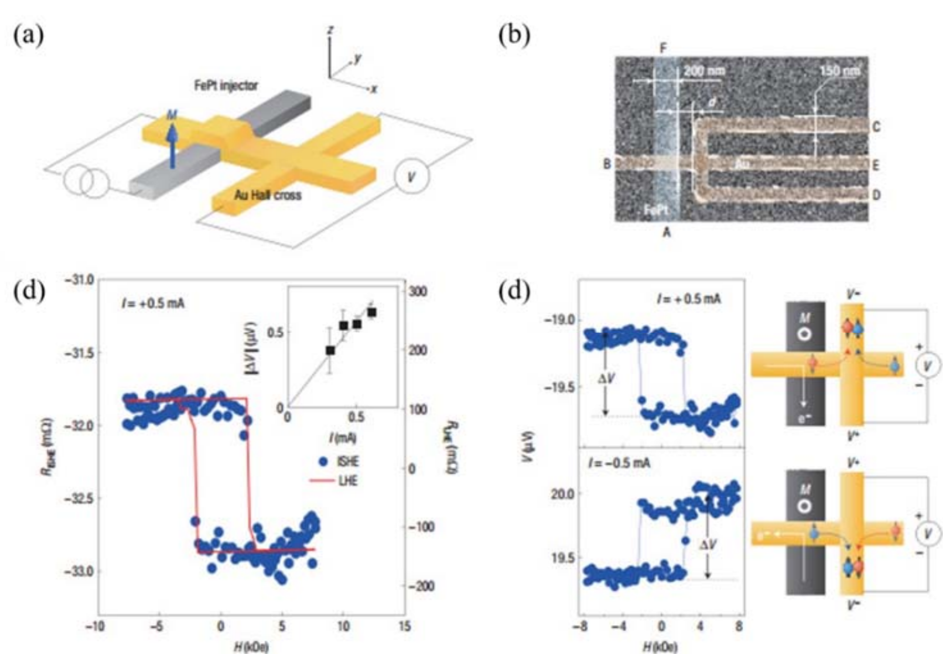

Figure 2-22. Example of SHE/ISHE detection measurement[53]. Using FM material, spin-polarized current was injected into the high SOC metal (Au), then the inverse spin Hall voltage signal was obtained displaying hysteresis behavior (reproduced from reference 53).

2.4 Detection of SHE without ferromagnetic materials

Conventional SOC and particular SOC in 2D materials (or 2D interface) and its SHE/ISHE were introduced above chapter 2.1-2.3. As introduced in chapter 2.3 about detection of SHE/ISHE, most of them were used transport methods by employing a ferromagnetic substance as a spin injection material, apart from the optical measurement method. In this chapter, a specific method about detection of SHE/ISHE using conducting material (or conducting interface) without FM materials will be introduced. This method corresponds to the method of controlling and detecting spin by using the spin Hall effect at the LAO/STO conductive interface which is the main experiment of this thesis.

Detection of SHE/ISHE without FM materials can be realized by using SOC effect twice. This was suggested by D. A. Abanin et al in 2009[54], and tried experimentally by Mihajlović et al[55]. Mihajlović et al used high SOC material of Au and made Hall bar structure. And their experiments have shown that the structure of the device (corresponding to the spin Hall region) must be designed in consideration of the ballistic transport region and the diffusion transport region when measuring the H-bar structure device. They fabricated Hall bar structure device with specific channel width and length (figure 2-23). If they applied current from one line then first SHE in the first Hall bar cross will appear and spin current will flow to the other Hall bar cross position through the channel (transverse direction of injected current). Then, spin current will generate charge current to the next vertical line by the ISHE at the other Hall bar cross. Thus, spin current induced non-local voltage will be detected at the next Hall bar line (next to the initial current flow line). This is the alternative method of detecting spin signal by using spin charge conversion twice. At this experiment, to minimize Ohmic signal by simple electron scattering or diffusion, channel length and width are very important. Channel width should longer than electron mean free path and shorter than electron spin diffusion length. This region is called spin Hall region. If channel width is much shorter than the electron mean free path, then electron will undergo ballistic transport (ballistic limit). And if channel width is much longer than spin diffusion length, then electron will experience diffusive transport with losing spin direction[54, 55]. Let's consider the Hall bar structure device of the non-magnetic metal as shown figure 2-23. The two adjacent parallel lines are connected with lateral channel with specific width w and length L. When a current is applied to one of two parallel lines, the non-local voltage can be measured on the other. In diffusive regime, where the width of the channel is greater than the mean free path of electrons, non-zero R_{nl} appears in non-local probes due to current spreading (figure 2-23 (a)). This magnitude of non-local resistance decay exponentially by increasing channel length. This follows van der paw (VDP) theorem at $L \geq W$ [54, 55]. $R_{nl}^{C} = R_{sq}\, exp(-\frac{\pi L}{W})$. R_{sq} is sheet resistance with resistivity and thickness t ($R_{sq} = \rho/t$). If channel width is in between mean free path and spin diffusion length (spin Hall region), non-local resistance by

spin Hall effect can be obtained by (figure 2-23 (b)). $R_{nl}^{SH} = \frac{1}{2}\gamma^2 R_{sq} \frac{W}{l_s} exp(-\frac{L}{l_s})$. This non-local resistance by SHE will also have positive value. Because created potential difference makes current flow opposite direction. (However, some research groups have recently been working on theoretical studies to show that the sign of non-local resistance can be experimentally differentiated depending on which SOC mechanisms are dominant, or depending on the interaction of the working SOC between orbital Hall effect and spin Hall effect.). Non-local resistance by SHE can be highly depends on channel length due to finite spin diffusion length. As shown in the equation, non-local resistance by SHE is proportional to square of SOC angle and inverse proportional to spin diffusion length and depends on channel length and width.

Similar to these studies, we can also employ experimental scheme of detecting SHE/ISHE with Hall bar type geometry. In 2010, Molenkamp group report detection of intrinsic SHE in ballistic transport region with Hall bar type geometry[56]. They used HeTe zero-gap semiconductor (HgTe/(Hg, Cd)Te quantum well) and measured non-local spin Hall voltage. And in 2013, Tomas Jungwirth group suggested new concept of combined spin-FET and SHE device shown in figure 2-24[57]. Spin current created by Hall bar geometry device region by SHE/ISHE transferred to the spin-FET region, then spin precession was created by gate voltage at the gated semiconductor channel (opposite process also possible). Large and clear voltage oscillation can be obtained by those process (figure 2-24) [57]. And J. Balakrishnan et al reported the experimental detection of SHE/ISHE induced non-local voltage and its enhancement with using 2D graphene channel material in 2013, 2014 (figure 2-25)[58, 59]. Graphene has hexagonal structure of 6 carbon atoms. And it has Dirac corn shape of energy dispersion relation at positions of k and k' in phase space. The mono layer graphene has very high mobility with limited defect or impurity. Along with low SOC, it can have high spin diffusion length. Low SOC constant is not enough to produce detectable non local voltage through the two time conversion of SHE/ISHE. Balakrishnan et al tried to increase SOC by irradiation electron beam to the surface of patterned graphene (figure 2-25). That is graphene hydrogenation (hydrogen impurity coupling with carbon atoms)[58]. They also attempt to increase SOC by doping impurity metal (high SOC metal) on a patterned graphene surface such as Au, Cu, Ag [59]. Also, they measured external magnetic field dependent non-local voltage behavior, which is spin precession effect (Hanle effect) already introduced at chapter 1. Generated spin current through the channel can undergo precession by external magnetic field. And the observed R vs B (resistance vs magnetic field) graph shows close to cosine function shape when the channel is ballistic transport regime. However, R vs B graph displays close to Lorentz shape with highest voltage at near zero field when the channel is in diffusive transport regime because oscillation component decrease by increasing magnetic field[11]. These reports showed Hanle curve close to Lorentz shape but non-local resistance signal live up to high field range (± 3T). The channel length dependent

non-local voltage signal curve can be fitted by the equation below[54, 55],

$$R_{nl}^{SH} = \frac{1}{2}\gamma^2 R_{sq} \frac{W}{l_s} \exp(-\frac{L}{l_s})$$

and magnetic field dependent non-local resistance graph can be fitted by

$$R_{nl}^{SH} = \frac{1}{2}\gamma^2 \rho \,\mathrm{Re}[(\sqrt{1+i\omega_B \tau_S} / \lambda_S) e^{-(\sqrt{1+i\omega_B \tau_S} / \lambda_S)|L|}]$$

So spin diffusion length of λ_s = ~1um, spin Hall angle (constant) γ = ~ 0.5 and spin diffusion length τ_s = λ_s^2/D = ~90 ps were obtained from fitting with above equations. Those results shows that small concentration of covalently bonded adatom on graphene can increase SOC without significant losing conductivity. This means SHE/ISHE can be manipulated by simple experimental method on graphene, thus graphene can be also used for spin-orbitronic application.

Additionally, we need to consider some point when we use Hall bar type geometry device for SHE/ISHE induced spin manipulation. One is the thermal effect. When flowing current or voltage through a material in a Hall bar structure, Seebeck, Peltier, Nernst and Ettingshaugen effects can occur depending on the presence or absence of an external magnetic field in adjacent lines (figure 2-26). Thus it is necessary to check the signal due to the thermal effect by considering whether there is any change in temperature or other related things.

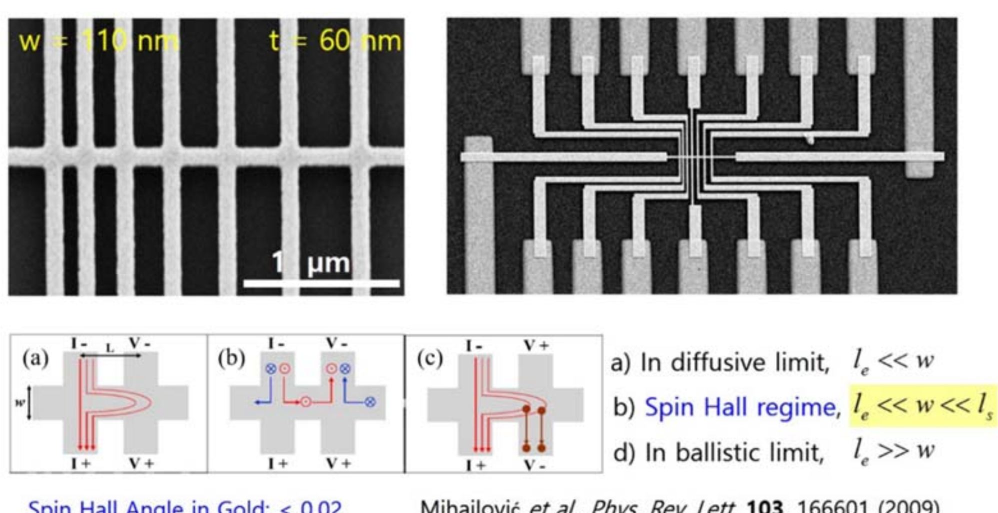

Figure 2-23. SEM image of H-bar geometry spin Hall device[55] (up) and schematic current flow of (a) diffusive (b) spin Hall and (c) quasi-ballistic region (reproduced by reference 55).

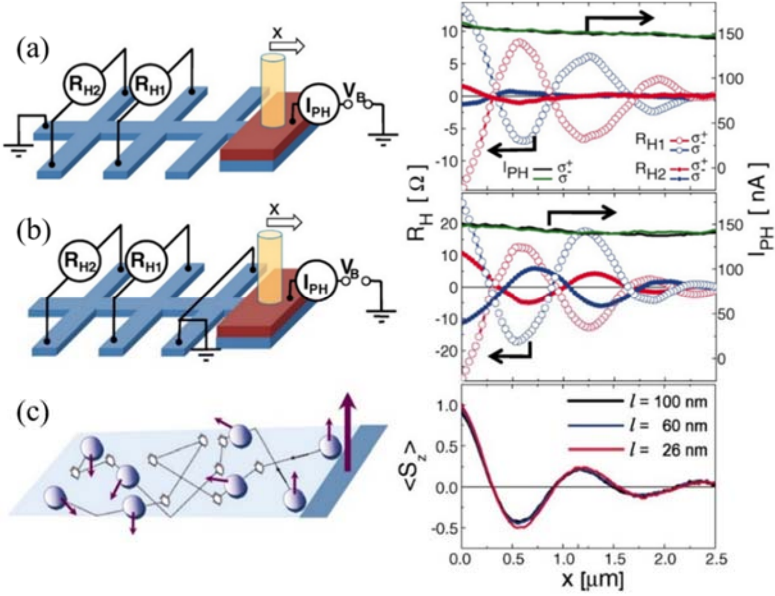

Figure 2-24. Spin Hall effect transistor[57]. (a) Schematics of the measurement setup with optically injected spin-polarized electrical current propagating through the Hall bar and corresponding experimental Hall effect signals at crosses H1 and H2. (b) Same as (a) for measurement geometry in which electrical current is closed before the first detecting Hall cross H1. (c) Schematics of the diffusive transport of injected spin-polarized electrons and Monte-Carlo simulations of the out-of-plane component of the spin of injected electrons averaged over the 1-mm bar cross section assuming Rashba field α = 5.5 meV Å, Dresselhaus field β = −24 meV Å, and different values of the mean free path l (reproduced from reference 57).

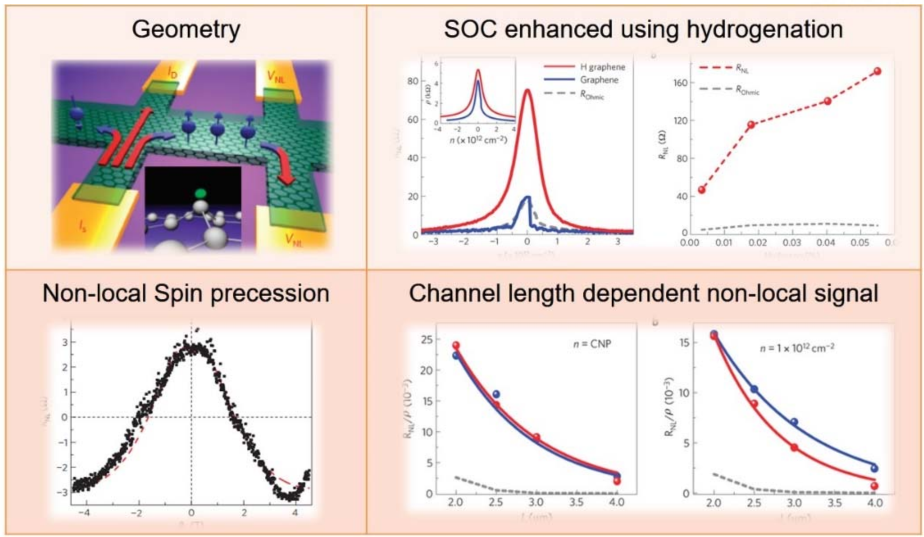

Figure 2-25. Spin Hall effect using non-local geometry in graphene[58]. They obtain SOC induced non-local voltage difference and further spin precession signal via parallel magnetic field by using 2D graphene channel material (reproduced from reference 58).

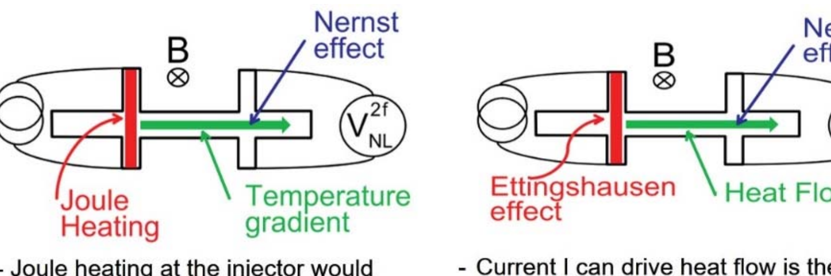

Figure 2-26. Possible thermal effect during non-local SHE measurement. With/without perpendicular magnetic field, the possible thermal effect such as Seebeck, Peltier, Nernst and Ettingshaugen effect can be present.

Chapter 3.
LAO/STO 2-Dimensional Electron Gas (2DEG)

3.1 Introduction of LAO, STO, and 2DEG

This chapter is for the introduction to the LAO/STO and 2DEG of the interface studied in this thesis. Each of LAO and STO single crystals are a conventional 3-elecment alloy ABO_3 (chemical formula) structure consisting of a combination of two different element cations and three oxygen atoms. In the material classification, it corresponds to an oxide semiconductor or a ceramic material. Each insulator material, LAO and STO single crystal, has the characteristics shown in Table 3-1 below. LAO is a distorted perovskite structure with a lattice constant a = 5.36 Å and a high bandgap insulator of 5.6 eV. The STO is characterized by cubic structure at room temperature and tetragonal structure at low temperature below 105 ° C, and its dielectric constant changes with temperature or external magnetic field. Also, it has a large band gap of 3.25 eV, and there is switching of dielectric and ferroelectric phase near 45 K. The STO has a lattice constant of 3.905 Å and is stacked with SrO and TiO_2 in the 001 direction. . In the STO, the 3d levels are split by the crystal field into e_g and t_{2g} states because the Ti atoms is surrounded by an oxygen octahedron[60]. And this STO can be electron doped by La substitution on Sr site, Nb substitutions on the Ti site, or by creating oxygen vacancies[60]. The mobility of STO films through doping or other method has been reported up to 50,000 cm^2/Vs at low temperatures[61]. STO is relatively easy to control its property by surface control, structural control, doping and deposition other upper materials, so characterization and application studies of STO have been conducted in various fields[62-67].

When such single crystal LAO and STO are stacked in an epitaxial relationship, a conductive layer of 2-dimensional electron gas (2DEG) is generated at the interface. The formation of conductive layer at the LAO/STO interface was first confirmed by Herold Hwang group in 2004[68]. Herold Hwang group obtained TiO_2-terminated single-crystal STO surface using an acid solution dip etching and oxygen-annealing process. Monocrystalline LAO was then epitaxially grown up to ~ 26 nm by the Pulsed Laser Deposition (PLD) method. The 2DEG (produced at the partial pressure of oxygen) showed mobility of up to 10000 cm^2/Vs at low temperature. This conductive layer can be formed from a few nm to tens nm depending on growth conditions (mainly LAO deposition on a STO substrate). And this conductive interface is often called a quasi-2DEG because it is not a perfect 2D system with a thickness of 1 nm or less. The essential conditions for making the conductive interface are i) LAO thickness of at least 4 unit

cell in the absence of external electric field, ii) LAO/STO single crystal epitaxial relation to the (001) direction, iii) TiO_2-termination of the STO surface (LaO termination of the LAO surface). However, in recent years, even if these conditions are not fully met, results of successfully formed 2DEG have been reported.

Property	$LaAlO_3$ (LAO)	$SrTiO_3$ (STO)
Single Crystal		
Stucture (crystallographic)	Distorted Perovskite (Rhombohedral a=5.36 Å)	Cubic a=3.91 Å (tetragonal below 105 °C)
Twinning structure	Orthogonal twin planes along (100)	Twin free
Melting point, hardness	2080 °C, 5.9 (Mohs)	2080 °C, 6-6.5 (Mohs)
Dielectric constant	25	300 (variable by Temp. and field)
Special character	Band insulator with large optical band around 5.6 eV	Indirect band gap of 3.25 eV Paraelectric > 45°K Ferroelectric < 45°K Specific resistivity > 10^7 Ohm/cm

Table 3-1. Property of each LAO and STO single crystal.

The origin of 2DEG formation at the LAO/STO interface is still under discussion. First, there is a polar catastrophe mechanism. As shown in figure 3-1, the LAO (4 unit cell or more) with the polarity of (001) direction is deposited on the STO, as a result, 1/2 electron per unit cell moves to the interface to resolve diverging potential[68, 69]. For TiO_2 terminated STO, this leads to an excess of ~10^{14} /cm^2 electrons at the interface. The interface of TiO_2/LaO can be conducting because the electrons from the LAO can be added to Ti^{4+} (Ti 3d orbitals) in STO and make it Ti^{3+}. Half of electrons will occupy the d-shell of Ti, then making the mixture of Ti^{3+} and Ti^{4+}. In the case of SrO termination, SrO/AlO_2 interface is formed. In this case, half of hole per unit cell will be transferred to the interface and energy costs for removing an electron from the O-2p valence band are too high to make this more favorable than a structural reconstruction[69, 70].This scenario can explains why the formation of conductive interface requires more than a critical thickness of LAO and STO to be TiO_2 terminated.

Another mechanism is that the conductivity comes from free electrons by oxygen vacancies in STO or LAO surfaces. STO is well-known material to be easily doped by oxygen vacancies during PLD deposition process due to low deposit pressure and diffusion of atoms to the STO surface with a high energy. And plasma during PLD consists of fractions of LAO such as La, LaO, Al, AlO etc. These fractions are not fully oxidized when they hit the substrate and have a higher affinity to oxygen then STO, thus they can extract oxygen from the substrate. When an oxygen ion is missing from the lattice, it introduces 2 electrons per vacancy because the valence of oxygen ions is O^{2-}. Carrier density will be enhanced by the oxygen vacancies and they will act as scatter centers at the interface[69]. This oxygen vacancy mechanism is associated with electron reconstruction of polar catastrophe scenario. And intermixing of La or Al in STO and Sr or Ti in LAO could also lead to a conducting layer. But the Transmission Electron Microscopy studies shows little intermixing and structural distortion. So the intermixing and structural distortion mechanism can be ignored. These days, researchers are accepting the coexistence of polar catastrophe and oxygen vacancy mechanism can be reasonable to explain the conductivity of the LAO/STO heterointerface.

One of the interesting phenomena at the interface is the co-existence of superconductivity and ferromagnetism at low temperature[71-73]. Usually the two mechanisms are counteract each other, the possible explanation is that the magnetism and superconductivity are carried by different orbital electrons. Carriers originate from the d electronic shell of the titanium (Ti) ions and come in two species, light d_{xy} and heavier d_{xz} and d_{yz} electrons. The d_{xy} electrons occupy lowest energy states and confined at the interface (figure 3-2). And the d_{yz} or d_{xz} electrons are extend further away from the interface and their mobility reaches much higher values than that of the d_{xy} states. Still it is not clearly understand, but can tell the electrons at d_{xy} orbital acts as both conducting electrons and ferromagnetism with coupling d_{yz} or d_{xz} orbitals (Hunds rule)[74-78].

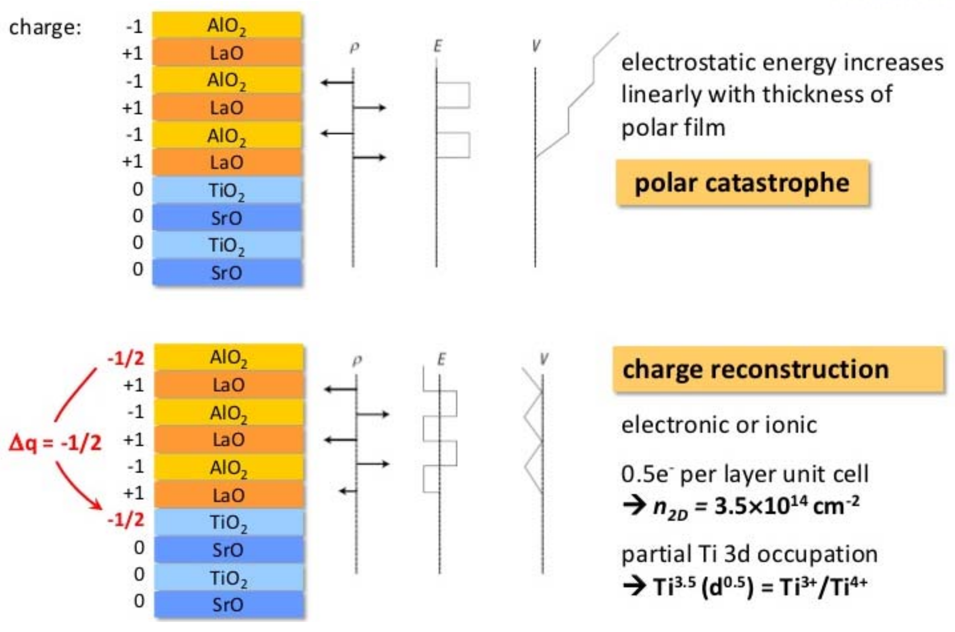

Figure 3-1. Polar catastrophe and charge reconstruction mechanism of LAO/STO interface conductivity[70].

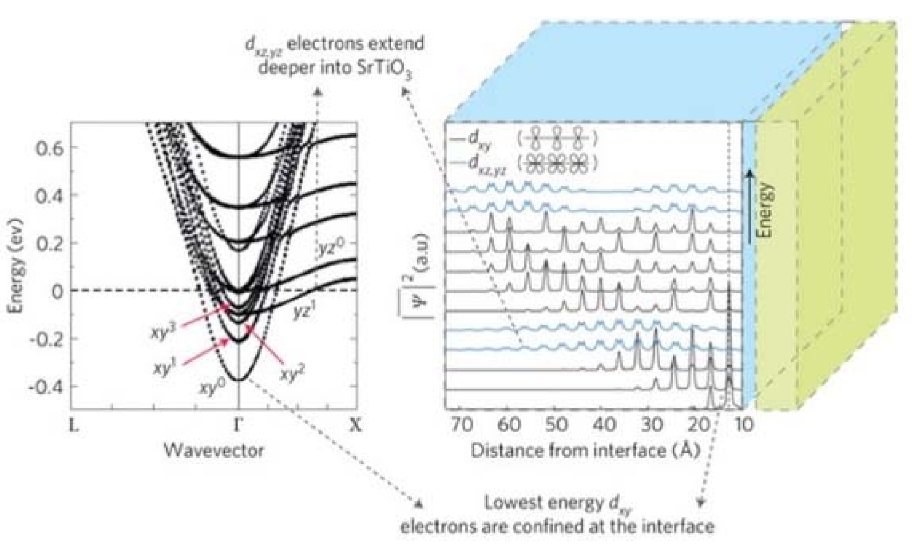

Figure 3-2. Electronic structure of LAO/STO interface[78]. Left, The dispersion of the different sub-bands. The lowest energy sub-bands have a d_{xy} character. Right, Extension of the wave functions of the sub-bands through $SrTiO_3$. The lowest energy d_{xy} electrons are very spatially localized at the interface, whereas d_{xz} and d_{yz} extend further into the $SrTiO_3$ (reproduced from reference 78).

3.2 LAO/STO research trend

A 2-dimensional (2D) material or a 2-dimensional electron gas (2DEG) at the oxide interface are fascinating materials for the research fields of implementing a next-generation device or a spintronic devices. Particularly, in recent years, the research field of spin-orbitronics (the fusion of spin orbit interaction and spintronics) or spin device with the spin-orbital interaction has growing attention to the 2D material or 2DEG at oxide interfaces (figure 2-1, 3-3). Conductive interface between insulating oxides exhibits high electron mobility[68, 79], tunable carrier densities and unique behaviors such as coexistence of superconductivity and ferromagnetism[71-73], Kondo resistance [80], etc. In this oxide interfaces, interesting and potential strategy is to study spin transport behavior for the future spintronic device applications[29, 81, 82]. Itinerant electrons at the oxide hetero-interface are predicted to have long spin diffusion length (up to several um)[81], while they are under the relatively strong Rashba-type spin orbit coupling (due to inversion symmetry breaking) [83-85].

LAO/STO is a typical 2DEG at the oxide interface. This research in LAO / STO can be categorized into three major areas. Study of basic physical properties (figure 3-4), study of electrical characteristics improvement (figure 3-5), and device application using LAO/STO 2DEG (figure 3-6, 3-7, 3-8). A study on the basic properties of LAO/STO 2DEG and its mechanism includes a study on unique properties such as Rashba interaction due to structure inversion symmetry breaking of LAO/STO. In 2007, the Kondo effect, which is the phenomenon that the resistance rises again below a certain temperature, was reported together with the low-temperature superconducting phenomenon (at the LAO/STO interface, LAO deposited under specific conditions)[80, 86]. The magnetic properties at the interface[87] and the coexistence of ferromagnetism and superconductivity[71-73] were reported. Also, it has been reported that the thickness of 2DEG can be controlled through heat treatment in oxygen atmosphere after deposition of LAO[88], and the charge concentration and conductivity of the interface can be controlled by an external electric field (gate voltage) [89, 90]. In addition, research and discussion on origin of 2DEG, magnetism and superconductivity at LAO/STO interface have been actively conducted so far[74-78, 91, 92].

In 2008, Mannhart & Triscone group developed an LAO/STO Hall bar structure device, and obtained an electronic phase diagram representing the low-temperature 2D superconducting region by measuring the resistance change (field effect modulation) according to the gate voltage (external electric field) in the mili- kelvin temperature region[93]. The SdH oscillation can also be obtained if the mobility of LAO/STO (over 5000 cm^2/vs) and the charge concentration condition are met. Controlling the growth conditions of LAO/STO can yield significantly higher mobility and charge concentration at low temperature. This oscillation is periodic for 1 / B (external magnetic field perpendicular to the sample). Other groups have also reported the SdH oscillation result according to the gate voltage[94, 95]. The beating of SdH oscillation measurement results indicate the presence of Rashba SOC due to structural inversion

symmetry breaking at the LAO/STO interface. In addition to the SdH oscillation measurement, Rashba SOC of the LAO/STO 2DEG can be obtained by measuring the MR with an external perpendicular magnetic field. The experiment showing that the Rashba constant can be obtained by using the MR and its change according to the gate was reported in 2010[83]. Rashiba SOC constants can also be obtained through planar anisotropic magnetoresistance (Planer AMR) measurements[96]. Interesting phenomena (such as Kondo effect, superconductivity, coexistence of superconductivity and ferromagnetism) of LAO/STO interface and their experimental results (existence of Rashba interface, superconducting region from electronic phase diagram and SdH oscillation) were presented in figure 3-4.

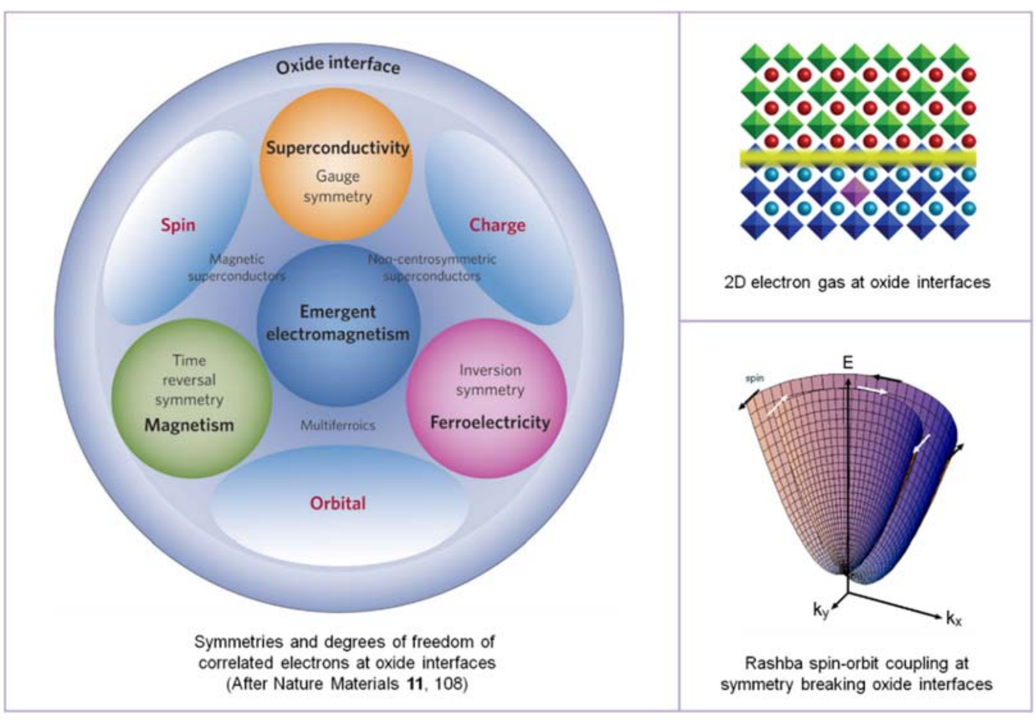

Figure 3-3. Emergent phenomena and 2D electron gas with Rashba SOC at oxide interface (reproduced from reference 114).

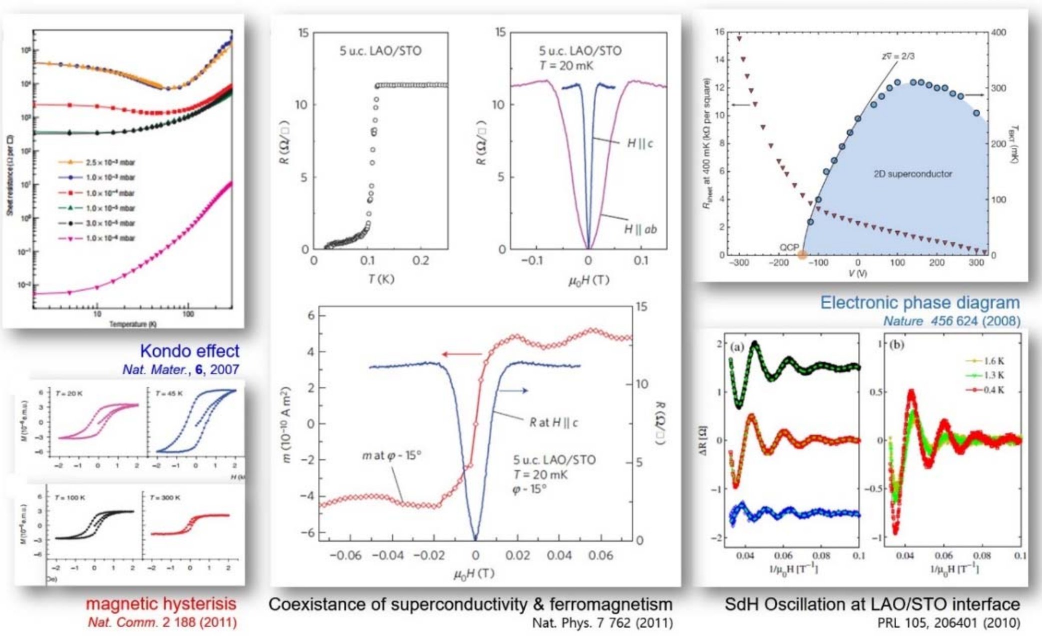

Figure 3-4. Interesting phenomena of LAO/STO interface.

LAO (or LAO/STO) growth condition and deposition condition control[68, 79, 80, 86, 97],, applying external voltage or ion implantation / doping[98, 99], interlayer insertion[100], and additional top materials[101, 102] are used to improve conductivity and charge density of the conductive interface. In addition, LAO/STO 2DEG conductivity changes can also be observed by UV irradiation, top and back gate voltage, and heating[103]. Polarity characteristics of LAO, which is susceptible to external influences, and ease of surface control of STO are thought to affect 2DEG. Device application studies of LAO/STO 2DEG have also been tried in various ways. In 2013, Christopher bell group reported the field effect transistor application using LAO as oxide barrier layer between top gate material and 2DEG (figure 3-6)[104]. Conductance change by external light and solar cell operation using residual polar field (figure 3-7) [105], and gas sensor operation through surface nanoparticle application(figure 3-8)[106] have been reported. In addition, including thermoelectric properties[107], a paper on the development of fabrication process of LAO/STO suitable for nano-electronic device application is also reported. Table 2 below compares the properties of LAO/STO and other solid-state materials. The LAO/STO has a long mean free path of electrons, and can realize devices with few nanometers using AFM, and has room temperature magnetism and has strong SOC. This is considered to be desired properties to apply for nano-electronic devices, particularly for nano-spin electronic devices.

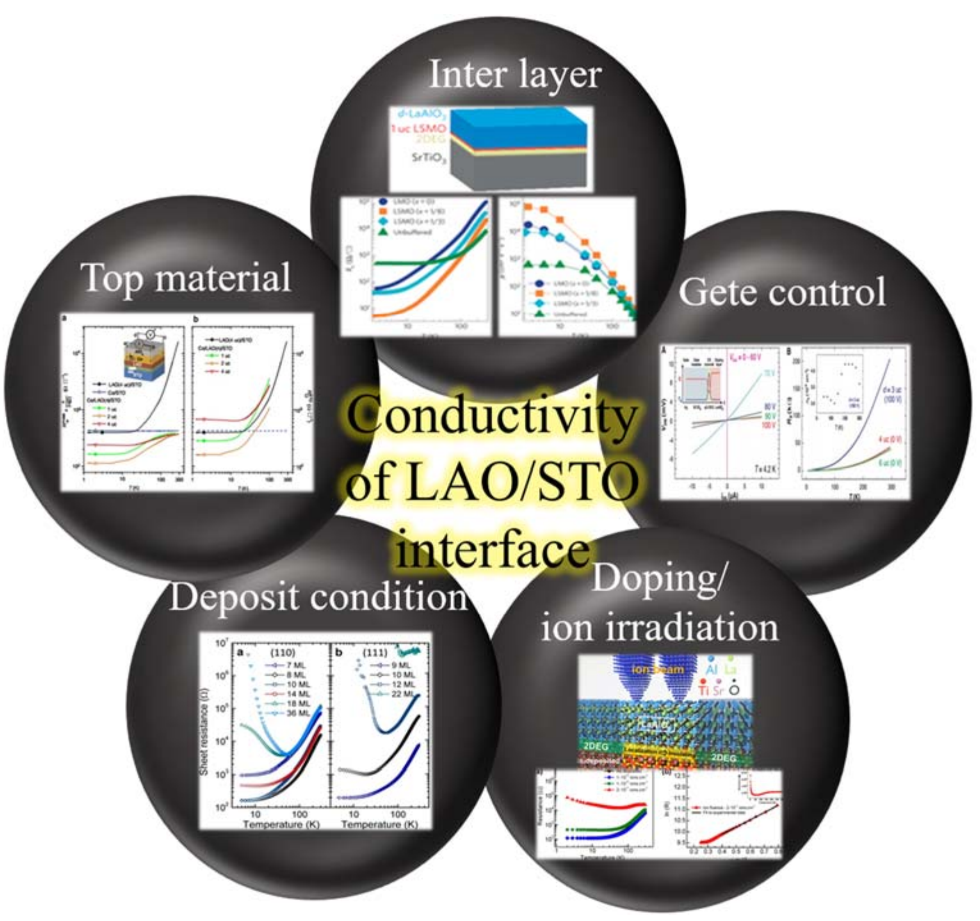

Figure 3-5. Controllable conductivity of LAO/STO interface via several kinds of method.

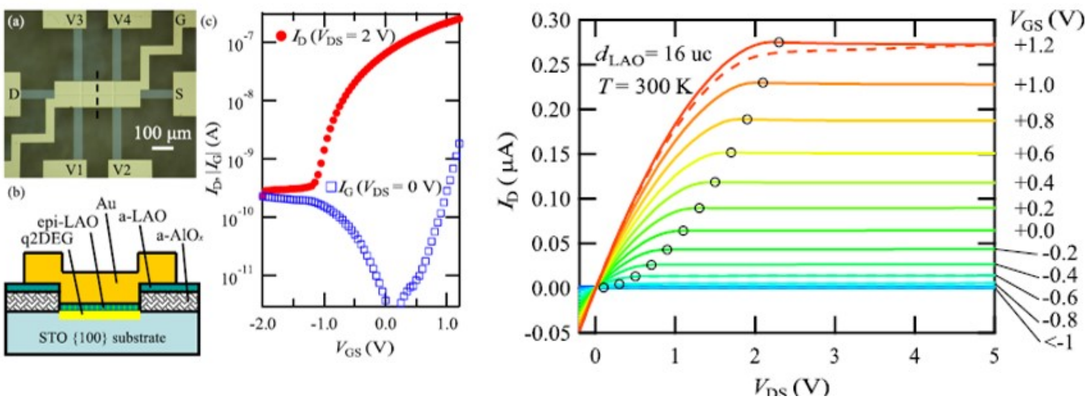

Figure 3-6. Transistor operation in top gated LAO/STO heterostructures[104] (reproduced from reference 104).

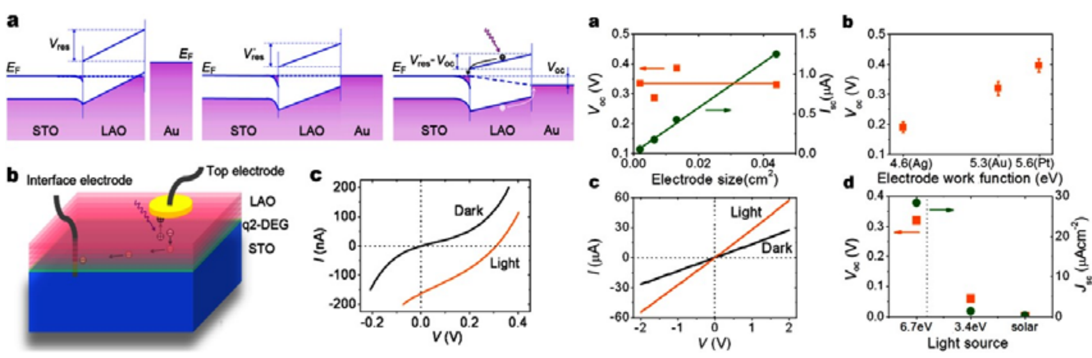

Figure 3-7. Giant photovoltaic effects[105] driven by residual polar field (reproduced from reference 105).

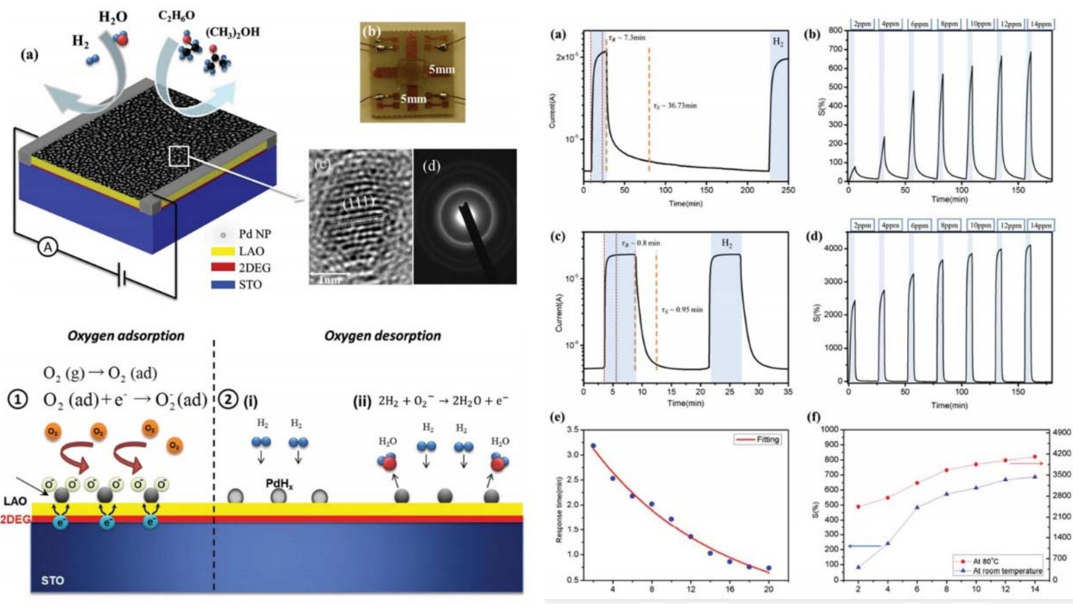

Figure 3-8. Highly sensitive gas sensor[106] by the modulation with Pd nanoparticles (reproduced from reference 106).

	$LaAlO_3/SrTiO_3$	III–V semiconductor heterostructures	Graphene	Nanotubes	Semiconducting nanowires
Dimensionality	2D/1D	2D/1D	2D	1D	1D
Record mobility $[cm^2/(V \cdot s)]$	6,600 (82)[a]	36,000,000 (162, 163)	200,000 (164–166)	$>$100,000 (167)	20,000 (168)
Mean free path	Hundreds of nanometers	~100 μm	~1 μm (165)	On substrate: ~10 μm (169); suspended: not yet measured	~100 nm (170)
Typical densities	10^{12}–10^{14} cm^{-2}	10^{10}–10^{12} cm^{-2}	10^9–5×10^{12} cm^{-2}	10^3–10^8 cm^{-1}	10^5–10^8 cm^{-1}
Achievable lithographic feature size	A few nanometers with AFM lithography	~100 nm [limited by interface depth (171)]	A few nanometers (but with substantially increasing disorder)	Tens of nanometers [disorder-free in suspended devices (172)]	A few nanometers (grown heterointerfaces along wires)
Superconductivity	Yes; T_c^{max} ~ 300 mK; gate tunable	No	No (only by proximity)	No (only by proximity)	No (only by proximity)
Magnetism	Yes; T_c > 300 K (22, 35); gate tunable	Yes; T_c < 200 K (173)	No	No	Yes; T_c < 20 K
Ferroelectricity	Possibly	No	No	No	No
Strong lattice-electron coupling	Yes	No	No	Yes	No
Spin-orbit coupling	Yes; a few meV; gate tunable	Yes; ~1 meV; gate tunable; Rashba and Dresselhaus	No; a few μeV; predicted	Yes (174–176); a few meV; circumferential motion coupled to spin	Yes; ~200 μeV; primarily Rashba

[a]A mobility of $>$100,000 $cm^2/(V \cdot s)$ has been reported in γ-alumina/$SrTiO_3$ (47).

Table 3-2. Comparison between LAO/STO and other solid-state materials systems for nanoscale devices[108]. Although LAO/STO is currently more electronically disordered than the other materials systems, its broad array of physical properties and potential tunability make it very attractive as a system for studying correlated electron physics in engineered environments (reproduced from reference 108)

3.3 Spin transport in LAO/STO (1st spin injection and detection through LAO/STO)

Recently, N. Reyren et al. reported direct spin injection & detection at LAO/STO interface by using FM material as spin injector and LAO as a tunnel barrier with 3-terminal geometry[81]. This is the first spintronic application of LAO/STO interface. As shown in figure 3-9, they used Co ferromangnetic material as spin injection source. 100 μm x 300 μm dimension of Co electrode was shared as source current electrode and detection voltage electrode in 3 terminal geometry. And it's right and left sides, each of 2DEG connecting electrodes were used as injecting current and detecting voltage electrode. Then the Hanle curve was observed by applying an external magnetic field, which leads a drop of resistance vs magnetic field with a typical Lorentzian shape as shown figure 3-9 below (already introduced at chapter 1.3). Hanle and inverted Hanle curves are generally measured to prove (show) the spin-dependent signal. Spin precessional dephasing of spin population (Hanle effect) is direct method to confirm spin injection and detection using ferromagnetic materials [81, 109] or spin-orbit coupling induced non-local signal with no magnetic materials[58]. But they used 3-terminal geometry which has controversy and question of relying on real spin transport[82], so that is one of my experimental motivation to measure real spin transport. Spin relaxation time $\tau \approx 50$ ps was extracted from the width of Lorentzian shape curve with g-factor 2. And the spin diffusion length $l_s \approx 1$ μm ($l_s = \sqrt{D\tau}$) was obtained from diffusion constant D and spin life time τ with RA product ($\approx 200\ \Omega.\mu m^2$). And they suggested the existence of electronic localized state (ELS) in the LAO band insulator which strongly affect the escape time of the electrons from the localized states to the 2DEG. So the spin conservation on the ELS will create a finite spin accumulation in the channel due to the tunnel coupling (spin life time is much longer that the escape time). Further, they reported injected spin signal can be controlled by applying back gate voltage (figure 3-10). V_g is not expected to influence the spin lifetime on the localized states. The maxima of the spin signal ΔRA shifts with the gate voltage indicating a shift of the Fermi level in the 2DEG due to a change of the confinement potential of the well in STO at LAO/STO interfaces (figure 3-10 (c)).

Other reported spin manipulation through LAO/STO interface is using interface-driven SOC mechanism which we call Rashba-Edelstein effect (REE) and inverse Rashba-Edelstein effect (IREE) (see above chapter 2.1). At 2016, E. Lesne et al observe very large, gate tunable inverse Rashba Edelstein effect (IREE) in NiFe/LAO/STO heterostructures with higher spin to charge conversion efficiency than other spin Hall materials[110]. They injected spin current from a NiFe ferromagnetic material into the oxide 2DEG through spin pumping method and detect the resulting charge current through the interface (figure 3-11). The spin to charge conversion from the ferromagnetic material can

be strongly modulated by a back gate voltage.

These experimental reports used ferromagnetic material to inject spin current. One of the important motivation of my experiment is to manipulate spin without ferromagnetic material through the LAO/STO interface.

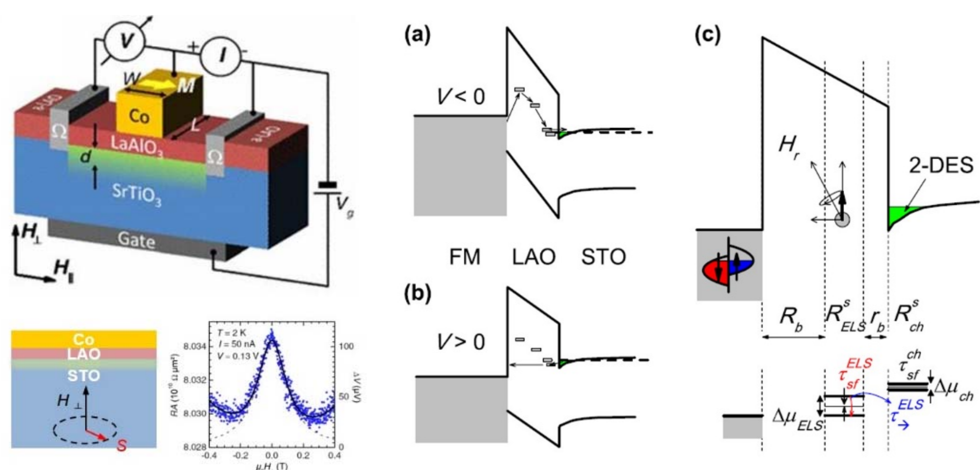

Figure 3-9. First experimental spin injection and detection at LAO/STO interface[81] (left) and suggested spin injection mechanism from FM materials to 2DEG through LAO oxide insulator (right) (reproduced from reference 81).

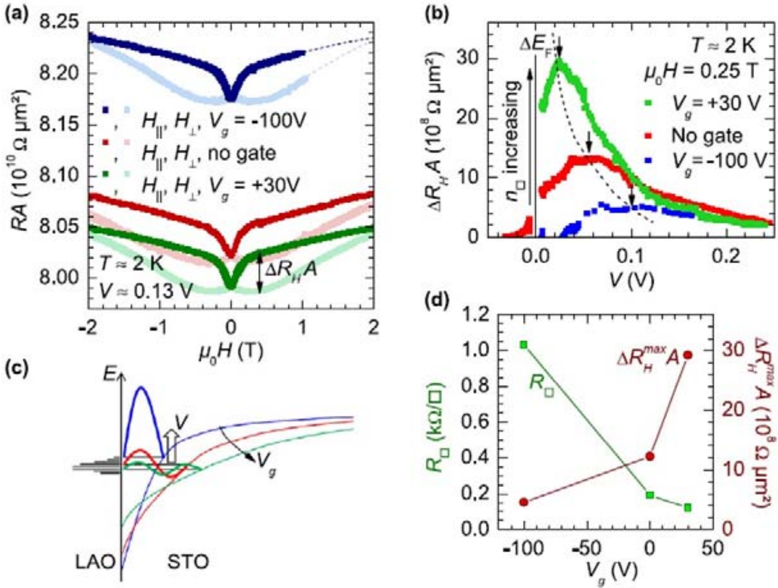

Figure 3-10. Gate tunable spin precession signal with RA product change (reproduced from reference 81).

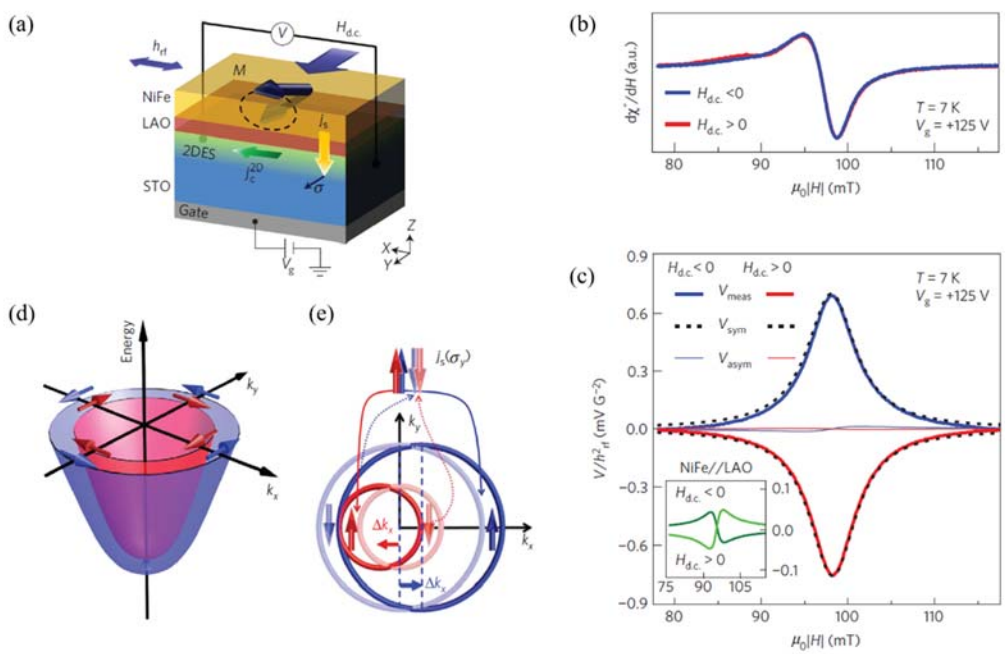

Figure 3-11. Spin to charge conversion in NiFe/LAO/STO device[110]. (a) Schematic of spin-pumping experimental configuration. (b) Ferromagnetic resonance signal at negative and positive external magnetic fields, at a gate voltage of V_g = +125V. (c) Detected voltage normalized to the square of the amplitude of the RF field (thick solid lines) at negative and positive external magnetic fields at V_g = +125V. (d) Sketch of a electron dispersion in Rashba-type system at equilibrium. At the Fermi level there are two Fermi contours (one sketched in blue, the other in red) with opposite spin textures (the blue and red arrows show the spin direction of the electrons on the outer and inner contour, respectively). (e) Principle of the inverse Edelstein effect: the injection of a current j_s of spins oriented along y from the ferromagnet creates an accumulation of spin-up electrons (darker blue and red arrows) and a depletion of spin-down electrons (lighter blue and red arrows). This accumulation/depletion process shifts the two inequivalent Fermi contours, which generates a transverse charge current along x (reproduced from reference 110).

3.4 Localization
(Related issue for spin transport at LAO/STO 2DEG)

One of the important phenomena associated with SOC is the localization phenomenon. Localization phenomena can be divided into strong localization phenomenon, weak localization phenomenon, and weak anti-localization phenomenon[111, 112].

The strong localization (SL) phenomenon proposed in 1958 by P.W. Anderson, so it is also called Anderson localization. Anderson proposed localization of electrons by impurities or defects in superconductors with large enough entropy. This localization is because the electrons accumulate only in a certain region due to a lot of impurities in the metal. In other words, it is a phenomenon that the wave function of electrons in a disordered medium is localized without spreading. This phenomenon is distinct from weak localization (precursor effect of strong localization) and Mott localization. Mott localization is a phenomenon that occurs in the transition between metal and insulator, not due to disorder, but by strong mutual Coulomb repulsion electrons[112, 113].

Dominant phenomenon in conductive metals or 2DEGs are weak localization (WL) phenomena and weak anti-localization (WAL) phenomena. WL phenomena and WAL phenomena are illustrated in figure 3.12. A WL phenomenon is coherent scattering that occurs at low temperatures in a disordered electronic system in a metal or semiconductor. The WL shows a graph in which the resistance decreases with increasing perpendicular magnetic field. On the contrary, the WAL phenomenon is incoherent scattering phenomenon and appears when there are strong SOC is exist. So the WAL shows a graph in which the resistance increases with increasing perpendicular magnetic field. If WL and WAL coexist in the material, the resistivity increases with increasing vertical magnetic field, then decreases at particular magnetic field strength shown in figure 3-12 (right).

These localization phenomenon occurs depending on the relative length scale between the electron mean free path, the diffusion length, and the phase coherent length. The mean free path is generally much smaller than the phase coherent length. If the spin diffusion length is significantly larger than the other two lengths, then WL occurs. And if the spin diffusion length is in between other two value and is close to the mean free path, then WAL occurs. Lastly, if the spin orbit path is close to the phase coherent length, then coexistence of WL/WAL occurs (figure 3-14 left below). In 2010, J. M. Triscone group measured vertical magnetic field versus resistance (MR) graphs with back gate voltage and analyzed the relationship between WL / WAL change and Rashba SOC at the LAO/STO interface according to the gate voltage (figure 3-13). And further, at 2012 and 2014, electronic phase diagram which represent the relation between WL/WAL and Rashba field depends on back/side gate voltage with Rashba field at LAO/STO interface was obtained (figure 3-14) [114, 115].

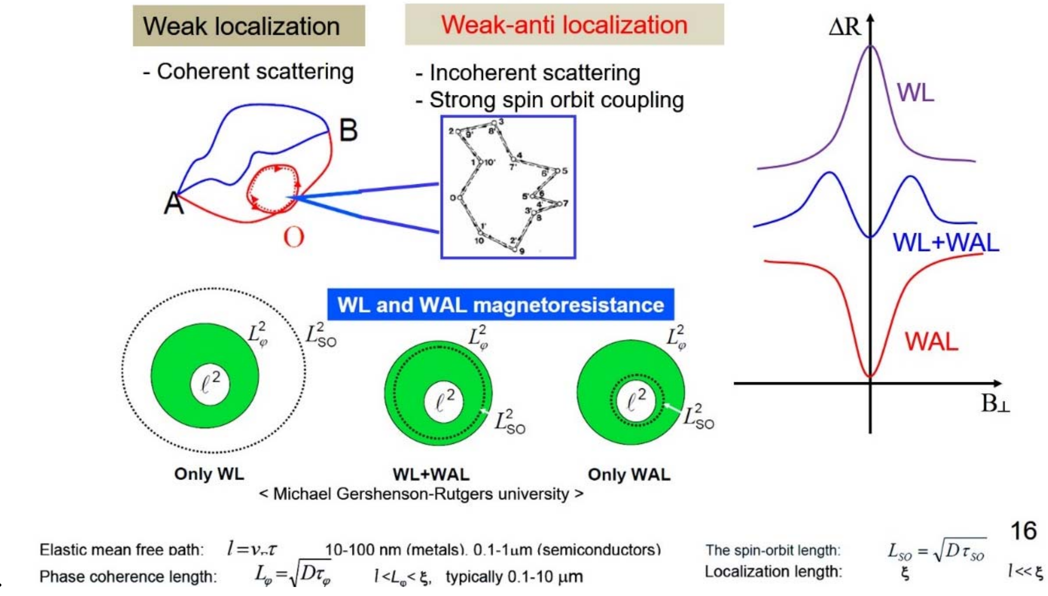

Figure 3-12. Weak/weak anti-localization depends on the relative length between electric mean free path (l), spin orbit length (L_{so}) and phase coherence length (L_{φ})

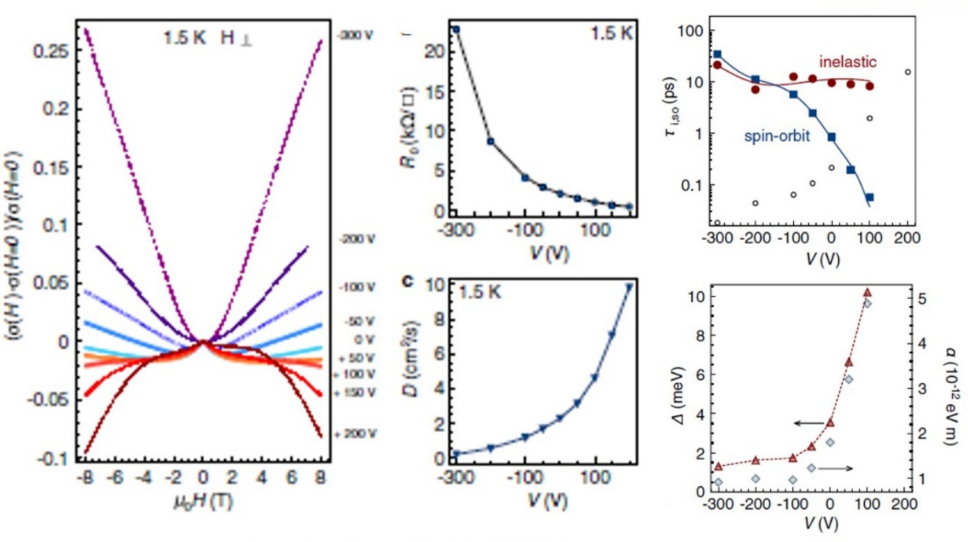

Figure 3-13. Experimental observation of weak/weak anti-localization and Rashba SOC at LAO/STO interface[83]. Depends on back gate voltage, weak/weak anti-localization is changed. Rashba SOC constant was obtained by fitting the MR curve (reproduced from reference 83).

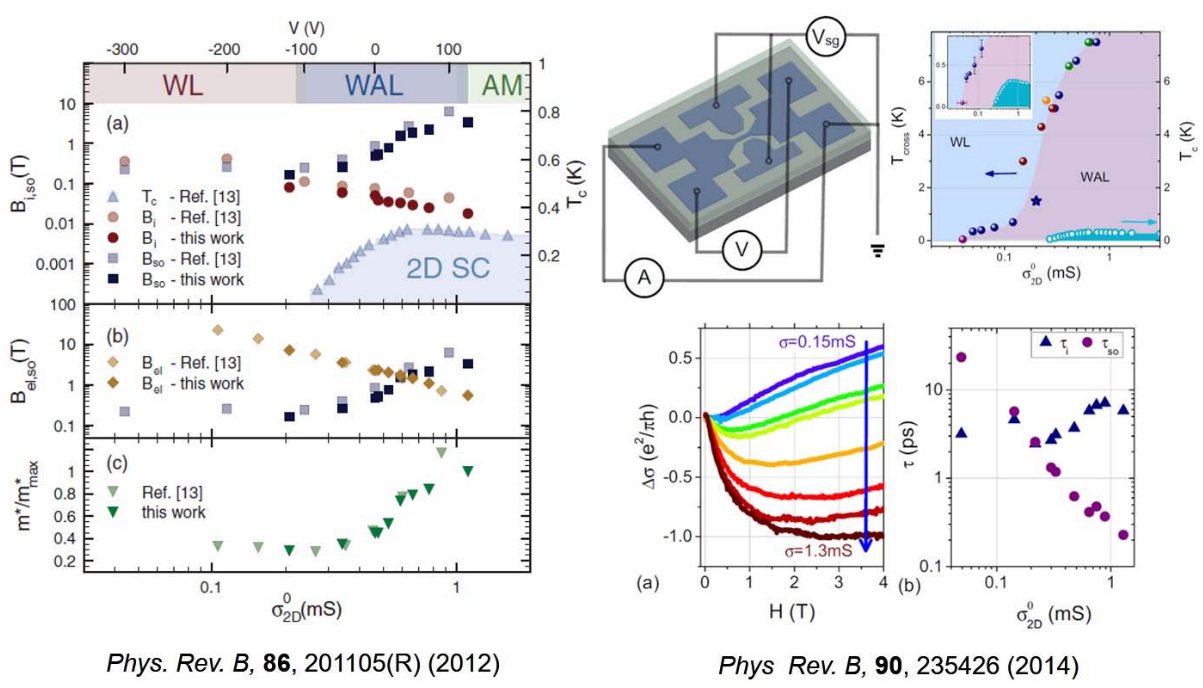

Figure 3-14. Electronic phase diagram which represent gate dependent WL/WAL and Rashba field at LAO/STO interface (reproduced from reference 114, 115)

Chapter 4.

Experimental Technique (Sample Fabrication)

4.1 LAO/STO sample preparation

As mentioned previous chapter, the main purpose of this thesis is to measure SHE/ISHE induced non-local spin diffusion signal through the LAO/STO interface and determine the spin diffusion in LAO/STO via spin precession signal with external magnetic field. To realize SHE/ISHE device without FM materials, three requirements need to be fulfilled. Firstly, the LAO/STO with 2DEG need to be structured in a Hall bar like geometry (H-bar). Second, the 2DEG contact electrode should be stable even at low temperature over repeated measurement. Third, relatively stable 2DEG condition should maintain through room temperature to low temperature (2 K). This chapter describes the various experimental approaches that have been performed for the successful device fabrication.

STO substrate, TiO_2-termination

Single crystal of STO substrate with (001) orientation (less than 0.1˚ miss-orientation) used in our device fabrication has 0.5 mm thickness with one side polished from CrysTec (Kristalltechnologie). The standard specification of delivered STO substrate is below 0.5 nm average roughness, below 0.8 nm root-mean-square-roughness, and below 3.5 nm maximum peak-to-valley range in the surface area. $SrTiO_3$ (001) single crystal substrates were etched by using buffered HF solution, and then were annealed at 1000 °C under an oxygen atmosphere to create the TiO_2-terminated surface with the clean step-terrace structure shown in figure 4-1 (a). TiO_2-terminated $SrTiO_3$ substrate was used for $LaAlO_3$ growth.

LAO deposit

LAO/STO 2DEG were prepared by pulsed laser deposition (PLD) on a (001)-oriented and TiO_2-terminated STO substrates (5 mm x 5 mm). Epitaxial LAO films were deposited by using pulsed laser deposition (PLD) with a KrF excimer laser (λ = 248 nm) under 1 mtorr O_2 pressure. A KrF excimer laser beam was used on a LAO single crystal target with an energy density of 1.5 J/cm^2 and a frequency of 2 Hz.

Grown LAO has 5 ~ 10 unit cell thickness and have clear surface step terrace structure with following

STO surface (figure 4-1 (b)). Temperature dependence sheet resistance and low temperature mobility were first tested to confirm quasi-2DEG condition using Van Der Paww geometry. The samples used in our studies have several tens to thousands ohm of sheet resistance and 500 ~ 1200 $cm^2/V.s$ of mobility at low temperatures. (TiO_2-termination and LAO deposit process was performed by co-worker group at KIST.)

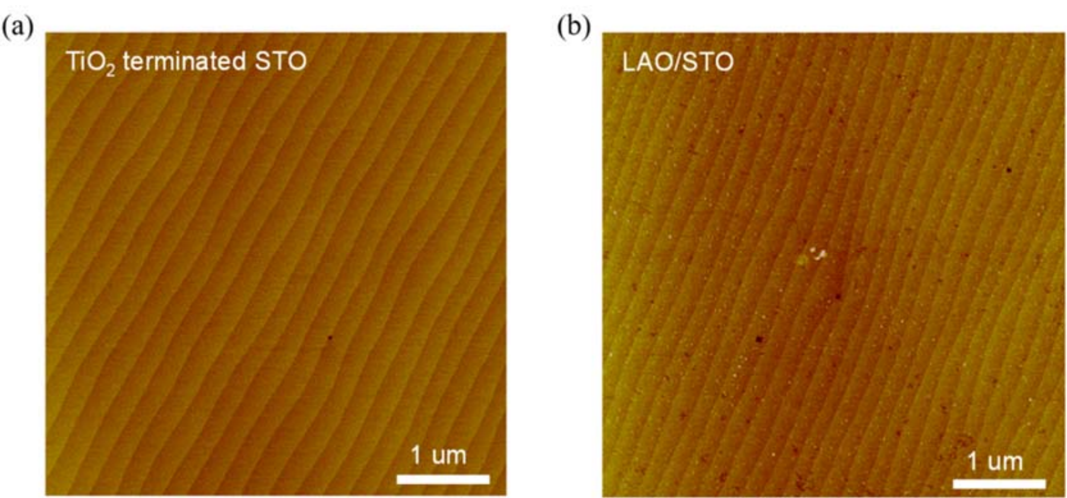

Figure 4-1. AFM images of the surface morphology (a) TiO_2-terminated STO substrate. (b) LAO/STO substrate.

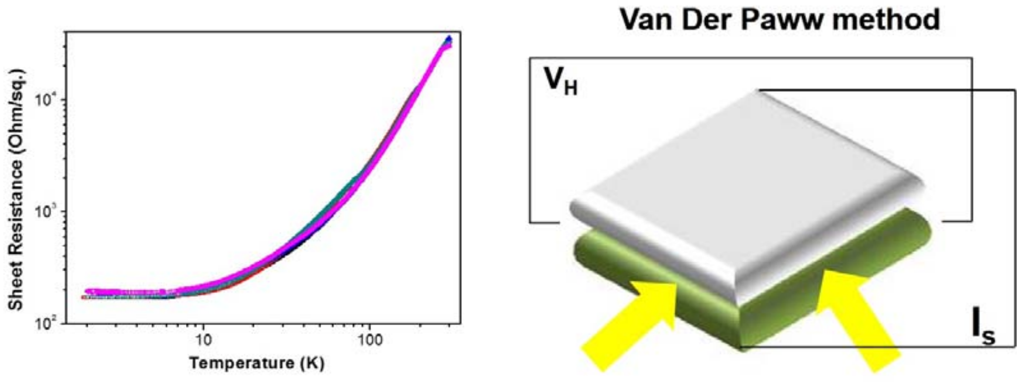

Figure 4-2. The prepared LAO/STO has metallic behavior of temperature dependent sheet resistance and mobility measured with Van Der Paww geometry. The estimated mobility and carrier concentration averaged for several samples were 1200 cm^2/Vs and 3.1 x 10^{13} cm^{-2}, respectively.

4.2. Patterning process & Fabrication

To make H-bar geometry of LAO/STO 2DEG, two types of device fabrication process was attempted.

Bottom-up process approach.

Figure 4-3 shows the schematic process of bottom-up fabrication for LAO/STO H-bar device. After TiO_2-termination of STO surface, lithography and buffer layer deposition process were followed. Then LAO can be deposited on the patterned STO surface. After then, 2DEG contact electrode was deposited on the surface of LAO/STO. In this bottom-up process, oxide insulating material should be chosen as a patterned buffer insulating layer. The buffer insulating layer need to be insulating with STO surface and should not make any other conductive interface 2DEG. It also should have good adhesion with STO surface for maintaining its structure condition during followed processes. Possible candidate for a patterned insulating layer were AlO_x (Al_2O_3), NiO_x, SiO_2. Among them, we choose AlO_x layer deposited by e-beam evaporator using Al_2O_3 source material for good adhesion to STO surface and stable condition over following fabrication processes. In this bottom-up process, 2DEG contact electrode need to be deposit at the end of the process. If the 2DEG adhesion is not stable, the temperature dependent resistance do not display the metallic behavior (quadratic decrease with temperature decrease) as you can see in figure 4-4.

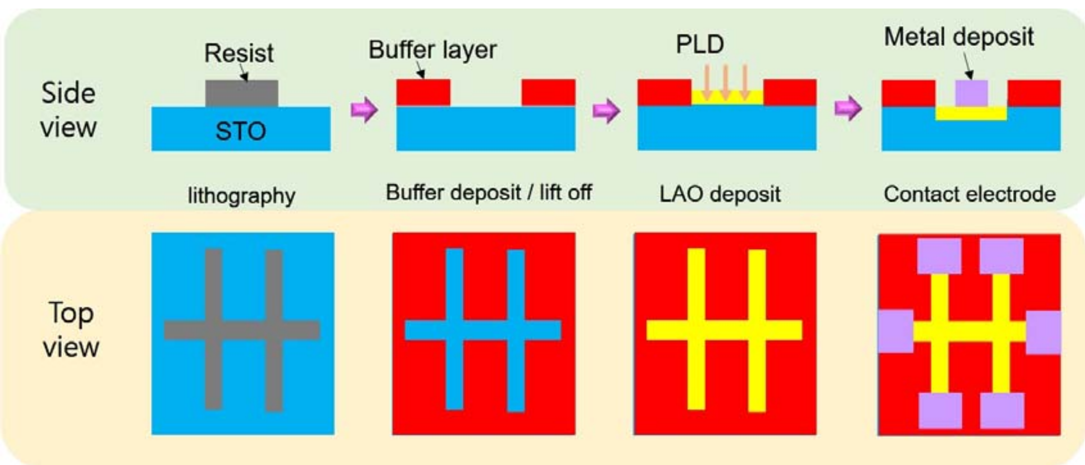

Figure 4-3. Schematic of bottom-up device fabrication steps for H-bar patterned LAO/STO 2DEG.

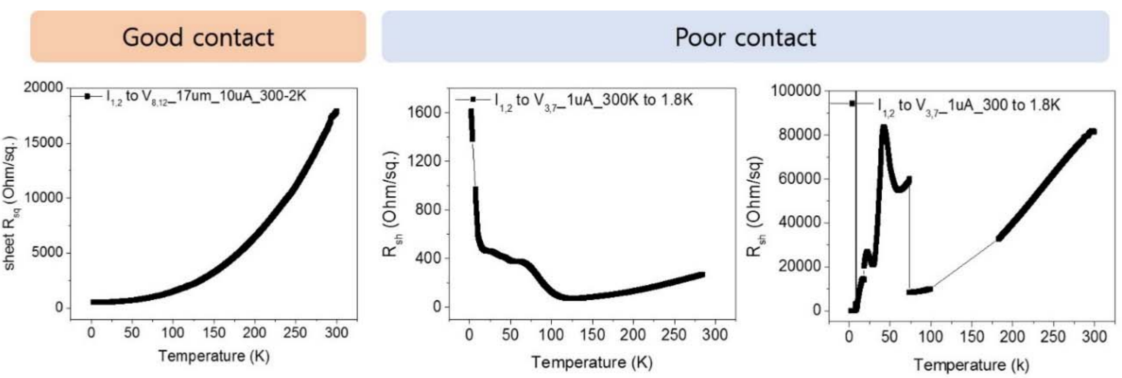

Figure 4-4. Example of resistance vs temperature for contact electrode with good adhesion condition (left) and contact electrode with poor adhesion condition (right).

Top-down process approach

Because the negative points of bottom-up process can not be solved easily, top-down process was used for H-bar type geometry of LAO/STO 2DEG in further study.

We fabricated simple Hall-bar (H-bar) like geometry to study non-local spin diffusion without ferromagnetic layer. Two times of e-beam lithography was used for the device fabrication.

First, LAO (~ 2.5 nm)/STO was cleaned with acetone, ethanol and DI water with sonication. Then it was coated with negative PMMA (~ 600 nm) and annealed 95˚C around 2 minutes. Then e-beam lithography was performed with 4.0 dose (C/m2) and 80kV of electron beam condition. After ~ 2 minute developing, sample was loaded on a vacuum chamber for thermal evaporation. 100 nm of Al buffer layer was thermally evaporated under 10^{-5} torr vacuum condition. After lift off, dot patterned sample was dry etched with reactive ion etching (RIE) using Ar plasma (ion). Then, circular Au (30 nm)/Ti (10 nm) contact electrode for LAO/STO interface was obtained by e-beam or thermal evaporation process.

Second, dot electrode patterned LAO/STO was cleaned with acetone, ethanol and DI water with sonication process. Then it was coated with positive PMMA (~ 150 nm) and annealed at 185˚C for around 2 minutes. Then e-beam lithography (4.0 dose (C/m2) and 80 kV of electron beam condition) was performed to make H-bar type geometry of device. After ~10 minute developing, sample was loaded on a vacuum chamber for thermal evaporation. 100 nm of Al buffer layer was thermally evaporated under 10^{-5} torr vacuum condition. After lift off, patterned (with variation of different channel

length) buffer layer sample was dry etched with RIE using Ar plasma (ion) and followed by oxygen plasma treatment. Then, oxygen annealing was performed at 200 ˚C ~ in order to anneal out oxygen vacancies created in the STO surface during etching. Patterned LAO/STO layer can be obtained in this process after removing Al buffer layer.

Finally, additional contact electrode (Au 30 nm/ Ti 10 nm) was evaporated on the top of the dot patterned contact electrode to make proper adhesion between metal and 2DEG.

We fabricated several tens of samples to confirm feasibility and reproducibility of LAO/STO spin Hall device. Each sample has four different channel length with variation of 2 ~ 10 μm to confirm spin diffusion through the conductive interface. And the H-bar device was patterned by reactive ion etching and oxygen annealing process to remove oxygen vacancy of STO surface. Detailed fabrication process was displayed in figure 4-5. And each of equipment condition was shown in figure 4-7, 4-8 and LAO/STO etching condition is shown in figure 4-9.

(a)
Markers
E-beam lithography
Metal deposit. / lift off
(i) 2DEG contact
E-beam lithography
Buffer metal deposit . / lift off
Ar reactive ion etchnig
Metal deposit. / lift off
(ii) H-bar patterning & contact electrode
E-beam lithography
Buffer metal deposit. / lift off
Ar reactive ion etchnig
Annealing / lift off
Metal deposit.

(b) (i) 2DEG contact
E-beam litho.
Metal deposit. / lift off
Reactive ion etching
Metal deposit. / lift off
(ii) H-bar patterning & contact electrode
E-beam litho. & Metal deposit. / lift off
Reactive ion etching & annealing / lift off
Contact electrode deposit.
STO
LAO
Au/Ti
Buffer layer
Resist

(c) (i) 2DEG contact
E-beam litho.
PMMA
Markers
Metal deposit. / lift off
(ii) H-bar patterning & contact electrode
E-beam litho.
Metal deposit.
Reactive ion etching & annealing / lift off
Reactive ion etching & annealing / lift off

Figure 4-5. Device fabrication procedure. (a) Device fabrication steps. (b) Schematics of the side views of the device at each fabrication step. (c) Optical images of the top views at each fabrication step.

STO surface etching & annealing process

At top down process approach, one of important step is etching and annealing process of STO surface. As presented in "*Top-down process approach*" part with figure 4-5, STO surface etching and annealing process was enacted for H-bar pattering of 2DEG (figure 4-5 ; '(ii) H-bar pattering and contact electrode' step).

There can be two types of etching method for patterning LAO/STO, one is wet etching method using acid solution and the other is dry etching method using focused ion beam (FIB), ion milling or RIE.

One of acid solution for wet etching of LAO/STO is buffered HF solution (BOE; buffered oxide etching). In the wet etching and patterning process, we need to choose proper barrier (buffer) material to endure etching by acid for μm scale H-bar pattering of LAO/STO. This wet etching process has some negative point for LAO/STO pattering. It is hard to control etching rate because of handling by person and surface uniformity is difficult to be reproducible producing sample to sample varication. And some impurity from acid solution can be deposit on the surface of STO. Furthermore, isotropic direction of wet etching can be a negative point for maintaining uniform and proper size of H-bar patterned LAO/STO 2DEG. Thus, it is hard to obtain reproducible micro scale patterning via wet etching process. Despite these problems, one group successfully obtained cross bar patterned LAO/STO interface for VDP geometry using buffered Hf solution[116]. They used surface oxidized photoresist buffer layer for 20 μm square VDP geometry and developed electrode pattering as shown at figure 4-6.

The dry etching process for LAO/STO pattering can be conducted by using FIB, ion milling or RIE method. FIB and ion milling use Ar source and they don't essentially need buffer layer for patterning. Both are normally utilized for pre-surface treatment (FIB) or cross-section cutting (ion milling) for transmission electron microscope (TEM) analysis. Thus, FIB has nanometer scale of etching area with low beam power and ion milling has micrometer scale of etching area with high power. Thus they are not suitable for large area (more than millimeter scale) patterning with relatively fast etching rate (more than nanometer per minute). On the other hand, RIE, which is large area etching process method, can obtain relatively fast etching rate (more than nanometer per minute) suitable for patterning around wafer scale area. For the patterning of 5 mm by 5mm area of LAO/STO sample, FIB or ion milling need more than ten hour, which is not suitable for reproducible patterning, but RIE takes ~ 10 min with reproducible pattern using buffer layer (lithography process). Figure 4-9 shows the STO etching condition (table) and AFM step image between LAO/STO and etched STO surface used in this thesis. The condition also explained at "*Top-down process approach*" part in the previous section. By using this etching condition, 20 ~ 25 nm of LAO/STO was etched to remove 2DEG clearly.

Furthermore, it is essential to perform oxygen annealing process after RIE in order to remove oxygen vacancy at the surface of STO. The etched STO surface by Ar plasma can have structural defect such as oxygen vacancy. Thus, conductive STO surface (several tens kilo ohm per centimeter) from the

plasma treatment cannot be avoided[117-119]. Oxygen atmosphere annealing process with temperature range of 200 ~ 800 °C can remove or anneal out the conducting surface[118, 119]. In this thesis experiment, we use 200 ~ 300 °C annealing temperature in oxygen atmosphere to minimize the damage of LAO/STO 2DEG during annealing process[118]. After annealing process, the resistance of the fabricated sample was tested to confirm if the STO surface was recovered (resistance more than 20 Giga ohm).

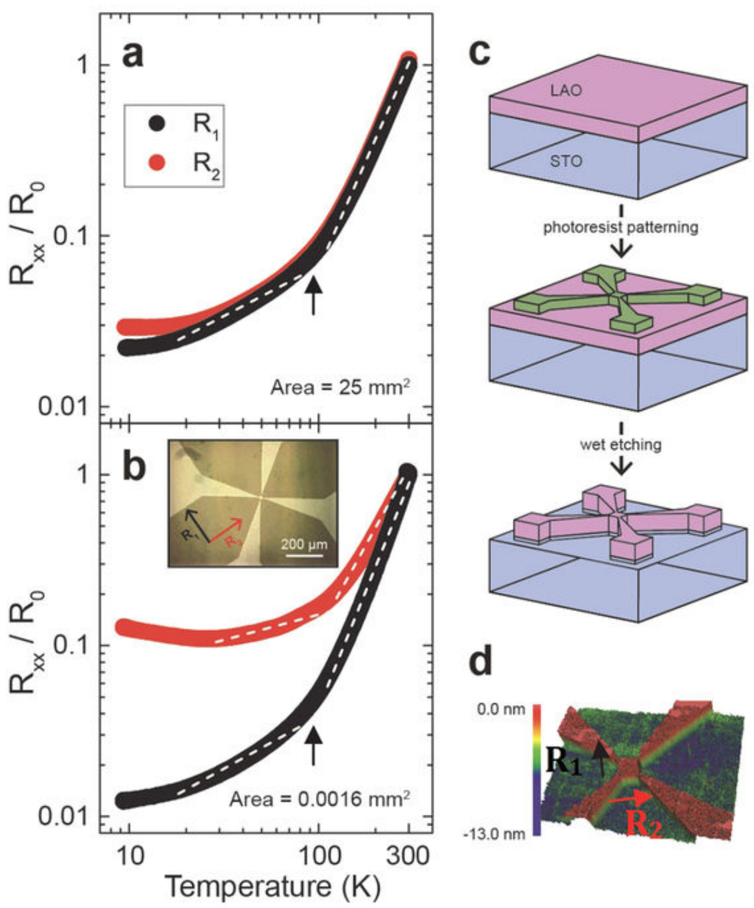

Figure 4-6. AO/STO sample before (a) and after (b) patterning. R1 and R2 indicate resistances taken with current and voltage contact configuration rotated by 90° (see inset of (b) and (d)). Inset is an optical microscopy image of the etched van der Pauw pattern. The black arrow and white dashed lines in (a) and (b) are a guide to the eye to show the position of the cubic-tetragonal transition and the slope change in R (T). The process of etching the sample is shown in (c). A photoresist mask is patterned on bare LAO/STO, which is subsequently etched. The mask is removed, leaving only the conductive interface covered by the pattern. After the process is complete, the sample topography was imaged using an optical profilometer (d) (reproduced from reference 116).

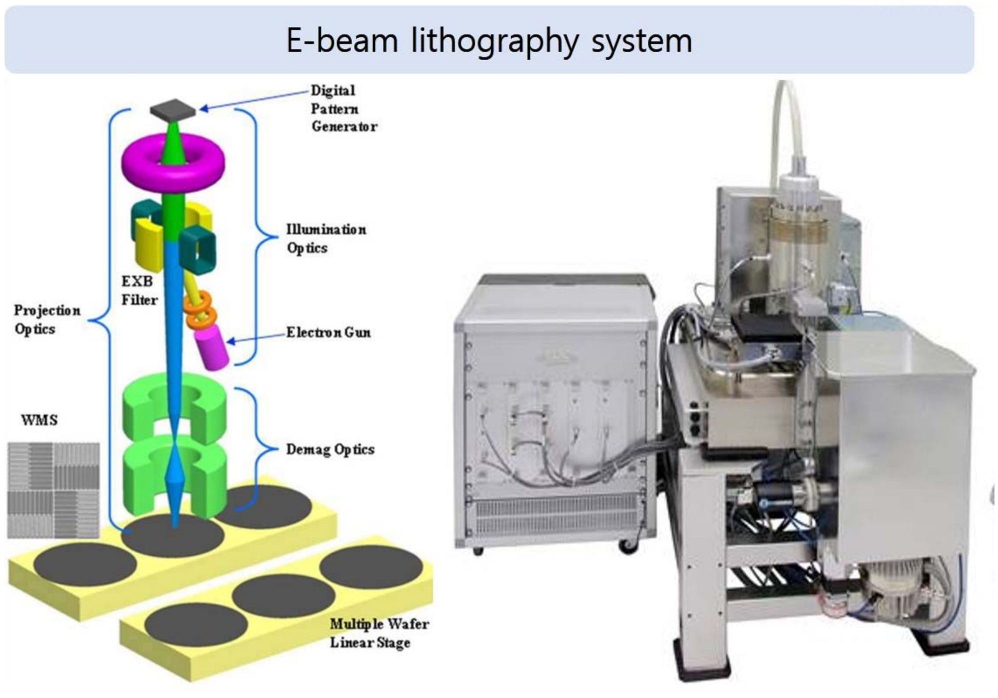

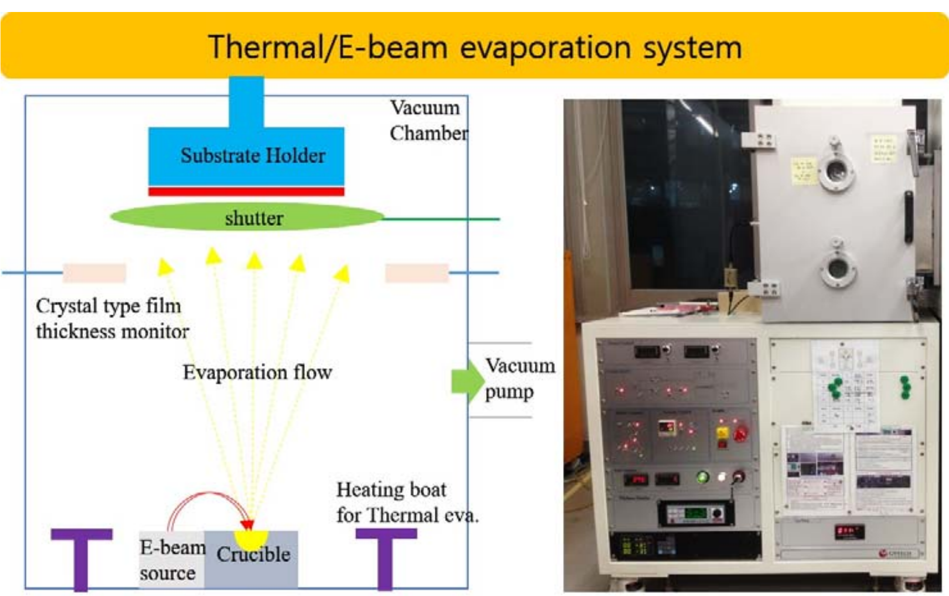

Figure 4-7. (Top) E-beam lithography system. Specifications: 2.1 nm beam size for 100 keV with 7 nA beam current, ≤ 5 nm of line width, Address grid resolution around 1 nm (1 mm main field), and beam voltage range of 30 ~ 100 keV. (Bottom) Thermal/e-beam evaporation system.

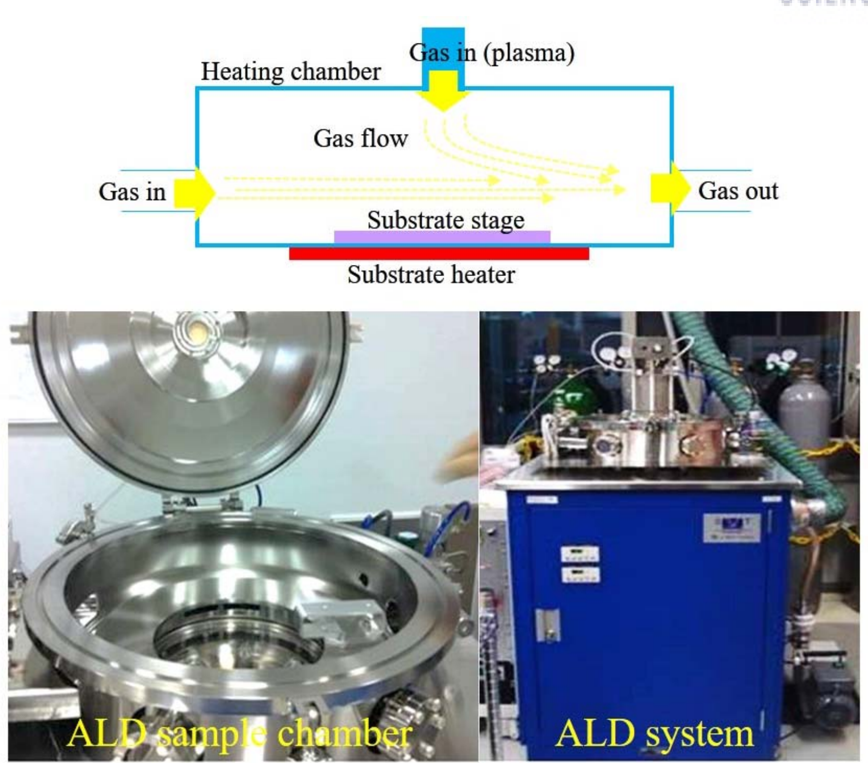

Figure 4-8. Thermal annealing system of Atomic Layer Deposition (ALD) chamber. Specific heating range is up to 500 ˚C with up to 100 sccm flow gas of oxygen, argon, nitrogen, and so on.

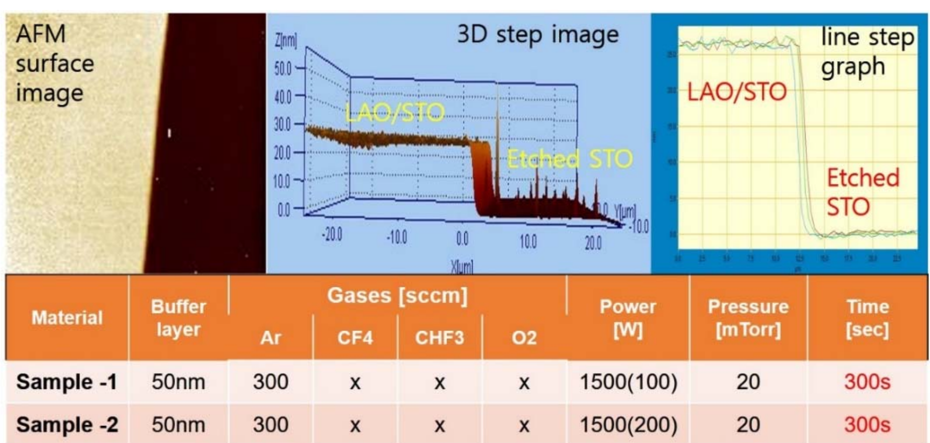

Material	Buffer layer	Gases [sccm]				Power [W]	Pressure [mTorr]	Time [sec]
		Ar	CF4	CHF3	O2			
Sample -1	50nm	300	x	x	x	1500(100)	20	300s
Sample -2	50nm	300	x	x	x	1500(200)	20	300s

Figure 4-9. Reactive ion etching (RIE) condition set-up for top-down process. Atomic force microscope (AFM) image of etched LAO/STO and etched STO surface (up) and its RIE test condition (down). When pattering the H-bar type geometry of LAO/STO 2DEG, the estimated etching rate of LAO/STO was ~ 5 nm/min with plasma power 1500 W and deep power 200 W.

4.3. Test equipment

Sample's electrical connection

Fabricated sample (5 mm x 5 mm) has 12 electrode with 200 μm x 350 μm size. Each of electrode was connected with PPMS sample puck using copper wire. And the sample was stood up to apply parallel field to sample plane as shown in figure 4-10.

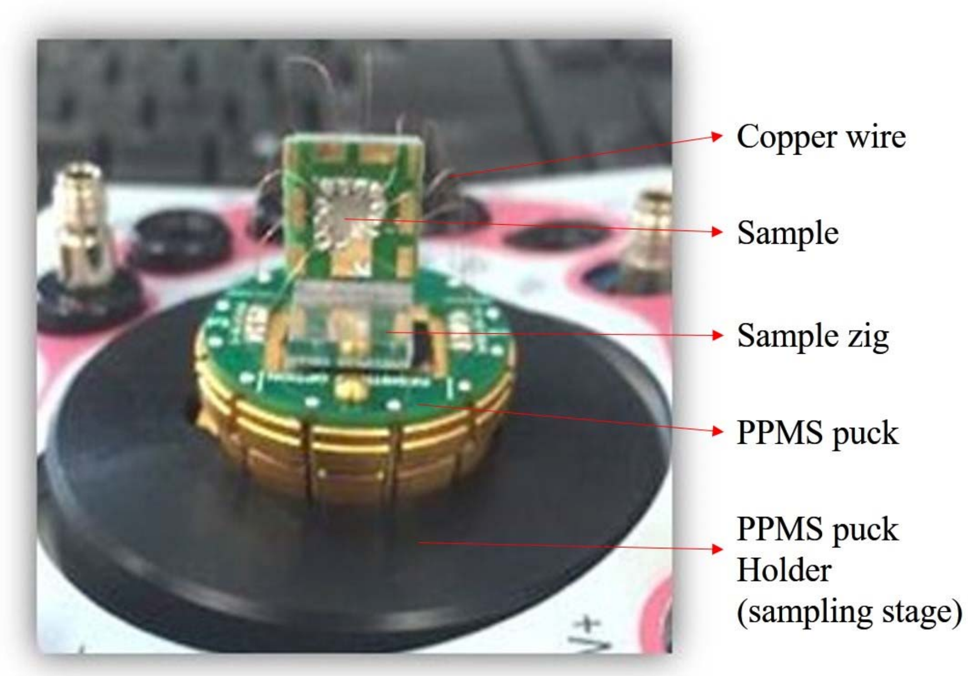

Figure 4-10. Sample image connected to PPMS puck before the electrical measurement.

Electrical Measurement

All electrical measurement was performed in a Physical Property Measurement System (PPMS) with vacuum condition. Electrical contacts to bonding pads on the device are made by using an Ag paste with copper wires. The non-local electrical measurement was performed using Keithely source meter (K2636) and nanovoltameter (K2182). And the 4-terminal DC measurements were compared with AC measurements utilizing K6221 and K2182. No significant differences in the noise level were found between the AC and DC measurements. When an electric current flows one of the lines of the H-bar

structures, a transverse spin current due to the spin Hall effect is induced in the central line. Subsequently, this spin current produces a non-local voltage difference in the next vertical line of the H-bar structures via the inverse spin Hall effect. The non-local spin diffusion were further confirmed with spin precession behavior under parallel magnetic field sweep. Electrical measurement configuration with PPMS system was shown in figure 4-11. All electrical measurement system was grounded to the land through the building to minimize unexpected noise signal.

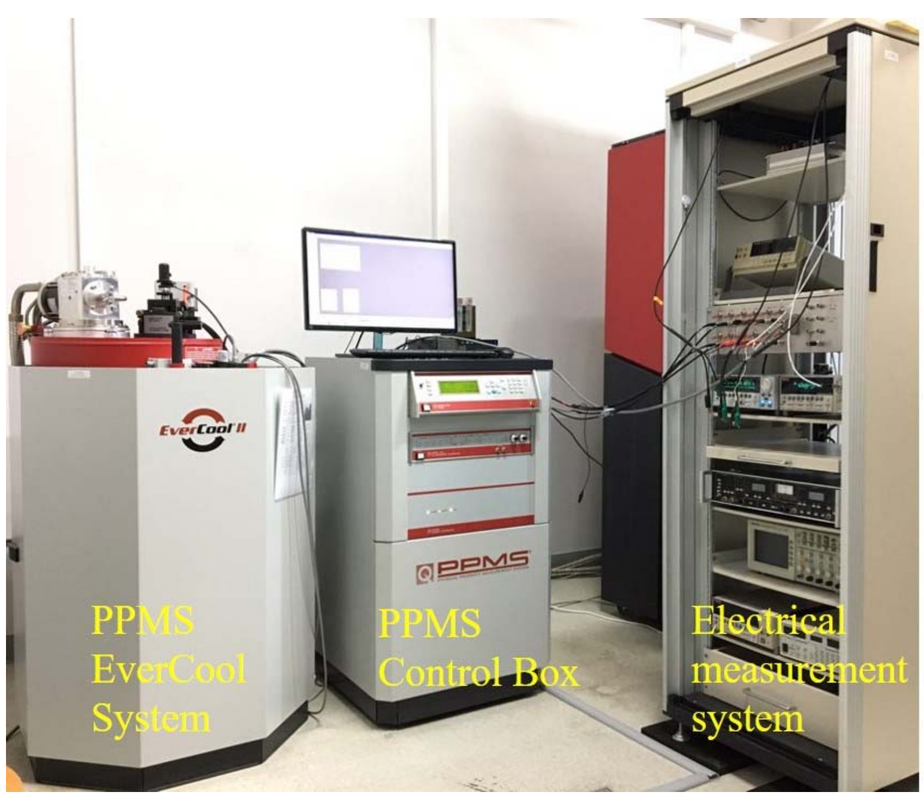

Figure 4-11. Physical properties measurement system (PPMS) and connected electrical measurement system. PPMS has specification of temperature range 1.8 K - 400 K with temperature accuracy of ± 0.5 % , continuous low-temperature control, controlled temperature sweep mode, and magnet range ± 9 T with field resolution of 0.3 Oe to 1 T and 3 Oe to 9 T.

Chapter 5.

Non-Local Spin Signal in LAO/STO

5.1 Introduction (Idea & motivation)

The interface between LaAlO3 (LAO) and SrTiO3 (STO), an archetype of conductive oxide heterointerfaces, has demonstrated various distinctive electronic behaviors[68, 79, 89, 93, 120-122], such as superconductivity[83, 86, 93, 123], ferromagnetism[76, 80, 84, 87, 124, 125], and coexistence of them[71-73]18-20. In particular, this conductive heterointerface provides a unique electronic system as the inversion symmetry is broken by the structure itself. The low dimensionality together with broken inversion symmetry of this interface makes it an important test-bed for the study of charge and spin transport under the electric-field gradient5. Itinerant electrons at the LAO/STO interface are predicted to have a robust spin coherence with an exceptionally long spin relaxation time[126]. The broken inversion symmetry at this heterointerface leads to a Rashba spin-orbit coupling[83, 120, 123, 127] that can be exploited for the manipulation of spin as well as the effective spin-charge conversion via the spin Hall effect. The strength of the Rashba interaction can be directly tuned by applying a gate voltage[83, 114, 123, 128, 129]. The gate tunability of the Rashba interaction in the LAO/STO can be used for a spin field-effect transistor, where the spin precession is governed by the gate-controllable Rashba field[28, 29]. At the same time, the spin-orbit interaction at this heterointerface could also allow us to generate and detect a spin current through the spin Hall effect[52, 54, 55, 130, 131].

Though the LAO/STO interface has been perceived as a promising platform for spintronic research, the non-local spin transport, which is one of core experiments to characterize spin properties, has suffered severe technical problems. One of the major challenges is the conflict between the condition for the efficient spin injection and the condition for the conductive electron gas formation at the interface; while the electron gas formation requires the LAO layer to be thick enough, such a thick layer works as a tunnel barrier with excessively high resistance and prevents efficient spin injection into the electron gas[132, 133]. One possible way to resolve this conflict is to adopt 3-terminal geometry with large area contacts[81] for spin injection, which allows the reduction of the contact resistance while maintaining the LAO layer thickness. There are concerns and debates, however, about this approach. Because this approach makes distinction between spin and charge transport signals difficult, the Hanle measurement, one of key experiments for the spin transport, is subject to spurious spin transport signals due to the

spin-dependent hopping through defects at the contact[82, 134]. Thus, coherent study on the spin transport and its dynamic in this system need to be performed within a separated spin and charge transport, i.e. a non-local spin diffusion. Here, we adopt an alternative approach to generate pure spin current by exploiting the spin Hall effect. In a system with a strong spin-orbit interaction, the longitudinal charge current gives rise to transverse spin current via the spin Hall effect. The oxide heterointerface can be well suited for the generation of the spin polarized current using the spin Hall effect and further study on the non-local spin diffusion, which has been prohibited due to inefficient spin injection using a ferromagnetic electrode.

In this work, we report the non-local spin diffusion at LAO/STO interface induced by the spin Hall effect. The Hall-bar (H-bar) like geometry was employed to generate a transverse spin polarized current, which in turn can be detected by the inverse spin Hall effect. The observed spin precession signatures clearly demonstrated the non-local spin diffusion as well as effective spin charge conversion at this oxide heterointerface. Results show that both D'yakonov-Perel' (DP) and Elliott-Yafet (EY) spin relaxations involve at low temperature, but Elliott-Yafet (EY) spin relaxation prevails above 10 K in this system. Most notably, the obtained spin Hall angle determined by the non-local spin diffusion was as high as ~ 0.15 ± 0.05 on average. This observation of strong spin-charge conversion is an important groundwork for the spin-orbitronic application of oxide heterointerfaces.

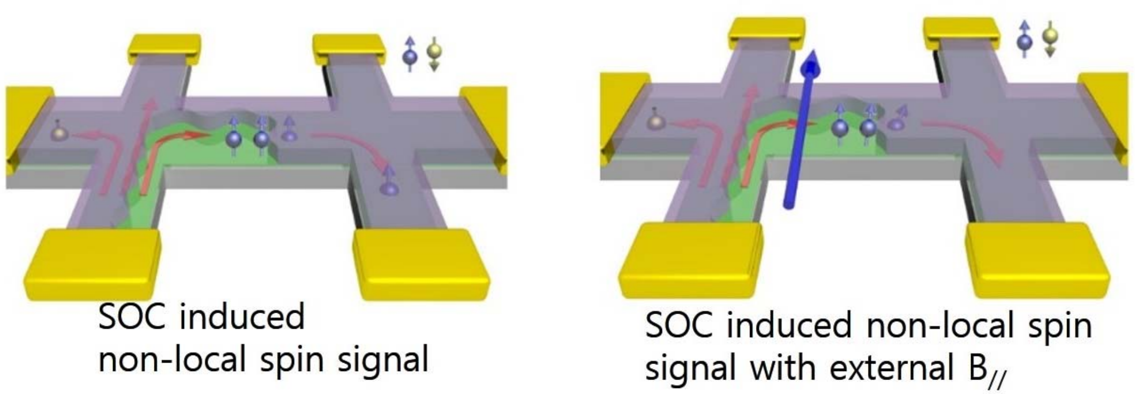

Figure 5-1. Experimental plane with H-bar type sample geometry. i) SHE & ISHE induced non-local spin signal though the oxide interface. ii) Non-local spin precession signal by external magnetic field (Hanle curve) and obtain Rashba SOC constant & spin diffusion length & spin life time at LAO/STO 2DEG. iii) channel length dependence and temperature dependence of the spin signal and analysis the mechanism of SOC.

5.2 Fabricated device property (basic property)

After fabrication and inserted into PPMS, first we measured local IV curve and temperature dependent resistance. As mentioned above, thermal effect such as Seebeck and Ettingshaugen, those effect should be subtracted by linear relationship of local IV curve. So the local charge transport properties of the device shows semi-logarithmic local *I-V* curves between 2-terminal probes shown in the inset (3-4, 5-6, 7-8, 9-10, and 11-12). The blue line is a linear fit to the data obtained from 3-4 terminals confirming Ohmic contacts between the conductive interfaces and the Ti/Au electrodes. And temperature dependence of local line resistance between probe 1 and 2 represents metallic behavior and contact is clearly stable until low temperature.

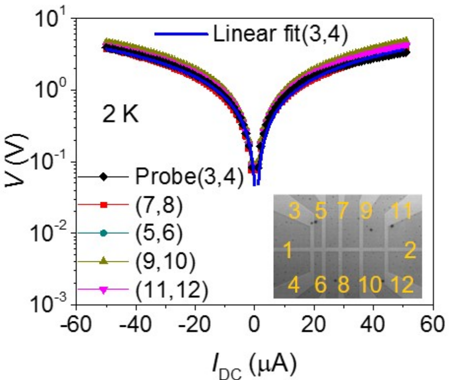

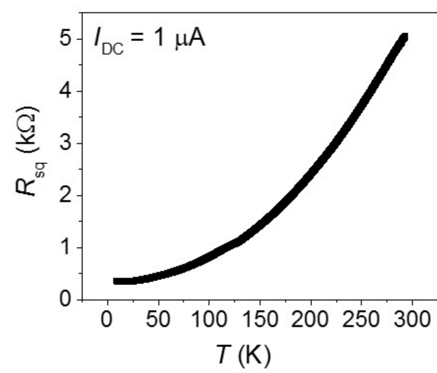

Figure 5-2. Local IV curve (left) and temperature dependent resistance behavior of device (right). Local IV curve should be linear relation to remove thermal effect or unstable detecting voltage. And Resistance vs Temperature curve clearly shown the metallic behavior.

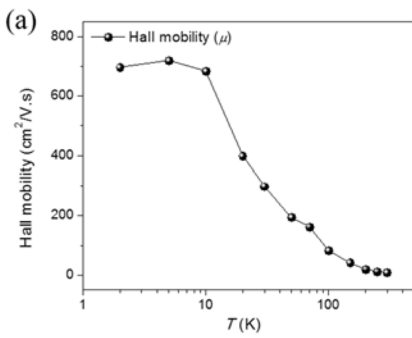

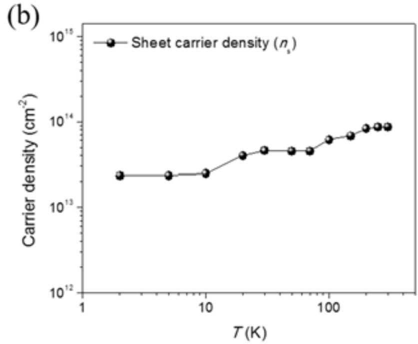

Figure 5-3. Local transport properties measured for the device A. (a) Temperature dependence of Hall mobility. (b) Temperature dependence of sheet carrier density.

The non-local magnetoresistance (MR) could be derived from a number of spurious responses, such as field dependent contact resistance, trace of local MR, offset of local Hall effect, anomalous Hall effect, other non-local signal related to thermoelectric effect, etc. Therefore, it is necessary to carefully investigate device characteristic and local MR together with constraints for the spin Hall regime ($\lambda_e << w << \lambda_s$). An electrical contact to the conductive interface underneath the LAO barrier has been a critical issue in fabricating a microelectronic device based on the LAO/STO. We followed the methods used by Goswami *et al*. to improve the metallic contact to the conductive interface[135]. A key procedure to improve the contact was the deposition of an imbedded Ti/Au layer immediately after a reactive ion etching process. Further details of the contact fabrication are described in the section of sample growth and device fabrication. Figure 5-2 (a) shows semi-logarithmic *I-V* curves between labeled contacts of the device A as displayed in the inset. The linear fit displayed excellent Ohmic contacts between the conductive interfaces and the Ti/Au electrodes. Therefore, we can effectively exclude effects from field-dependent impurity scattering at the interface, when we characterize the field-dependent non-local signal.

The temperature dependence of local resistance in our device A is displayed in figure 5-2 (b), which follows general metallic behavior of the LAO/STO interface[136]. The temperature dependence of mobility and carrier concentration obtained by Hall effect measurement are displayed in figure 5-3. The measured sheet resistance (R_s) was ~ 300 Ω at 2 K. The sheet carrier density (n_s) was $\sim 2.5\times10^{13}\ \mathrm{cm}^{-2}$ at 2 K. Given the 2-dimensional electron gas (2DEG) characteristic of the conductive interface, the Fermi wavenumber is given as $k_\mathrm{F} = (2\pi n_\mathrm{s})^{1/2} \sim 1.25\times10^{7}\,\mathrm{cm}^{-1}$ and the Fermi velocity is $v_\mathrm{F} = \frac{\hbar k_\mathrm{F}}{m^*} \sim 4.82\times10^{6}\,\mathrm{cm/s}$. Here, the effective mass m^* is taken as $3m_e$, where m_e is the mass of the free electron[137]. The momentum scattering time given by the macroscopic Ohm's law is $\tau = \frac{m^* \sigma_\mathrm{s}}{n_\mathrm{s} e^2} \sim$ 1.42 ps. Thus, the mean free path can be obtained as $\lambda_\mathrm{e} = v_\mathrm{F}\tau \sim 68.4$ nm, which is sufficiently smaller than $w \sim 500$ nm, satisfying the condition $w >> \lambda_e$. Considering λ_s is generally much longer than λ_e, our device geometry could also satisfy the other constraint $w << \lambda_s$, which will be confirmed later in non-local measurement.

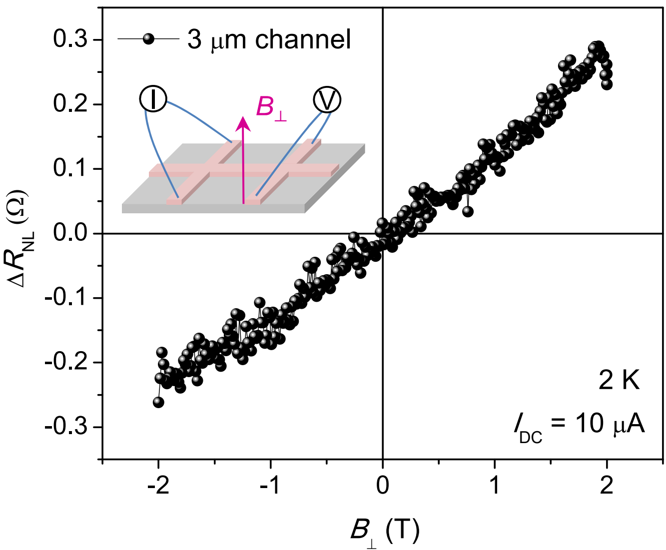

Figure 5-4. Non-local MR measured as a function of perpendicular magnetic field for the device A. Measurements taken with I_{DC} = 10 μA for the 3 μm channel of device A. The non-local voltage showed only a trace of a Hall voltage offset, which is directly proportional to the applied perpendicular magnetic field.

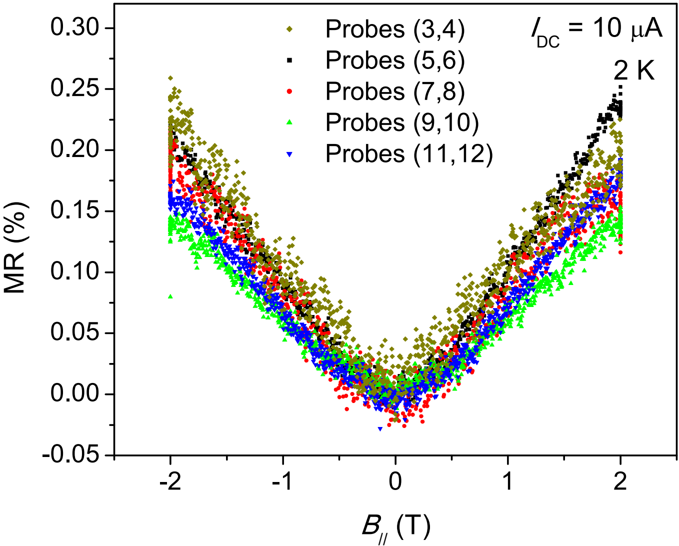

Figure 5-5. Local MRs measured as a function of parallel magnetic field for the device A. Measurements taken with I_{DC} = 10 μA for each of the two-terminal probes as shown in the inset of figure 5-2.

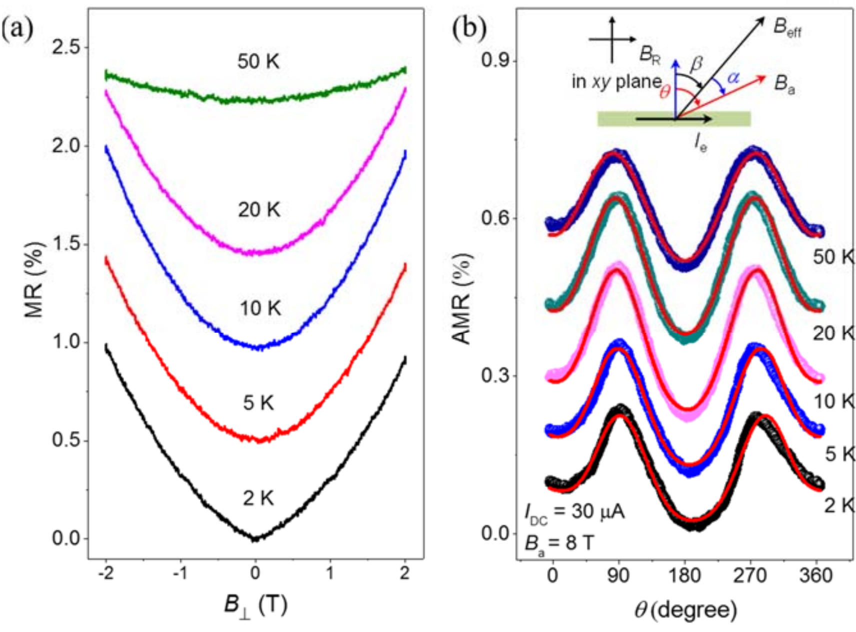

Figure 5-6. (a) MR as a function of perpendicular magnetic field measured for the local line (probe 1-2) at various temperatures (T = 2, 5, 10, 20, and 50 K). The MR curves are shifted vertically for clarity. (b) AMR measured for the local line (probe 1-2) with a source current of I_{DC} = 30 μA at B_a = 8 T and T = 2, 5, 10, 20, and 50 K. The inset shows the measurement configuration with respect to the applied magnetic field (B_a) in the plane. The angle dependent AMR displays an asymmetry between θ = 0 and 180, which implies the presence of equivalent field arisen from the Rashba spin-orbit interaction (denoted as B_R in the inset).

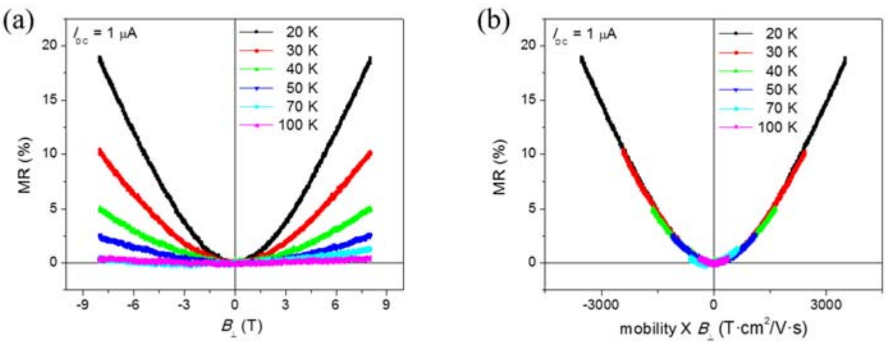

Figure 5-7. Temperature dependent behavior of magnetoresistances (MRs) measured for the device A. (a) MRs as a function of perpendicular magnetic field measured at T = 20, 30, 40, 50, 70, and 100 K. (b) MR curves plotted according to the generalized Kohler's rule $\Delta\rho/\rho_0 \sim f(\mu H)$. All curves excellently collapse in a single function displaying universal behavior.

Figure 5-6 displays magnetoresistance (MR) data measured at the local line between terminal 1 and 2, where the MR was defined as $\mathrm{MR} = [R(B) - R(B=0)] / R(B=0)$. The observed MR displays parabolic field dependence satisfying the classical Kohler's rule of $\Delta\rho / \rho_0 \sim B^2$, arising from the cyclic motion of an electron in a magnetic field. The momentum scattering of carriers reduces this MR since it interrupts the cyclotron motion. Thus, the temperature dependence of MRs can be well scaled to the universal behavior of the generalized Kohler's rule[138] $\Delta\rho / \rho_0 \sim f(\mu B)$ (see figure 5-7). However, a significant deviation from $\sim B^2$ behavior was observed at 2 K, especially at low field. Such deviation is associated with quantum corrections to the diffusive transport, i.e. weak localization (WL) and/or weak anti-localization (WAL) from the interferences of self-crossing electron trajectories. Several studies have successfully determined Rashba spin-orbit coupling constant and its gate tunability by analyzing low-temperature MR behavior based on the WL/WAL theory[83, 119, 128, 129]. In general, whether the LAO/STO sample is in the WL or WAL limit and their gate tunability are highly dependent on the details of the growth conditions[139]. The analysis of the WL/WAL theory yet involves a complex formula with many parameters and can be applicable only at a low temperature.

The strength of the Rashba field at higher temperature can be indirectly inferred from the angle dependence of an anisotropic magnetoresistance (AMR) as done by Narayanapillai *et al*[140]. The epitaxial LAO/STO interface generally forms magnetic domains derived from localized d_{xy} electrons of interfacial Ti^{3+} ions [76, 77, 125]. And itinerant t_{2g} electrons are populated in subsequent TiO_2 layers of STO with a typical depth of ~ a few nm[77]. Due to the presence of interfacial magnetic moments, conduction electrons at this interface display AMR with a two-fold oscillation for the full rotation of in-plane magnetic field, which is regardless of the crystal axes[77, 140]. Similar to the case of a magnetic bilayer[141], the in-plane current introduces a spin orbit torque on the localized domain as long as the spin Hall effect is engaged. Thus, it can be regarded as if there is an equivalent magnetic field corresponding to the spin orbit torque induced by the in-plane charge current and spin Hall effect. Note that although this equivalent field arises from the Rashba spin-orbit interaction, it is different from the Rashba spin-orbit field that leads to the spin splitting energy of the conduction electron; the former is defined by the spin accumulation caused by charge current whereas the latter is defined by the spin-dependent energy-momentum relation in equilibrium. Since the direction of this equivalent field is locked to be perpendicular to the direction of current, the in-plane angle dependent AMR displays an asymmetry between $\theta = 0$ and π, where θ is the angle between applied in-plane field and normal to the electron current[140]. Figure 5-6 (b) displays AMRs measured from the local channel between probe 1 and 2 as a function of the in-plane angle at various temperatures. The observed asymmetry of the AMR clearly suggested that strong spin Hall effect involves in carrier transport even at relatively high temperatures. Thus, we can exploit the proposed H-bar geometry for the study of non-local spin diffusion at the

LAO/STO interface.

5.3 Rashba SOC in LAO/STO (Planer AMR)

The asymmetry of AMR shown in figure 5-6 (b) is also an indicative of strongly coupled charge and spin transport in this system. Here, we estimate the equivalent Rashba-like field from our AMR results following ref. 93[96]. We labeled the B_R for the equivalent field that is normal to the electron flow (see the inset of figure 5-6 (b)). Then, the total effective magnetic field (B_{eff}) experienced by the carriers has its magnitude and direction given by[140]

$$B_{eff}^2 = B_a^2 + B_R^2 + 2B_a B_R \cos\theta \tag{4}$$

$$\alpha = \arctan\left[\frac{B_R \sin\theta}{B_a + B_R \cos\theta}\right] \tag{5}$$

where α is the angle between the applied magnetic field (B_a) and B_{eff}. Then, the angle dependent AMR is given by

$$\mathrm{AMR} = a_0 + a_1 B_{eff} \cos^2(\beta + \phi) + a_2 B_{eff} \cos^4(\beta + \phi) \tag{6}$$

where a_0, a_1, a_2 and ϕ are constants, and β is defined as $\beta = \theta - \alpha$. Fitting eq 6 to the angle dependent AMR can determine the magnitude of B_R[140]. Fitting curves are shown as solid red lines in figure 5-6 (b). The angle dependent AMRs at various applied currents are also displayed in Supporting Information, figure 5-9. Because this equivalent Rashba-like field is originated from the current-induced spin orbit torque, the value of B_R is highly dependent on the current density[140] (see figure 5-10 (a)). For I_{DC} = 30 μA, the extracted B_R value in our device is ~ 1.34 T at 2 K. If we assume 2DEG thickness of 7 nm as reported earlier[88], a current density for 30 μA is 8.57×10^9 A/m^2. For a current density of 10^{12} A/m^2, the corresponding current-driven Rashba-like field is ~ 156 T, although this value relies on the presumed thickness of 2DEG. The estimated Rashba-like field is extremely higher than those obtained for metallic bilayer systems, where current-driven fields are typically less than Tesla for a 10^{12} A/m^2 current density[142, 143]. The extracted B_R value was slightly decreased as the temperature was increased up to 10 K, then it displayed upturn with increasing temperature further (figure 5-10 (b)). These results suggest that strong spin-charge conversion at this heterointerface would also be effective at high temperature.

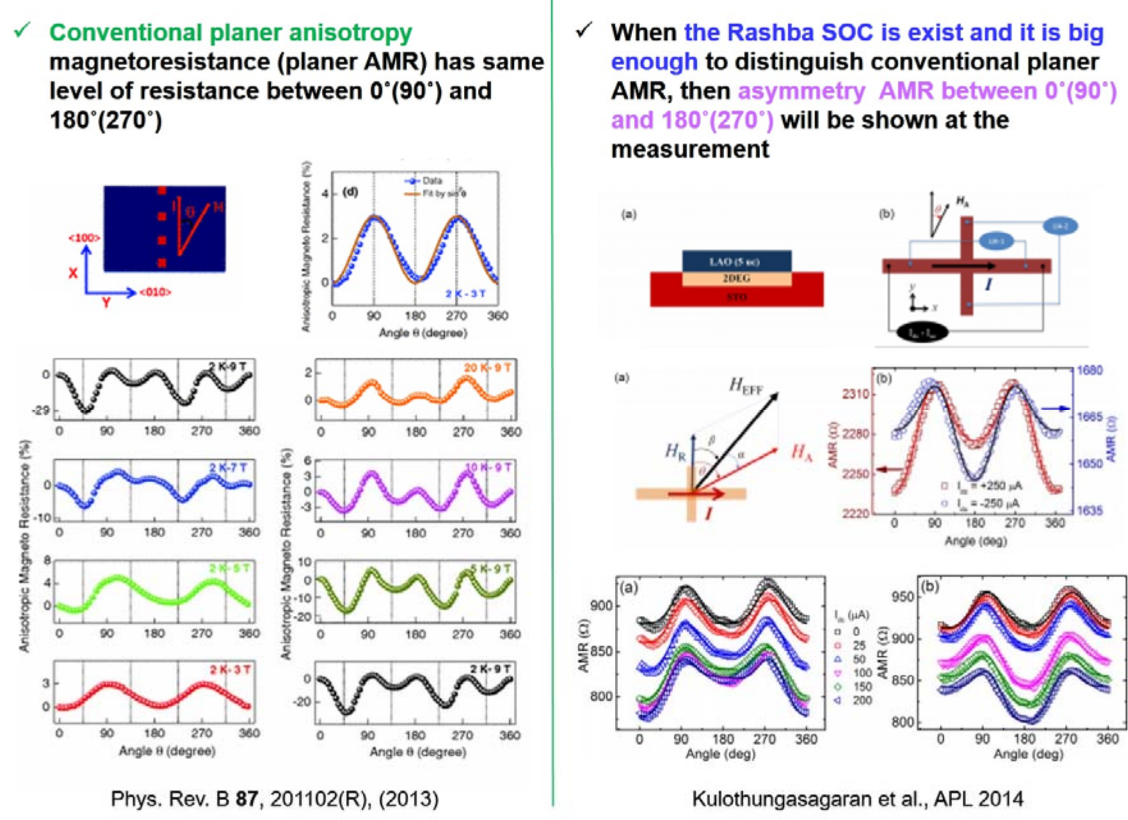

Figure 5-8. Comparison of conventional planer AMR and planer AMR with Rashba SOC at a conductive interface[96, 144]. As already mentioned above chapters, asymmetry AMR also can be the evidence of Rashba SOC (reproduced from reference 96, 144).

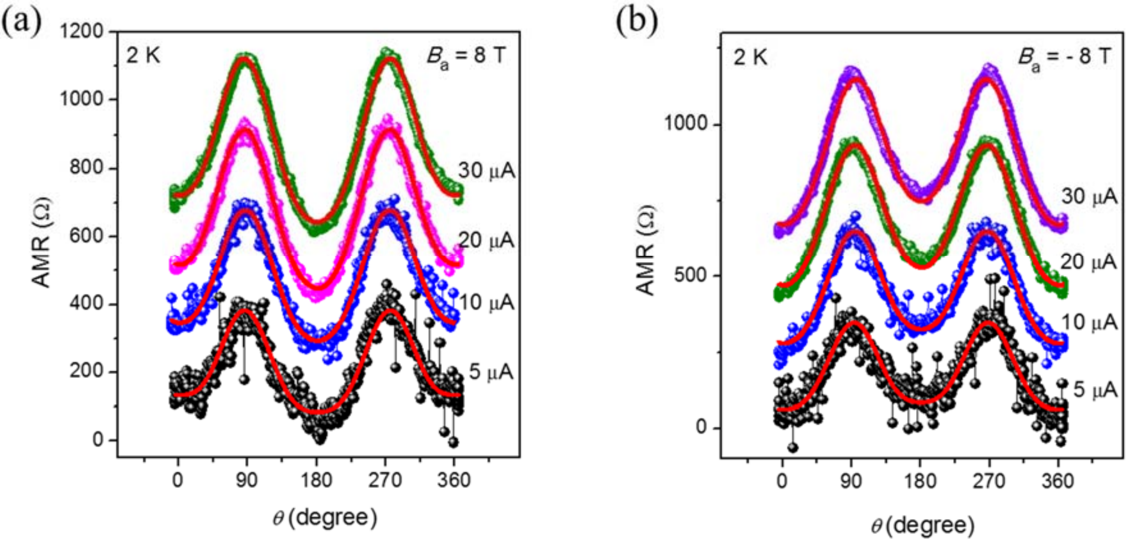

Figure 5-9. Angle-dependent AMR measured for the device A. (a) AMR measured at B = 8 T for I_{DC} = 5, 10, 20, and 30 μA. (b) AMR measured at H = - 8 T for I_{DC} = 5, 10, 20, and 30 μA.

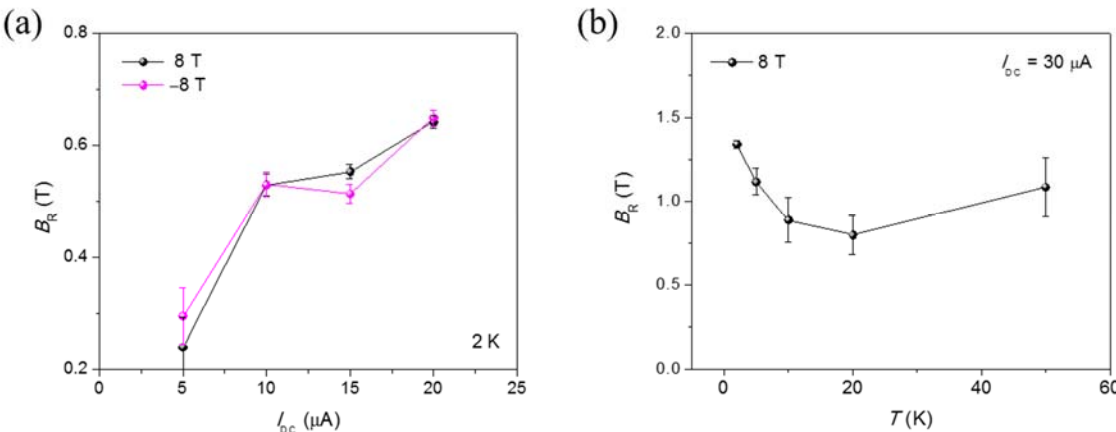

Figure 5-10. The estimated Rashba-like fields. (a) Rashba-like fields for various DC currents. Values were estimated by fitting equation (6) to the results in figure 5-4. (b) Rashba-like fields for various temperatures. Values were estimated by fitting equation (6) to the results in figure 5-6 (b).

5.4 Non-local spin signal depends on the channel length

Figure 5-11 (a) displays a SEM image of the H-bar like device we used for the study of the spin Hall induced spin diffusion. The devices were fabricated on 5 mm x 5 mm STO substrates. Multiple H-bar channels were employed to study the dependence of the spin diffusion on the channel length. Results displayed in the text were mainly obtained from the two devices (device A and device B), which have the same geometry as in figure 5-11 (a). The inset of figure 5-11 (a) exhibits a cross-sectional view of the LAO/STO interface obtained by high-resolution transmission electron microscopy (HR-TEM). The LAO/STO samples used for our devices have typically 10 unit cells (5 nm) of LAO layers grown by the pulsed laser deposition. The HR-TEM image clearly shows that the heterointerface is atomically sharp and free from misfit dislocations. Details of sample growth and device fabrication were described in section of sample growth and device fabrication. In this H-bar geometry as shown in a schematic of figure 5-11 (b), a current through a vertical line can induce the transverse spin diffusion through a bridging channel via the spin Hall effect. If the spin carriers preserve their polarization until they reach the next vertical line, the inverse spin Hall effect can induce a non-local voltage away from the local current. However, one has to be careful in determining such a non-local spin signal. Since the current density spread through the bridging wire, a non-zero Ohmic voltage of non-spin origin can still arise between non-local probes unless the channel length (L) is much longer than the width (w). This non-local Ohmic voltage ($R_{\mathrm{NL}}^{\mathrm{C}}$) is given as $R_{\mathrm{NL}}^{\mathrm{C}} = R_{\mathrm{sq}} \exp\left(-\frac{\pi L}{w}\right)$ from the van der Pauw theorem for L > w, where Rsq is the sheet resistance of the materials. In general, if the channel length is 3 time longer than the width, the Ohmic contribution to the non-local voltage becomes nearly negligible (less than 0.001 %). As shown in figure 5-11 (a), the device channels were fabricated to have width of 500 nm and length of 2, 3, 4, and 5 μm keeping the ratio of L to w greater than 4. Additional constraints on w are needed to single out signal from the spin Hall induced non-local spin diffusion. For instance, the non-local voltage can even be negative in the ballistic regime, i.e. w << λ_e, where λ_e is the electron mean free path[55]. To avoid such non-intuitive features, which make data analysis difficult, we impose both w >> λ_e (diffusive transport regime) and w << λ_s (one dimensional spin transport regime), where λ_s is the electron spin diffusion length. In this regime, the non-local resistance is given by[54]

$$R_{\mathrm{NL}}^{\mathrm{SH}} = \frac{1}{2}\gamma^2 R_{\mathrm{sq}} \frac{w}{\lambda_s} \exp\left(-\frac{L}{\lambda_s}\right) \quad (1)$$

where $\gamma = \frac{\sigma_{xy}^{\mathrm{SH}}}{\sigma_{xx}}$ is the spin Hall coefficient (angle) in the conductive electron gas at the interface.

Here, σ_{xx} is the charge conductivity and $\sigma_{xy}^{\mathrm{SH}}$ is the spin Hall conductivity.

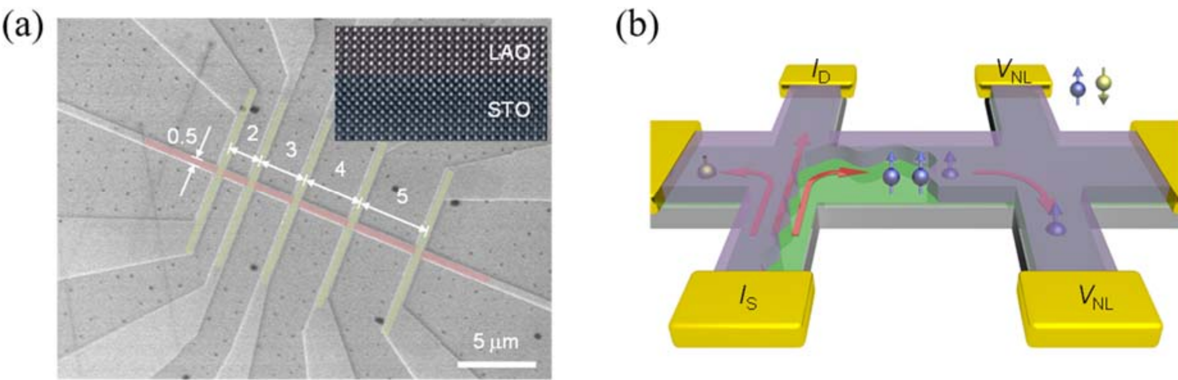

Figure 5-11. Device geometry for the study of spin Hall induced spin diffusion in LAO/STO. (a) SEM image of the non-local device (device A) fabricated on a 5 mm x 5 mm STO substrate. The line width is 500 nm. Channel lengths, i.e., the distances between the centers of consecutive lines, are 2, 3, 4, and 5 µm. The inset shows a cross-sectional high-resolution transmission electron microscope (HR-TEM) image of the LAO/STO interface. (b) Schematic of spin Hall induced non-local spin diffusion and its measurement configuration. In this geometry, local charge current induces a transverse spin current via the spin Hall effect, which in turn produces non-local spin voltage via the inverse spin Hall effect.

The spin Hall induced spin diffusion through the bridging channel in our H-bar device geometry can be confirmed by the signature of a spin precession and its length dependence. The non-local voltage as a function of in-plane magnetic field produces a Hanle curve as shown in figure 5-12 (a). Here, the spin Hall effect induces the spin current along the bridging channel with its polarization perpendicular to the plane. Thus, the in-plane magnetic field causes the Larmor precession of carrier spins. Depending on the degree of precession, the non-local voltage will be applied via the inverse spin Hall effect as long as spin Hall regime ($\lambda_e << w << \lambda_s$) is satisfied. This non-monotonic oscillatory signal can be fitted with[145]

$$R_{\mathrm{NL}}^{\mathrm{SH}} = \frac{1}{2}\gamma^2 R_{\mathrm{sq}} w \,\mathrm{Re}\left[\left(\sqrt{1+i\omega_{\mathrm{B}}\tau_{\mathrm{s}}}/\lambda_{\mathrm{s}}\right) e^{-\left(\sqrt{1+i\omega_{\mathrm{B}}\tau_{\mathrm{s}}}/\lambda_{\mathrm{s}}\right)|L|}\right] \quad (2)$$

where $\omega_{\mathrm{B}} = \Gamma B_{//}$ is the Larmor frequency, Γ is the gyromagnetic ratio for the electron and $B_{//}$ is the applied in-plane magnetic field. In contrast to the typical Hanle signature from a linear spin diffusion, the curve produced by eq 2 displays a dip at zero magnetic field, which stems from the geometry effect[145]. The non-local voltage in response to the perpendicular magnetic field displayed trace of the Hall voltage offset and did not show such oscillatory signature (see figure 5-4). The local MR in response to the in-plane magnetic field exhibits simple linear behavior as presented in Supporting Information, figure 5-5. These two MR measurements confirmed that the observed Hanle curve is not associated with the Ohmic contribution. The Hanle curves shown in figure 5-12 (a) displayed narrower width for the longer channel since the transit time for the carrier spins to precess was increased. The magnitude of the Hanle signal also decayed exponentially as the channel length was increased as shown in figure 5-12 (b). These two signatures unambiguously demonstrated the validity of spin Hall induced spin diffusion in our device. Fitting eq 2 to the measured Hanle curve at 2 K yielded $\gamma \sim 0.10$ and $\lambda_{\mathrm{s}} \sim 0.90\,\mu\mathrm{m}$ for 2 μm and $\gamma \sim 0.089$ and $\lambda_{\mathrm{s}} \sim 0.88\,\mu\mathrm{m}$ for 3 μm, respectively. The spin diffusion length can also be obtained from the dependence of the non-local spin signal on channel length. Fitting eq 1 to the recorded non-local voltages at 2 K produced $\gamma \sim 0.067$ and $\lambda_{\mathrm{s}} \sim 1.4\,\mu\mathrm{m}$ for the device A and $\gamma \sim 0.10$ and $\lambda_{\mathrm{s}} \sim 1.5\,\mu\mathrm{m}$ for the device B, respectively. The obtained parameters showed large sample to sample variation. Because our device fabrication involves many procedures, the conductive interfaces could be partially degraded. Higher channel resistance generally underestimates the non-local spin signal leading to the variations for the extracted spin Hall angle. The average values of parameters obtained from Hanle curves of seven individually fabricated samples were $\gamma \sim 0.15 \pm 0.05$ and $\lambda_{\mathrm{s}} \sim 1.05 \pm 0.33\,\mu\mathrm{m}$ at 2 K.

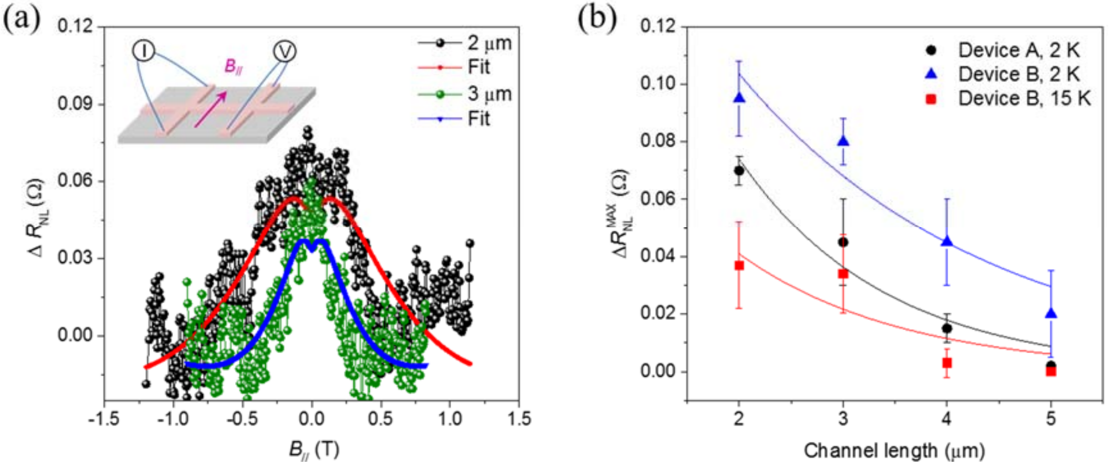

Figure 5-12. Dependence of non-local spin signals on channel length. (a) Non-local voltage as a function of in-plane magnetic field measured for the channels with lengths of 2 and 3 μm. The inset displays a measurement configuration with the relative orientation of the in-plane magnetic field. Red and blue lines are fits of equation 2 to the data. The 3 μm channel produced a narrower Hanle curve due to increased transit time for spin. (b) The magnitude of the non-local spin voltage as a function of the channel length measured for the device A and B. Solid lines are fits of equation 1 to the data.

5.5 Non-local spin signal with temperature & Relaxation mechanism

Figure 5-13 (a) displays Hanle curves measured for the 3 μm channel of the device B at various temperatures. And the extracted parameters obtained by fitting with eq 2 are shown in figure 5-13 (b). The spin diffusion length and time exhibit general trend of reduction with increasing temperature. The signature of Hanle curve in our devices nearly disappeared when the temperature was greater than 20 K, which implies significant reduction of λ_s above 20 K. The LAO/STO systems typically display strong temperature dependence of a momentum scattering rate $1/\tau_p$, especially above 20 K (see figure 5-3). Considering that λ_s depends on $1/\tau_p$, the temperature dependence of λ_s is natural. In addition, the spin Hall regime ($\lambda_e << w << \lambda_s$) of our device may be valid only at low temperatures. To gain an insight into the spin relaxation in the LAO/STO system, we examined below the relation between τ_p and τ_s. Within the DP mechanism, the spin relaxation time τ_s is inversely proportional to the momentum relaxation time τ_p as given by $\frac{1}{\tau_{s,DP}} = (\frac{\Delta_{DP}^2}{\hbar^2})\tau_p$, where Δ_{DP} is the effective spin-orbit coupling[146]. On

the other hand, the spin relaxation associated with the EY mechanism is directly proportional to the momentum scattering time as given by $\tau_{\mathrm{s,\,EY}} = \tau_{\mathrm{p}} /(\Delta g)^2$, where Δg is a shift of the free electron g factor in a solid[147, 148]. Since the Ti 3d conduction band is significantly altered in STO[137], the EY spin relaxation could be also considerable. If above two mechanisms are independent of each other, then the total spin relaxation rate can be determined as $\frac{1}{\tau_{\mathrm{s}}} = \frac{1}{\tau_{\mathrm{s,\,EY}}} + \frac{1}{\tau_{\mathrm{s,\,DP}}}$, which leads to expression[149]

$$\frac{\tau_{\mathrm{p}}}{\tau_{\mathrm{s}}} = (\Delta g)^2 + \left(\frac{\Delta_{\mathrm{DP}}^2}{\hbar^2}\right)\tau_{\mathrm{p}}^2 \qquad (3)$$

Figure 5-13 (c) displays the plot of $\tau_{\mathrm{p}} / \tau_{\mathrm{s}}$ versus τ_{p}^2. Here, we used τ_{s} values obtained from Hanle curve fits and τ_{p} values taken from the Hall mobilities. The slope and y intercept of a linear fit can provide crude estimation of Δ_{DP} and Δg. The obtained values are Δ_{DP} ~ 30 μeV and Δg ~ 0.068. Then, the spin relaxation times for individual mechanisms can be calculated from the values of Δ_{DP} and Δg. If we assume Δ_{DP} and Δg are temperature independent, temperature dependent behavior of $\tau_{\mathrm{s,\,DP}}(T)$ and $\tau_{\mathrm{s,\,EY}}(T)$ can be obtained with τ_{p} from the Hall mobility. Figure 5-13 (d) displays the estimated $\tau_{\mathrm{s,\,DP}}(T)$ and $\tau_{\mathrm{s,\,EY}}(T)$ up to 100 K, where the variations of Δ_{DP} and Δg start to be considerable due to thermal fluctuations. At 2 K, $\tau_{\mathrm{s,\,DP}}$ ~ 394 ps and $\tau_{\mathrm{s,\,EY}}$ ~ 251 ps, respectively. Both EY and DP mechanisms involve in spin relaxation up to 10 K. As the temperature increases further, EY spin relaxation dominates in our sample. Engineering 2DEG interface for the mobility enhancement is mandatory to study spin transport at higher temperature. Recently, several methods have shown that the mobility of 2DEG at the STO surface can be increased to the order of 10^4 $\mathrm{cm^2/V \cdot s}$[61, 62, 100, 150].

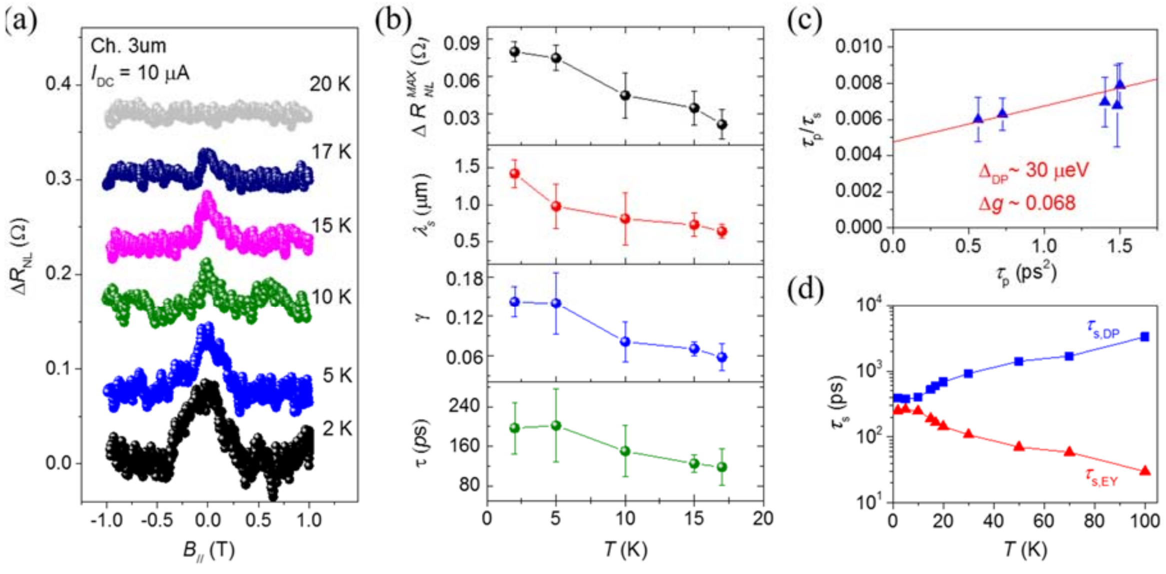

Figure 5-13. Temperature dependence of non-local spin signals measured for the device B. (a) Non-local spin resistance as a function of in-plane magnetic field for the channel of 3 μm measured at 2, 5, 10, 15, 17 K. The non-local spin signals are shifted vertically for clarity. (b) Temperature dependence of the extracted parameters by fitting with equation 2 to the measured Hanle curves. From top to bottom, the magnitude of non-local spin resistance, spin diffusion length, spin Hall angle, and spin relaxation time are displayed. (c) The plot of τ_p / τ_s versus τ_p^2, obtained from temperature dependent τ_s and τ_p values. The red line is a linear fit. The slope and y intercept of a linear fit yielded Δ_{DP} ~ 30 μeV and Δg ~ 0.068. (d) The estimated EY spin relaxation time $\tau_{s,EY}$ and DP spin relaxation time $\tau_{s,DP}$ as a function of temperature.

$$\frac{1}{\tau_{s,EY}} = (\Delta g)^2 \frac{1}{\tau_p}$$

Elliott-Yafet mechanism

Dyakonov Perel mechanism

$$\frac{1}{\tau_{s,DP}} = \left(\frac{\Delta_{DP}^2}{\hbar^2}\right)\tau_p$$

Figure 5-14. Major two types of spin relaxation mechanism of Elliott-Yafet & Dyakonov-Perel' mechanism.

5.6. Summary

A 2-dimensional electron gas emerged at a LaAlO3/SrTiO3 interface is an ideal system for ‘spin-orbitronics’ as the structure itself strongly couple the spin and orbital degree of freedom through the Rashba spin-orbit interaction. One of core experiments towards this direction is the non-local spin transport measurement, which has remained elusive due to the low spin injection efficiency to this system.

In this work, we studied non-local spin transport by generating spin current not from a ferromagnetic electrode but through the inherent spin Hall effect. The strongly coupled charge and spin transport at this heterointerface is the key to realize this approach. At this point, it is not clear whether the intrinsic and extrinsic spin Hall mechanism mainly accounts for the effective spin-charge conversion in this system. Further detailed study with an artificial engineering of the epitaxial interface may resolve the mechanism of the spin Hall effect. The estimated spin Hall angle on average was $\gamma \sim 0.15 \pm 0.05$ at 2 K. This value is extremely large compared to the values obtained from bulk transition metals with the non-local spin transport measurement. Moreover, this non-local experiment significantly underestimate the spin Hall angle, especially for highly resistive materials[142, 151] For instant, the obtained γ for Ta by using non-local spin valve measurement was 0.0037[152], while it was estimated to be 0.15[142] by using spin torque induced ferromagnetic resonance technique. The low-dimensionality together with the broken inversion symmetry in this conductive interface might have led to such strong spin-charge conversion.

Here we bypass the problem by generating a spin current not through the spin injection from outside but instead through the inherent spin Hall effect, and demonstrate the non-local spin transport. The analysis on the non-local spin voltage, confirmed by the signature of a Larmor spin precession and its length dependence, displays that both D’yakonov-Perel’ and Elliott-Yafet mechanisms involve in the spin relaxation at low temperature. Our results show that the oxide heterointerface is highly efficient in spin-charge conversion with exceptionally strong spin Hall coefficient $\gamma \sim 0.15 \pm 0.05$ and could be an outstanding platform for the study of coupled charge and spin transport phenomena and their electronic applications.

References

1. Uhlenbeck, G. E.; Goudsmit, S. *Die Naturwissenschaften* **1925,** 13, (47), 953-954.
2. Uhlenbeck, G. E.; Goudsmit, S. *Nature* **1926,** 117, 264-265.
3. Thomson, W. *Proceedings of the Royal Society of Londen* **1856,** 8, 546-550.
4. Grunberg, P.; Schreiber, R.; Pang, Y.; Brodsky, M. B.; Sowers, H. *Phys Rev Lett* **1986,** 57, (19), 2442-2445.
5. Baibich, M. N.; Broto, J. M.; Fert, A.; Nguyen Van Dau, F.; Petroff, F.; Etienne, P.; Creuzet, G.; Friederich, A.; Chazelas, J. *Phys Rev Lett* **1988,** 61, (21), 2472-2475.
6. 한석희; 김동영; 권해웅; 홍수열; 손대락; 김건우; 김철기; 이상호; 홍종일; 박병국; 이경진; 유천열; 이현우; 최석봉; 김동현; 구현철; 장준연; 한동수; 김상국; 정종율; 민병철; 이기석, *자성재료와 스핀트로닉스 (Magnetic materials and spintronics)*. 한국자기학회: 2014.
7. Takahashi, S.; Maekawa, S. *science and technology of advanced materials* **2008,** 9, 014105.
8. Dash, S. P.; Sharma, S.; Patel, R. S.; de Jong, M. P.; Jansen, R. *Nature* **2009,** 462, (7272), 491-494.
9. Jansen, R. *Nat Mater* **2012,** 11, (5), 400-8.
10. Jansen, R.; Dash, S. P.; Sharma, S.; Min, B.-C. *Semiconductor Science and Technology* **2012,** 27, 083001.
11. Balakrishnan, J. Spin transport studies in graphene. Ph. D. Thesis, National University of Singaphore, 2013.
12. Lou, X.; Adelmann, C.; Crooker, S. A.; Garlid, E. S.; Zhang, J.; Reddy, K. S. M.; Flexner, S. D.; Palmstrøm, C. J.; Crowell, P. A. *Nat Phys* **2007,** 3, (3), 197-202.
13. Min, B.-C. *Journal of the Korean Magnetics Society* **2011,** 21, (2), 67-76.
14. Žutić, I.; Fabian, J.; Das Sarma, S. *Reviews of Modern Physics* **2004,** 76, (2), 323-410.
15. Fabian, J.; Sarma, S. D. *Journal of Vacuum Science & Technology B: Microelectronics and Nanometer Structures* **1999,** 17, (4), 1708.
16. Manchon, A.; Koo, H. C.; Nitta, J.; Frolov, S. M.; Duine, R. A. *Nat Mater* **2015,** 14, (9), 871-882.
17. Maekawa, S.; Valenzuela, S. O.; Saitoh, E.; Kimura, T., *Spin Current*. Oxford University Press: 2012.
18. Yuan, H.; Bahramy, M. S.; Morimoto, K.; Wu, S.; Nomura, K.; Yang, B.-J.; Shimotani, H.; Suzuki, R.; Toh, M.; Kloc, C.; Xu, X.; Arita, R.; Nagaosa, N.; Iwasa, Y. *Nat Phys* **2013,** 9, (9), 563-569.

19. Xiao, D.; Liu, G. B.; Feng, W.; Xu, X.; Yao, W. *Phys Rev Lett* **2012,** 108, (19), 196802.
20. Bychkov, Y. A.; Rashba, E. I. *JETP letters* **1984,** 39, (78), 66-69.
21. Kim, C.; Park, S. R. *Physics and High Technology* **2014,** 23, (10), 25.
22. Jakobs, S.; Ruffing, A.; Cinchetti, M.; Mathias, S.; Aeschlimann, M. *Phys Rev B* **2013,** 87, (23).
23. Tamai, A.; Meevasana, W.; King, P. D. C.; Nicholson, C. W.; de la Torre, A.; Rozbicki, E.; Baumberger, F. *Phys Rev B* **2013,** 87, (7).
24. King, P. D.; McKeown Walker, S.; Tamai, A.; de la Torre, A.; Eknapakul, T.; Buaphet, P.; Mo, S. K.; Meevasana, W.; Bahramy, M. S.; Baumberger, F. *Nat Commun* **2014,** 5, 3414.
25. Park, S. R.; Han, J.; Kim, C.; Koh, Y. Y.; Kim, C.; Lee, H.; Choi, H. J.; Han, J. H.; Lee, K. D.; Hur, N. J.; Arita, M.; Shimada, K.; Namatame, H.; Taniguchi, M. *Phys Rev Lett* **2012,** 108, (4), 046805.
26. Nitta, J.; Akazaki, T.; Takayanagi, H.; Enoki, R. *Phys Rev Lett* **1997,** 78, (7), 1335.
27. Rowe, A. C. H.; Nehls, J.; Stradling, R. A.; Ferguson, R. S. *Phys Rev B* **2001,** 63, (20).
28. Datta, S.; Das, B. *Appl Phys Lett* **1990,** 56, (7), 665-667.
29. Koo, H. C.; Kwon, J. H.; Eom, J.; Chang, J.; Han, S. H.; Johnson, M. *Science* **2009,** 325, (5947), 1515.
30. Edelstein, V. M. *Solid State Communications* **1990,** 73, (3), 233-235.
31. Sánchez, J. C. R.; Vila, L.; Desfonds, G.; Gambarelli, S.; Attané, J. P.; De Teresa, J. M.; Magén, C.; Fert, A. *Nat Commun* **2013,** 4, 2944.
32. Ganichev, S. D.; Ivchenko, E. L.; Bel'kov, V. V.; Tarasenko, S. A.; Sollinger, M.; Weiss, D.; Wegscheider, W.; Prettl, W. *Nature* **2002,** 417, (6885), 153-156.
33. Ganichev, S. D. *Physica E: Low-dimensional Systems and Nanostructures* **2004,** 20, (3-4), 419-423.
34. Grachev, A. I. *Physics of the Solid State* **2004,** 46, (11), 2008-2011.
35. Golub, L. E. *JETP Letters* **2007,** 85, (8), 393-397.
36. Garate, I.; Franz, M. *Phys Rev Lett* **2010,** 104, (14), 146802.
37. Skinner, T. D.; Olejnik, K.; Cunningham, L. K.; Kurebayashi, H.; Campion, R. P.; Gallagher, B. L.; Jungwirth, T.; Ferguson, A. J. *Nat Commun* **2015,** 6, 6730.
38. Chen, L.; Decker, M.; Kronseder, M.; Islinger, R.; Gmitra, M.; Schuh, D.; Bougeard, D.; Fabian, J.; Weiss, D.; Back, C. H. *Nat Commun* **2016,** 7, 13802.
39. Dyakonov, M. I.; Perel, V. I. *JETP letters* **1971,** 13, 467.
40. Dyakonov, M. I.; Perel, V. I. *Physics Letters A* **1971,** 35, (6), 459-460.
41. Nagaosa, N.; Sinova, J.; Onoda, S.; MacDonald, A. H.; Ong, N. P. *Reviews of Modern Physics* **2010,** 82, (2), 1539-1592.
42. Kato, Y. K.; Myers, R. C.; Gossard, A. C.; Awschalom, D. D. *Science* **2004,** 306, (5703), 1910.

43. Wunderlich, J.; Kaestner, B.; Sinova, J.; Jungwirth, T. *Phys Rev Lett* **2005,** 94, (4), 047204.
44. Saitoh, E.; Ueda, M.; Miyajima, H.; Tatara, G. *Appl Phys Lett* **2006,** 88, (18), 182509.
45. Harii, K.; Ando, K.; Sasage, K.; Saitoh, E. *physica status solidi (c)* **2007,** 4, (12), 4437-4440.
46. Mosendz, O.; Pearson, J. E.; Fradin, F. Y.; Bauer, G. E.; Bader, S. D.; Hoffmann, A. *Phys Rev Lett* **2010,** 104, (4), 046601.
47. Yoshino, T.; Kajiwara, Y.; Ando, K.; Nakayama, H.; Ota, T.; Uchida, K.; Saitoh, E. *Journal of Physics: Conference Series* **2010,** 200, (6), 062038.
48. Ando, K.; Kajiwara, Y.; Takahashi, S.; Maekawa, S.; Takemoto, K.; Takatsu, M.; Saitoh, E. *Phys Rev B* **2008,** 78, (1).
49. Ando, K.; Takahashi, S.; Harii, K.; Sasage, K.; Ieda, J.; Maekawa, S.; Saitoh, E. *Phys Rev Lett* **2008,** 101, (3), 036601.
50. Ando, K.; Ieda, J.; Sasage, K.; Takahashi, S.; Maekawa, S.; Saitoh, E. *Appl Phys Lett* **2009,** 94, (26), 262505.
51. Ando, K.; Takahashi, S.; Ieda, J.; Kurebayashi, H.; Trypiniotis, T.; Barnes, C. H.; Maekawa, S.; Saitoh, E. *Nat Mater* **2011,** 10, (9), 655-9.
52. Valenzuela, S. O.; Tinkham, M. *Nature* **2006,** 442, (7099), 176-179.
53. Seki, T.; Hasegawa, Y.; Mitani, S.; Takahashi, S.; Imamura, H.; Maekawa, S.; Nitta, J.; Takanashi, K. *Nat Mater* **2008,** 7, (2), 125-9.
54. Abanin, D. A.; Shytov, A. V.; Levitov, L. S.; Halperin, B. I. *Phys Rev B* **2009,** 79, (3).
55. Mihajlovic, G.; Pearson, J. E.; Garcia, M. A.; Bader, S. D.; Hoffmann, A. *Phys Rev Lett* **2009,** 103, (16), 166601.
56. Brüne, C.; Roth, A.; Novik, E. G.; König, M.; Buhmann, H.; Hankiewicz, E. M.; Hanke, W.; Sinova, J.; Molenkamp, L. W. *Nat Phys* **2010,** 6, (6), 448-454.
57. Wunderlich, J.; Park, B.-G.; Irvine, A. C.; Zârbo, L. P.; Rozkotová, E.; Nemec, P.; Novák, V.; Sinova, J.; Jungwirth, T. *Science* **2010,** 330, (6012), 1801.
58. Balakrishnan, J.; Kok Wai Koon, G.; Jaiswal, M.; Castro Neto, A. H.; Özyilmaz, B. *Nat Phys* **2013,** 9, (5), 284-287.
59. Balakrishnan, J.; Koon, G. K.; Avsar, A.; Ho, Y.; Lee, J. H.; Jaiswal, M.; Baeck, S. J.; Ahn, J. H.; Ferreira, A.; Cazalilla, M. A.; Castro Neto, A. H.; Ozyilmaz, B. *Nat Commun* **2014,** 5, 4748.
60. Caviglia, A. Two-dimensional electron gas in functional oxide interfaces. . University of Deneve, 2010.
61. Kobayashi, S.; Mizumukai, Y.; Ohnishi, T.; Shibata, N.; Ikuhara, Y.; Yamamoto, T. *Acs Nano* **2015,** 9, (11), 10769-10777.
62. Son, J.; Moetakef, P.; Jalan, B.; Bierwagen, O.; Wright, N. J.; Engel-Herbert, R.; Stemmer, S. *Nat Mater* **2010,** 9, (6), 482-484.

63. Han, W.; Jiang, X.; Kajdos, A.; Yang, S. H.; Stemmer, S.; Parkin, S. S. *Nat Commun* **2013,** 4, 2134.
64. Gallagher, P.; Lee, M.; Williams, J. R.; Goldhaber-Gordon, D. *Nat Phys* **2014**.
65. Wang, N.; Chen, H.; He, H.; Norimatsu, W.; Kusunoki, M.; Koumoto, K. *Sci Rep* **2013,** 3, 3449.
66. Lee, S. W.; Liu, Y.; Heo, J.; Gordon, R. G. *Nano Letters* **2012,** 12, (9), 4775-4783.
67. Chen, Y. Z.; Bovet, N.; Trier, F.; Christensen, D. V.; Qu, F. M.; Andersen, N. H.; Kasama, T.; Zhang, W.; Giraud, R.; Dufouleur, J.; Jespersen, T. S.; Sun, J. R.; Smith, A.; Nygard, J.; Lu, L.; Buchner, B.; Shen, B. G.; Linderoth, S.; Pryds, N. *Nat Commun* **2013,** 4, 1371.
68. Ohtomo, A.; Hwang, H. Y. *Nature* **2004,** 427, (6973), 423-426.
69. Peter, E. Top-gating of the two-dimensional electron gas at complex oxide interfaces. University of Twente, 2014.
70. Nakagawa, N.; Hwang, H. Y.; Muller, D. A. *Nat Mater* **2006,** 5, (3), 204-209.
71. Li, L.; Richter, C.; Mannhart, J.; Ashoori, R. C. *Nat Phys* **2011,** 7, (10), 762-766.
72. Dikin, D. A.; Mehta, M.; Bark, C. W.; Folkman, C. M.; Eom, C. B.; Chandrasekhar, V. *Phys Rev Lett* **2011,** 107, (5), 056802.
73. Bert, J. A.; Kalisky, B.; Bell, C.; Kim, M.; Hikita, Y.; Hwang, H. Y.; Moler, K. A. *Nat Phys* **2011,** 7, (10), 767-771.
74. Delugas, P.; Filippetti, A.; Fiorentini, V.; Bilc, D. I.; Fontaine, D.; Ghosez, P. *Phys Rev Lett* **2011,** 106, (16), 166807.
75. Son, W.-j.; Cho, E.; Lee, B.; Lee, J.; Han, S. *Phys Rev B* **2009,** 79, (24).
76. Lee, J. S.; Xie, Y. W.; Sato, H. K.; Bell, C.; Hikita, Y.; Hwang, H. Y.; Kao, C. C. *Nat Mater* **2013,** 12, (8), 703-706.
77. Joshua, A.; Ruhman, J.; Pecker, S.; Altman, E.; Ilani, S. *P Natl Acad Sci USA* **2013,** 110, (24), 9633-9638.
78. Gabay, M.; Triscone, J.-M. *Nat Phys* **2013,** 9, (10), 610-611.
79. Herranz, G.; Basletic, M.; Bibes, M.; Carretero, C.; Tafra, E.; Jacquet, E.; Bouzehouane, K.; Deranlot, C.; Hamzic, A.; Broto, J. M.; Barthelemy, A.; Fert, A. *Phys Rev Lett* **2007,** 98, (21), 216803.
80. Brinkman, A.; Huijben, M.; Van Zalk, M.; Huijben, J.; Zeitler, U.; Maan, J. C.; Van der Wiel, W. G.; Rijnders, G.; Blank, D. H. A.; Hilgenkamp, H. *Nat Mater* **2007,** 6, (7), 493-496.
81. Reyren, N.; Bibes, M.; Lesne, E.; George, J. M.; Deranlot, C.; Collin, S.; Barthelemy, A.; Jaffres, H. *Phys Rev Lett* **2012,** 108, (18), 186802.
82. Swartz, A. G.; Harashima, S.; Xie, Y.; Lu, D.; Kim, B.; Bell, C.; Hikita, Y.; Hwang, H. Y. *Appl Phys Lett* **2014,** 105, (3), 032406.
83. Caviglia, A. D.; Gabay, M.; Gariglio, S.; Reyren, N.; Cancellieri, C.; Triscone, J. M. *Phys Rev*

Lett **2010,** 104, (12), 126803.

84. Banerjee, S.; Erten, O.; Randeria, M. *Nat Phys* **2013,** 9, (10), 625-629.
85. Zubko, P.; Gariglio, S.; Gabay, M.; Ghosez, P.; Triscone, J.-M. *Annual Review of Condensed Matter Physics* **2011,** 2, (1), 141-165.
86. Reyren, N.; Thiel, S.; Caviglia, A. D.; Kourkoutis, L. F.; Hammerl, G.; Richter, C.; Schneider, C. W.; Kopp, T.; Rüetschi, A. S.; Jaccard, D.; Gabay, M.; Muller, D. A.; Triscone, J. M.; Mannhart, J. *Science* **2007,** 317, (5842), 1196.
87. Ariando; Wang, X.; Baskaran, G.; Liu, Z. Q.; Huijben, J.; Yi, J. B.; Annadi, A.; Barman, A. R.; Rusydi, A.; Dhar, S.; Feng, Y. P.; Ding, J.; Hilgenkamp, H.; Venkatesan, T. *Nat Commun* **2011,** 2, 188.
88. Basletic, M.; Maurice, J. L.; Carretero, C.; Herranz, G.; Copie, O.; Bibes, M.; Jacquet, E.; Bouzehouane, K.; Fusil, S.; Barthelemy, A. *Nat Mater* **2008,** 7, (8), 621-625.
89. Thiel, S.; Hammerl, G.; Schmehl, A.; Schneider, C. W.; Mannhart, J. *Science* **2006,** 313, (5795), 1942.
90. Cen, C.; Thiel, S.; Hammerl, G.; Schneider, C. W.; Andersen, K. E.; Hellberg, C. S.; Mannhart, J.; Levy, J. *Nat Mater* **2008,** 7, (4), 298-302.
91. Yoshimatsu, K.; Yasuhara, R.; Kumigashira, H.; Oshima, M. *Phys Rev Lett* **2008,** 101, (2), 026802.
92. Chambers, S. A. *Surface Science* **2011,** 605, (13-14), 1133-1140.
93. Caviglia, A. D.; Gariglio, S.; Reyren, N.; Jaccard, D.; Schneider, T.; Gabay, M.; Thiel, S.; Hammerl, G.; Mannhart, J.; Triscone, J. M. *Nature* **2008,** 456, (7222), 624-627.
94. Ben Shalom, M.; Ron, A.; Palevski, A.; Dagan, Y. *Phys Rev Lett* **2010,** 105, (20), 206401.
95. Fête, A.; Gariglio, S.; Berthod, C.; Li, D.; Stornaiuolo, D.; Gabay, M.; Triscone, J. M. *New Journal of Physics* **2014,** 16, (11), 112002.
96. Narayanapillai, K.; Gopinadhan, K.; Qiu, X.; Annadi, A.; Ariando; Venkatesan, T.; Yang, H. *Appl Phys Lett* **2014,** 105, (16), 162405.
97. Herranz, G.; Sanchez, F.; Dix, N.; Scigaj, M.; Fontcuberta, J. *Sci Rep* **2012,** 2, 758.
98. Mathew, S.; Annadi, A.; Chan, T. K.; Asmara, T. C.; Zhan, D.; Wang, X. R.; Azimi, S.; Shen, Z.; Rusydi, A.; Ariando; Breese, M. B. H.; Venkatesan, T. *Acs Nano* **2013,** 7, (12), 10572-10581.
99. Dai, W.; Adhikari, S.; Garcia-Castro, A. C.; Romero, A. H.; Lee, H.; Lee, J. W.; Ryu, S.; Eom, C. B.; Cen, C. *Nano Lett* **2016,** 16, (4), 2739-43.
100. Chen, Y. Z.; Trier, F.; Wijnands, T.; Green, R. J.; Gauquelin, N.; Egoavil, R.; Christensen, D. V.; Koster, G.; Huijben, M.; Bovet, N.; Macke, S.; He, F.; Sutarto, R.; Andersen, N. H.; Sulpizio, J. A.; Honig, M.; Prawiroatmodjo, G. E. D. K.; Jespersen, T. S.; Linderoth, S.; Ilani, S.; Verbeeck, J.; Van Tendeloo, G.; Rijnders, G.; Sawatzky, G. A.; Pryds, N. *Nat Mater* **2015,** 14, (8), 801-806.

101. Huijben, M.; Koster, G.; Kruize, M. K.; Wenderich, S.; Verbeeck, J.; Bals, S.; Slooten, E.; Shi, B.; Molegraaf, H. J. A.; Kleibeuker, J. E.; van Aert, S.; Goedkoop, J. B.; Brinkman, A.; Blank, D. H. A.; Golden, M. S.; van Tendeloo, G.; Hilgenkamp, H.; Rijnders, G. *Advanced Functional Materials* **2013,** 23, (42), 5240-5248.

102. Reinle-Schmitt, M. L.; Cancellieri, C.; Li, D.; Fontaine, D.; Medarde, M.; Pomjakushina, E.; Schneider, C. W.; Gariglio, S.; Ghosez, P.; Triscone, J. M.; Willmott, P. R. *Nat Commun* **2012,** 3, 932.

103. Tra, V. T.; Yang, J.-C.; Hsieh, Y.-H.; Lin, J.-Y.; Chen, Y.-C.; Chu, Y.-H. *physica status solidi (RRL) - Rapid Research Letters* **2014,** 8, (6), 478-500.

104. Hosoda, M.; Hikita, Y.; Hwang, H. Y.; Bell, C. *Appl Phys Lett* **2013,** 103, (10), 103507.

105. Liang, H.; Cheng, L.; Zhai, X.; Pan, N.; Guo, H.; Zhao, J.; Zhang, H.; Li, L.; Zhang, X.; Wang, X.; Zeng, C.; Zhang, Z.; Hou, J. G. *Scientific Reports* **2013,** 3, 1975.

106. Chan, N. Y.; Zhao, M.; Huang, J.; Au, K.; Wong, M. H.; Yao, H. M.; Lu, W.; Chen, Y.; Ong, C. W.; Chan, H. L.; Dai, J. *Adv Mater* **2014,** 26, (34), 5962-8.

107. Pallecchi, I.; Telesio, F.; Li, D.; Fete, A.; Gariglio, S.; Triscone, J. M.; Filippetti, A.; Delugas, P.; Fiorentini, V.; Marre, D. *Nat Commun* **2015,** 6, 6678.

108. Sulpizio, J. A.; Ilani, S.; Irvin, P.; Levy, J. *Annual Review of Materials Research* **2014,** 44, (1), 117-149.

109. Min, B. C.; Motohashi, K.; Lodder, C.; Jansen, R. *Nat Mater* **2006,** 5, (10), 817-22.

110. Lesne, E.; Fu, Y.; Oyarzun, S.; Rojas-Sanchez, J. C.; Vaz, D. C.; Naganuma, H.; Sicoli, G.; Attane, J. P.; Jamet, M.; Jacquet, E.; George, J. M.; Barthelemy, A.; Jaffres, H.; Fert, A.; Bibes, M.; Vila, L. *Nat Mater* **2016,** 15, (12), 1261-1266.

111. Hook, J. R.; Hall, H. E., *Solid State Physics*. John Willey & Sons: 2010.

112. Dirac, P. A. M., *The principles of quantum mechanics*. Oxford University Press: 1958.

113. Datta, S., *Electronic transport in Mesoscopic system*. Cambrige: 1995.

114. Fete, A.; Gariglio, S.; Caviglia, A. D.; Triscone, J. M.; Gabay, M. *Phys Rev B* **2012,** 86, (20), 201105(R).

115. Stornaiuolo, D.; Gariglio, S.; Fête, A.; Gabay, M.; Li, D.; Massarotti, D.; Triscone, J. M. *Phys Rev B* **2014,** 90, (23).

116. Goble, N. J.; Akrobetu, R.; Zaid, H.; Sucharitakul, S.; Berger, M. H.; Sehirlioglu, A.; Gao, X. P. *Sci Rep* **2017,** 7, 44361.

117. Santander-Syro, A. F.; Copie, O.; Kondo, T.; Fortuna, F.; Pailhes, S.; Weht, R.; Qiu, X. G.; Bertran, F.; Nicolaou, A.; Taleb-Ibrahimi, A.; Le Fevre, P.; Herranz, G.; Bibes, M.; Reyren, N.; Apertet, Y.; Lecoeur, P.; Barthelemy, A.; Rozenberg, M. J. *Nature* **2011,** 469, (7329), 189-93.

118. Rakhmilevitch, D.; Ben Shalom, M.; Eshkol, M.; Tsukernik, A.; Palevski, A.; Dagan, Y. *Phys*

Rev B **2010,** 82, (23).

119. Chang, J. W.; Song, J.; Lee, J. S.; Noh, H.; Seung, S. K.; Baasandorj, L.; Lee, S. G.; Doh, Y. J.; Kim, J. *Appl Phys Express* **2013,** 6, (8), 085201.
120. Hwang, H. Y.; Iwasa, Y.; Kawasaki, M.; Keimer, B.; Nagaosa, N.; Tokura, Y. *Nat Mater* **2012,** 11, (2), 103-113.
121. Bark, C. W.; Sharma, P.; Wang, Y.; Baek, S. H.; Lee, S.; Ryu, S.; Folkman, C. M.; Paudel, T. R.; Kumar, A.; Kalinin, S. V.; Sokolov, A.; Tsymbal, E. Y.; Rzchowski, M. S.; Gruverman, A.; Eom, C. B. *Nano Letters* **2012,** 12, (4), 1765-1771.
122. Kim, S. I.; Kim, D. H.; Kim, Y.; Moon, S. Y.; Kang, M. G.; Choi, J. K.; Jang, H. W.; Kim, S. K.; Choi, J. W.; Yoon, S. J.; Chang, H. J.; Kang, C. Y.; Lee, S.; Hong, S. H.; Kim, J. S.; Baek, S. H. *Adv Mater* **2013,** 25, (33), 4612-4617.
123. Ben Shalom, M.; Sachs, M.; Rakhmilevitch, D.; Palevski, A.; Dagan, Y. *Phys Rev Lett* **2010,** 104, (12).
124. Bi, F.; Huang, M. C.; Ryu, S.; Lee, H.; Bark, C. W.; Eom, C. B.; Irvin, P.; Levy, J. *Nat Commun* **2014,** 5, 5019.
125. Ngo, T. D. N.; Chang, J. W.; Lee, K.; Han, S.; Lee, J. S.; Kim, Y. H.; Jung, M. H.; Doh, Y. J.; Choi, M. S.; Song, J.; Kim, J. *Nat Commun* **2015,** 6, 8035.
126. Sahin, C.; Vignale, G.; Flatte, M. E. *Phys Rev B* **2014,** 89, (15), 155402.
127. Zhong, Z. C.; Toth, A.; Held, K. *Phys Rev B* **2013,** 87, (16), 161102(R).
128. Liang, H. X.; Cheng, L.; Wei, L. M.; Luo, Z. L.; Yu, G. L.; Zeng, C. G.; Zhang, Z. Y. *Phys Rev B* **2015,** 92, (7), 075309.
129. Gopinadhan, K.; Annadi, A.; Kim, Y.; Srivastava, A.; Kumar, B.; Chen, J. S.; Coey, J. M. D.; Ariando; Venkatesan, T. *Adv Electron Mater* **2015,** 1, (8), 1500114.
130. Choi, W. Y.; Kim, H. J.; Chang, J.; Han, S. H.; Koo, H. C.; Johnson, M. *Nat Nanotechnol* **2015,** 10, (8), 666-670.
131. Hayden, L. X.; Raimondi, R.; Flatte, M. E.; Vignale, G. *Phys Rev B* **2013,** 88, (7), 075405.
132. Bibes, M.; Reyren, N.; Lesne, E.; George, J. M.; Deranlot, C.; Collin, S.; Barthelemy, A.; Jaffres, H. *Philos T R Soc A* **2012,** 370, (1977), 4958-4971.
133. Bibes, M.; Villegas, J. E.; Barthelemy, A. *Adv Phys* **2011,** 60, (1), 5-84.
134. Inoue, H.; Swartz, A. G.; Harmon, N. J.; Tachikawa, T.; Hikita, Y.; Flatte, M. E.; Hwang, H. Y. *Phys Rev X* **2015,** 5, (4), 041023.
135. Goswami, S.; Mulazimoglu, E.; Vandersypen, L. M. K.; Caviglia, A. D. *Nano Letters* **2015,** 15, (4), 2627-2632.
136. Ohtomo, A.; Hwang, H. Y. *Nature* **2004,** 427, (6973), 423-6.
137. Mattheis.Lf. *Phys Rev B* **1972,** 6, (12), 4740-4753.

138. Noto, K.; Tsuzuku, T. *Carbon* **1974,** 12, (2), 209-210.

139. Hernandez, T.; Bark, C. W.; Felker, D. A.; Eom, C. B.; Rzchowski, M. S. *Phys Rev B* **2012,** 85, (16), 161407(R).

140. Narayanapillai, K.; Gopinadhan, K.; Qiu, X. P.; Annadi, A.; Ariando; Venkatesan, T.; Yang, H. *Appl Phys Lett* **2014,** 105, (16), 162405.

141. Miron, I. M.; Garello, K.; Gaudin, G.; Zermatten, P. J.; Costache, M. V.; Auffret, S.; Bandiera, S.; Rodmacq, B.; Schuhl, A.; Gambardella, P. *Nature* **2011,** 476, (7359), 189-U88.

142. Liu, L. Q.; Pai, C. F.; Li, Y.; Tseng, H. W.; Ralph, D. C.; Buhrman, R. A. *Science* **2012,** 336, (6081), 555-558.

143. Kim, J.; Sinha, J.; Hayashi, M.; Yamanouchi, M.; Fukami, S.; Suzuki, T.; Mitani, S.; Ohno, H. *Nat Mater* **2013,** 12, (3), 240-245.

144. Annadi, A.; Huang, Z.; Gopinadhan, K.; Wang, X. R.; Srivastava, A.; Liu, Z. Q.; Ma, H. H.; Sarkar, T. P.; Venkatesan, T.; Ariando. *Phys Rev B* **2013,** 87, (20).

145. Abanin, D. A.; Shytov, A. V.; Levitov, L. S.; Halperin, B. I. *Phys Rev B* **2009,** 79, (3), 035304.

146. Dyakonov, M. I.; Perel, V. I. *Fiz Tverd Tela+* **1972,** 13, (12), 3023-3026.

147. Elliott, R. J. *Phys Rev* **1954,** 96, (2), 266-279.

148. Yafet, Y. *Solid State Phys* **1963,** 14, 1-98.

149. Zomer, P. J.; Guimaraes, M. H. D.; Tombros, N.; van Wees, B. J. *Phys Rev B* **2012,** 86, (16), 161416(R).

150. Chen, Y. Z.; Trier, F.; Kasama, T.; Christensen, D. V.; Bovet, N.; Balogh, Z. I.; Li, H.; Thyden, K. T. S.; Zhang, W.; Yazdi, S.; Norby, P.; Pryds, N.; Linderoth, S. *Nano Letters* **2015,** 15, (3), 1849-1854.

151. Liu, L. Q.; Moriyama, T.; Ralph, D. C.; Buhrman, R. A. *Phys Rev Lett* **2011,** 106, (3), 036601.

152. Morota, M.; Niimi, Y.; Ohnishi, K.; Wei, D. H.; Tanaka, T.; Kontani, H.; Kimura, T.; Otani, Y. *Phys Rev B* **2011,** 83, (17).

** Chapter 5 is reproduced in part with permission of "Nonlocal Spin Diffusion Driven by Giant Spin Hall Effect at Oxide Heterointerface, Nano Letters, 17, 36-43, 2017".*
Copyright 2016 American Chemical Society.

Appendix A : List of Achievements

The results of this dissertation & during Ph. D course I have been published in :

1. **Mi-jin Jin**, Junhyeon Jo, Guru P. Neupane, Jeongyong Kim, Ki-Seok An and Jung-Woo Yoo, "Tuning of undoped ZnO thin film via plasma enhanced atomic layer deposition and its application for an inverted polymer solar cell", *AIP advances*, **3**, 102114 (2013)
2. Junhyeon Jo, **Mi-Jin Jin**, Jungmin Park, Vijayakumar Modepalli, Chi-Yueh Kao,A.J. Epstein, Min Choi, Noejung Park, Seung-Yeop Lee, Cheolho Jeon and Jung-Woo Yoo, "Organic-based magnetic semiconductor thin film of Fe(TCNQ)x～2developed by physical vapor deposition and local spin densityinduced core-level shifts", *Synthetic Metals*, **196**, 56–60, (2014)
3. **Mi-Jin Jin**, Junhyeon Jo, Ji-Hee Kim, Ki-Seok An, Mun Seok Jeong, Jeongyong Kim and Jung-Woo Yoo, "Effects of TiO2 Interfacial Atomic Layers on Device Performances and Exciton Dynamics in ZnO Nanorod Polymer Solar Cells", *ACS Appl. Mater. Interfaces*, **6**, 11649−11656, (2014)
4. **Mi-Jin Jin**, Junhyeon Jo and Jung-Woo Yoo, "Impedance spectroscopy analysis on the effects of TiO_2 interfacial atomic layers in ZnO nanorod polymer solar cells:Effects of interfacial charge extraction on diffusion and recombination", *Organic Electronics,* **19**, 83–91, (2015)
5. Vijayakumar Modepalli, **Mi-Jin Jin**, Jungmin Park, Junhyeon Jo, Ji-Hyun Kim, Jeong Min Baik, Changwon Seo, Jeongyong Kim, and Jung-Woo Yoo, "Gate-Tunable Spin Exchange Interactions and Inversion of magneto-resistance in Single Ferromagnetic ZnO Nanowires", *ACS Nano*, **10**, 4618−4626, (2016)
6. Jeong-Hyeon Lee, Shumin He, Peter Grunberg, **Mi-Jin Jin**, Jung-Woo Yoo and B. K. Cho, "A comparative study of three-terminal Hanle signals in CoFe/SiO2/n1-Si and Cu/SiO2/n1-Si tunnel junctions", *Applied Physics Letters*, **108**, 032406 (2016)
7. Hyo-Ki Hong, Junhyeon Jo, Daeyeon Hwang, Jongyeong Lee, Na Yeon Kim, Seungwoo Son, Jung Hwa Kim, **Mi-Jin Jin**, Young Chul Jun, Rolf Erni, Sang Kyu Kwak, Jung-Woo Yoo and Zonghoon Lee, "Atomic Scale Study on Growth and Heteroepitaxy of ZnO Monolayer on Graphene", *Nano Letters* **17**, 120−127, (2017)
8. **Mi-Jin Jin**, Seon Young Moon, Jungmin Park, Vijayakumar Modepalli, Junhyeon Jo, Shin-Ik Kim, Hyun Cheol Koo, Byoung-Chul Min, Hyun-Woo Lee, Seung-Hyub Baek and Jung-Woo Yoo, "Nonlocal Spin Diffusion Driven by Giant Spin Hall Effect at Oxide Heterointerfaces", *Nano Letters*, **17**, 36−43, (2017)
9. Jungmin Park, Hyung Duk Yun, **Mi-Jin Jin**, Junhyun Jo, Inseon Oh, Vijayakumar Modepalli,

Soon-Yong Kwon and Jung-Woo Yoo, "Gate-dependent spin Hall induced nonlocal resistance and the symmetry of spin-orbit scattering in Au-clustered graphene", *Physical Review B* (2017), *accepted*

Conference Presentaions & Honors and Awards :

1. 우수 발표상(포스터 부문), **Mi-jin Jin**, JunHyun Jo, Vijayakumar Modepalli, Jungmin Park and Jung-Woo Yoo, "Thermally induced charge tunneling into graphene", 한국물리학회, 한물 2013-411호
2. 최우수 발표상(포스터 부문), **Mi-jin Jin**, seon Young Moon, JunHyun Jo, Vijayakumar Modepalli, Jungmin Park, Seung-Hyub Baek, and Jung-Woo Yoo, "Spin –orbit coupling induced non-local signal in quasi-2DEG of LAO/STO", 한국물리학회, 한물 2014-540호
3. 우수 발표상(구두 부문), **Mi-jin Jin**, Seon Young Moon, Vijayakumar Modepalli, Jungmin Park, JunHyun Jo, Seung-Hyub Baek, and Jung-Woo Yoo, "Non-local spin signal in quasi-2DEG of LAO/STO", 한국물리학회, 한물 2016-325호

Acknowledgements

During my Ph. D course, most hard thing was to study new field of spintronics. It was quite different from my last research field until master course and researcher in other research center. My major was based on material engineering (especially in electronic materials and devices), and because of that, I was extremely slowly learn about spin engineering during my Ph. D course. I slowly understand about spintronics with step by step and I was getting more interested in the field. So now, I recognized that I have enlarged my research spectrum because of this Ph. D course. I am so glad to meet this research field and I would like to study more deeply and widely in the future.

In this page, I would like to express my appreciations during my Ph. D course.

Most of all, I am specially thanks and gratitude to my thesis adviser Prof. Jung-Woo Yoo, *Ulsan National Institute of Science and Technology (UNIST)* for his guidance, assistance, and patience during my Ph.D course. It is a great honor to work under his supervision. My thesis works would not have been possible without his help.

And I would like to thank my committee members, Prof. Seung Hyub Baek, *Korea Institute of Science and Technology (KIST)*, Prof. Ki-Bok Park, Hyung-Jun Shin, and Ki-Suk Lee, *Ulsan National Institute of Science and Technology (UNIST)*, for their suggestion and encouragement. I also would like to express my appreciations to my co-workers, Seon Young Moon, Shin-Ik Kim from KIST for the patient supporting of my experiment samples.

I feel appreciate and sorry to my laboratory members Vijayakumar Modepalli, Jungmin park, Junhyeon Jo that they have hard time to set up all the laboratory equipment and experiment system with me. And I happy to meet coming new members of Inseon Oh, Daesung Choi. I feel so appreciate to all my laboratory members for their devotion and help me at the end of my Ph. D course (especially, this year I was pregnant and I cannot do many things for/at laboratory.). And I would like to thank my UNIST friends Minbok Jung, Byung-Uk Ye, Jinsung Chun, Ji-hyun Kim, Ja-young Won, Su-in Kim, Namkyu Kim, Su-Suk Lee, Hee-Sung Han, Dae-Han Jung, Su-Min Seo, Chan-Wool Kim, Min-Joo Park, etc. They was a tonic in my UNIST life.

Lastly, I would like to tell my family (my parents, brother and his wife, and my nephew) that I love them so much. And I would like to express my special thanks to my lovely husband for his trust and encouragement during my Ph. D course as a colleague, lover, friend and husband. If he were not beside me, I cannot stand this course. And I feel thanks to god for giving us lovely baby.